



HAL
open science

Deformation mechanisms of nanostructured thermoelectric alloys

Matthieu Aumand

► **To cite this version:**

Matthieu Aumand. Deformation mechanisms of nanostructured thermoelectric alloys. Materials. Université de Poitiers; University of Houston, 2018. English. NNT : 2018POIT2281 . tel-02055986

HAL Id: tel-02055986

<https://theses.hal.science/tel-02055986>

Submitted on 4 Mar 2019

HAL is a multi-disciplinary open access archive for the deposit and dissemination of scientific research documents, whether they are published or not. The documents may come from teaching and research institutions in France or abroad, or from public or private research centers.

L'archive ouverte pluridisciplinaire **HAL**, est destinée au dépôt et à la diffusion de documents scientifiques de niveau recherche, publiés ou non, émanant des établissements d'enseignement et de recherche français ou étrangers, des laboratoires publics ou privés.



THÈSE

pour l'obtention du Grade de

DOCTEUR DE L'UNIVERSITÉ DE POITIERS
(Faculté des Sciences Fondamentales et Appliquées)
(Diplôme National - Arrêté du 7 août 2006)

Ecole Doctorale : Sciences et Ingénierie
en Matériaux, Mécanique, Énergétique et Aéronautique

Secteur de Recherche : Milieux denses, Matériaux et Composants

Présentée par:

Matthieu AUMAND

DEFORMATION MECHANISMS OF NANOSTRUCTURED THERMOELECTRIC ALLOYS

Directeurs de Thèse : **L. THILLY et K. WHITE**

Soutenue le 12 Septembre 2018 devant la commission d'examen

JURY

Pradeep SHARMA	Professor, University of Houston	Chair
Michael DEMKOWICZ	Associate Professor, Texas A&M University	Rapporteur
Robert VAJTAI	Research Professor, Rice University	Rapporteur
Yashashree KULKARNI	Associate Professor, University of Houston	Examinatrice
Andrew ROBERTSON	Research Scientist, Baker Hughes	Examineur
Christophe TROMAS	Professeur, Université de Poitiers	Examineur
Ken WHITE	Professor, University of Houston	Examineur
Ludovic THILLY	Professeur, Université de Poitiers	Examineur

DEFORMATION MECHANISMS OF NANOSTRUCTURED
THERMOELECTRIC ALLOYS

A Dissertation

Presented to

The Faculty of the Department
of Materials Science and Engineering
University of Houston

In Partial Fulfillment

of the Requirements for the Degree of

Doctor of Philosophy

in Materials Science and Engineering

By

Matthieu Aumand

December 2018

Acknowledgements

I would like to thank Ludovic Thilly, who allowed me to step into this unique opportunity that is a cotutelle PhD program. Our constructive discussions, and his guidance during these years made this project a unique piece of work, supporting the effort of the thermoelectric materials community, and trained me toward higher standards both as a student and a scientist, with a special thanks for hosting me at the Pprime institute. I would like to thank Ken White for welcoming me into his research group at the University of Houston, and for his guidance into the U.S. academic system and during these years of work. I would like to thank Anne-Marie at the Pprime Institute, with whom the many days of polishing were made easier while listening to Jazz music, and from whom my work benefited thanks to her many technical advices. Extended appreciation is given to the workshop personnel at Pprime, who made many experiments possible by giving me access to their facilities on many occasions. Many thanks to Jerry Clifton at the University of Houston, who provided many technical counsel and support, allowing us to build flawless experimental setups in no time. Special thanks to Jean-Baptiste Giouse, with whom I shared an office all these years both at UH and Pprime, as well as many successes both in school and in the lab.

My deepest gratitude goes to my wife, Gaëlle Auguste, for her continual support, and for her strength while I spent these many months abroad. Many thanks to all my family for their support in this endeavor.

À mon ami Pierre.

DEFORMATION MECHANISMS OF NANOSTRUCTURED
THERMOELECTRIC ALLOYS

An abstract
of a dissertation presented to
the Faculty of the Department
of Materials Science and Engineering
University of Houston

In Partial Fulfillment
of the Requirements for the Degree of
Doctor of Philosophy
in Materials Science and Engineering

By
Matthieu Aumand
December 2018

Abstract

Increasing the figure of merit ZT of thermoelectric (TE) alloys is a challenge that is currently attempted through various metallurgy methods, including nanostructuring and dislocation engineering. Microstructures with such level of complexity raises questions about the mechanical reliability of these new materials. Indeed, despite the values of hardness and elastic modulus known for the clear majority of TE materials, the data on deformation mechanisms are still rare. Focusing on the nanostructured p-type half-Heusler $\text{Hf}_{0.44}\text{Zr}_{0.44}\text{Ti}_{0.12}\text{CoSb}_{0.8}\text{Sn}_{0.2}$, our multi-scale study aims to analyze the deformation mechanisms. Experiments conducted at macro-, meso- and micro-scale are designed to trigger and assess plasticity mechanisms. Compression testing on bulk samples subject to a confining pressure environment and temperature leads to an exclusive brittle failure. The mixed-mode failure mechanisms involve switching between intra- and inter-granular crack propagation, depending on the grain size met by the crack tip. Indentation toughness at meso-scale generates cracks, while TEM analysis of the crack tip area confirms no dislocation activity and 3D-EBSD technique confirms the mixed crack propagation behavior. At micro-scale, micro-pillar compression stress-strain curves and failure mechanisms are comparable with bulk samples testing analysis. These results can be used to provide design guidelines for more crack-resistant TE alloys.

Table of Contents

Acknowledgements.....	iv
Abstract.....	vi
Table of Contents.....	vii
List of Figures.....	xii
List of Tables.....	xx
General Introduction.....	1
Chapter 1: Thermoelectric Materials.....	4
1.1 Thermoelectric principles and power generation.....	4
1.1.1 Thermoelectric effects.....	4
1.1.1.1 The Seebeck effect.....	4
1.1.1.2 The Peltier effect.....	5
1.1.1.3 The Thomson effect.....	6
1.1.1.4 The Kelvin relations.....	6
1.1.1.5 The Onsager relations.....	7
1.1.2 From discovery to advanced engineering.....	10
1.1.2.1 Early development.....	10
1.1.2.2 Semi-conductors for carrier concentration engineering.....	11
1.1.2.3 Novel material structure.....	15
1.1.3 Motivations for new thermoelectric materials.....	18

1.1.3.1 Global context.....	18
1.1.3.2 The thermoelectric module	22
1.2 Mechanical properties of thermoelectric materials	27
1.3 Dislocations and thermoelectric materials	30
1.3.1 Dislocation influence on thermoelectric parameters	30
1.3.1.1 Electrical resistivity	31
1.3.1.2 Seebeck coefficient	32
1.3.1.3 Thermal conductivity	32
1.3.2 Dislocations studies in thermoelectric materials	37
1.3.2.1 Post-processing dislocations	38
1.3.2.2 Deformation-induced dislocations	40
1.3.2.3 Dislocation engineering	41
1.3.3 The case of metallic TE alloys	44
1.4 Half-Heusler thermoelectric alloys	45
1.4.1 Development of the p-type half-Heusler MCoSb.....	45
1.4.2 Properties of the p-type $\text{Hf}_{0.44}\text{Zr}_{0.44}\text{Ti}_{0.12}\text{CoSb}_{0.8}\text{Sn}_{0.2}$	48
1.4.2.1 Synthesis	48
1.4.2.2 Thermoelectric properties	49
1.4.2.3 Mechanical properties and dislocations	51
1.5 Summary	54

Chapter 2	: Experimental methodology.....	58
2.1	Microstructure characterization.....	58
2.1.1	Surface preparation.....	58
2.1.2	Focused Ion Beam (FIB)	58
2.1.3	Scanning Electron Microscopy (SEM).....	59
2.1.3.1	SEM imagery	59
2.1.3.2	Energy-dispersive X-ray Spectroscopy (EDS)	60
2.1.3	Scanning Transmission Electron Microscopy (STEM) and Transmission Electron Microscopy (TEM)	61
2.1.4	Electron BackScattered Diffraction (EBSD).....	62
2.1.5	3D Electron BackScattered Diffraction	64
2.1.5.1	FIB serial sectioning procedure	64
2.1.5.2	Evolution toward 3D-EBSD	65
2.1.6	X-Ray diffraction.....	68
2.1.7	Grain size analysis	69
2.2	Mechanical Characterization.....	70
2.2.1	Classical compression test.....	70
2.2.2	Compression test with hydrostatic pressure environment	71
2.2.4	Mesoscale testing: controlled crack insertion by nanoindentation.....	75
2.2.4.1	Nanoindentation.....	75

2.2.4.2 Controlled crack insertion.....	76
2.2.5 Micro-compression.....	79
2.2.5.1 Pillar preparation.....	79
2.2.5.2 Nanoindentation procedure.....	80
2.2.5.3 The Sneddon correction.....	82
2.2.5.4 Nanoindentation data.....	83
2.3 Summary.....	89
Chapter 3: Results and discussion.....	91
3.1 Metallurgical analysis of $\text{Hf}_{0.44}\text{Zr}_{0.44}\text{Ti}_{0.12}\text{CoSb}_{0.8}\text{Sn}_{0.2}$	91
3.1.1 Crystalline structure and composition.....	91
3.1.1.1 X-Ray Analysis.....	91
3.1.1.2 EDS Analysis.....	92
3.1.2 Microstructure.....	92
3.1.2.1 SEM Observations.....	92
3.1.2.2 STEM and TEM Observations.....	93
3.1.2.3 EBSD analysis.....	96
3.2 Classical compression at ambient atmosphere.....	98
3.3 Compression under confining pressure.....	99
3.4 Mesoscale analysis of controlled crack insertion.....	103
3.4.1 Surface observations.....	103

3.4.2 Tomographic reconstruction.....	106
3.4.3 TEM observation.....	108
3.5 Micropillar compression.....	112
3.5.1 Mechanical testing.....	112
3.5.2 Corrections on micro-pillar data.....	115
3.5.3 Conclusions.....	116
3.5.4 Critical flaw size estimation.....	117
3.6 Summary.....	118
Chapter 4: General discussion, general conclusion and perspectives.....	120
4.1 General discussion.....	120
4.1.1 Native Microstructure.....	120
4.1.2 Ductile versus brittle behavior.....	121
4.1.3 Crack propagation and damage mechanisms.....	123
4.1.4 Guidelines for material development.....	124
4.2 General conclusion.....	125
4.3 Perspectives.....	126
Bibliography.....	129

List of Figures

Figure 1.1: a -Seebeck effect b -Peltier effect.....	5
Figure 1.2: Evolution of Z for near-room temperature thermoelectric materials	12
Figure 1.3: Schematic dependance of thermoelectric parameters on carrier concentration highlighting the optimum power factor where α is the Seebeck coefficient and λ the thermal conductivity	14
Figure 1.4: The evolution of ZT in time. The red triangles represent power generating system, and the blue circles cooling systems.....	16
Figure 1.5: France energy consumption in 2016 in MTeps (P: production, I: import, DS: destock, *including hydroelectric, wind-power, photovoltaic).....	20
Figure 1.6: Estimated U.S. energy consumption in 2016 in Quads, by the Lawrence Livermore National Laboratory	21
Figure 1.7: a -Cooler setup : a current is applied to the device, the heat flow follows the carrier movement, cooling one end and rejecting the heat at the other. b -Generator setup : the heat flux directs the charges where the two semi conductors are separated, creating a potential difference	22
Figure 1.8: An assembled thermoelectric module showing the charge flow for both cooling and power generation setup.....	23

Figure 1.9: Efficiency of a TEG (Eq 1.11) for various ZT values.....	25
Figure 1.10: Main TE materials sorted by ZT vs temperature in 2013.....	27
Figure 1.11: Hardness vs Elastic modulus of various TE materials	28
Figure 1.12: Schematics of one thermoelectric couple in a TEG system	30
Figure 1.13: thermal conductivity vs temperature in LiF for various density of etch pits in slip bands in cm^{-2} for various amounts of deformation. The solid lines are theoretical work from Srpoull and the identified lines are experimental work from Suzuki.....	36
Figure 1.14: Thermal conductivity vs dislocation density in GaN showing a plateau until constant slope decrease	37
Figure 1.15: TEM bright-field images of dislocations in n-type bismuth telluride under two-beam conditions with presence of dipoles (d1, d2) and small loops and a low angle grain boundary (LAGB).	38
Figure 1.16: Video sequences acquired by TEM in Bi_2Te_3 material of free standing dislocations (i) and (ii) at different times, gliding in opposite directions indicated by arrows. The motion of dislocations (i) stopped in front of a dislocation pileup (iii)	39
Figure 1.17: a -phase diagram of $\text{Bi}_{0.5}\text{Sb}_{1.5}\text{Te}_3\text{-Te}$. b - SEM image of melt-spun ribbon of Te-MS material showing the $\text{Bi}_{0.5}\text{Sb}_{1.5}\text{Te}_3$ platelets surrounded by the eutectic	

phase of $\text{Bi}_{0.5}\text{Sb}_{1.5}\text{Te}_3\text{-Te}$ mixture. **c-** Illustration of the dislocation arrays generation during the liquid-phase compaction process. 42

Figure 1.18: ZT vs temperature for each step of sample processing : the green plot is the ingot, the violet the ball milled (BM), the blue plot the melt-spun with stoichiometric proportion (S-MS) and the red plot the melt-spun with an excess of Te (TE-MS). 43

Figure 1.19: Crystal structure of the half-Heusler 46

Figure 1.20: (Ti, Zr, Hf) $\text{CoSb}_{0.8}\text{Sn}_{0.2}$ ternary phase diagram. The ternary compositions are: $\text{Hf}_{0.44}\text{Zr}_{0.44}\text{Ti}_{0.12}\text{-CoSb}_{0.8}\text{Sn}_{0.2}$ (1); $\text{Hf}_{0.65}\text{Zr}_{0.25}\text{Ti}_{0.1}\text{CoSb}_{0.8}\text{Sn}_{0.2}$ (2); $\text{Hf}_{0.45}\text{Zr}_{0.45}\text{Ti}_{0.1}\text{CoSb}_{0.8}\text{Sn}_{0.2}$ (3); and $\text{Hf}_{0.72}\text{Zr}_{0.1}\text{Ti}_{0.18}\text{CoSb}_{0.8}\text{Sn}_{0.2}$ (4). 47

Figure 1.21: Reported microstructure of $\text{Hf}_{0.44}\text{Zr}_{0.44}\text{Ti}_{0.12}\text{CoSb}_{0.8}\text{Sn}_{0.2}$ with **a-** Scanning electron microscopy observation of a fractured surface **b-**Microstructure observed by transmission electron microscopy 49

Figure 1.22: **a-**electrical conductivity, **b-**Seebeck coefficient, **c-**power factor, **d-**thermal conductivity, **e-**lattice thermal conductivity, and **f-**ZT of $\text{Hf}_{0.44}\text{Zr}_{0.44}\text{Ti}_{0.12}\text{CoSb}_{0.8}\text{Sn}_{0.2}$, $\text{Hf}_{0.5}\text{Zr}_{0.5}\text{CoSb}_{0.8}\text{Sn}_{0.2}$, and $\text{Hf}_{0.8}\text{Ti}_{0.2}\text{CoSb}_{0.8}\text{Sn}_{0.2}$. The p-type SiGe has been added in (f) for comparison 50

Figure 1.23: **a-**calculated stress vs. strain of TiNiSn under various slip systems **b-**calculated stress vs. strain of (Ti, Zr, and Hf)NiSn under $\langle 110 \rangle \{111\}$ shear loading..... 53

Figure 2.1: NANOLAB FIB at PPrime Institute, University of Poitiers	59
Figure 2.2: Electron interaction bubble with the scanned surface	60
Figure 2.3: a -Pt layer deposited before FIB milling b -TEM lamella milling under progress c -Lift-out technique under progress d -TEM lamella Pt-welded to the Cu grid before thinning	62
Figure 2.4: EBSD setup	63
Figure 2.5: imagery from EBSD with a 10nm pixel size of the same area seen as: a -SEM image; b -IPF map; c -IQ map; d -Superposition of IQ and IPF map	64
Figure 2.6 illustration of the FIB serial sectioning procedure	65
Figure 2.7: a- Front view of a cubic specimen showing the surface scanned by EBSD b- Upper view highlighting the incident ion milling procedure	66
Figure 2.8: example of a reconstructed volume via 3D-EBSD of Ti-6Al-4V	68
Figure 2.9: Compression Setup at the University of Houston, here equipped with a furnace	71
Figure 2.10: Paterson Machine at the PPrime Institute.....	72
Figure 2.11: Schematics of the pressure vessel and sample column	73
Figure 2.12: schematics of a nanoindenter	75

Figure 2.13 : Cube corner tip profile	77
Figure 2.14: a -Grid of indentation generated with the cube corner tip from 5gf to 30gf b - example of a 20gf (~200mN) indent selected for the study.....	78
Figure 2.15: a -A set of 9 micro-pillars milled out by FIB b -A single micropillar (2x2x6 μm^3) with the Pt layer on the top.....	80
Figure 2.16: Flat punch tip with 10 μm diameter used to compress the pillars.....	81
Figure 2.17: a -pillar surface after pre-loading with Pt debris b -stress-strain curve of a pre- loading.....	82
Figure 2.18: Literature data on nanoindentation loading cycles acquired with a berkovich tip on fused silica with a - load vs. displacement with 120 mN peak load from Oliver and Pharr, and b - load vs. displacement with 120 mN peak load from Guilloneau <i>et al.</i>	84
Figure 2.19: Load controlled loading cycle on fused silica with a Berkovich tip and a 10 mN peak load from the <i>Nanoindenter XP</i>	85
Figure 2.20: indentation loading cycle with the Berkovich tip, from the load control method (black curve) and from the displacement control method (red curve).....	86
Figure 2.21: indentation loading cycle with a flat punch tip	87
Figure 2.22: loading cycles from both methods, showing a displacement over-estimation for the displacement control method.....	88

Figure 3.1: X-ray analysis confirming the half-Heusler phase presence	91
Figure 3.2: a- SEM observation of the surface in backscattered electron mode b- Hf map from EDS scan highlighting an area of high Hf concentration.....	92
Figure 3.3: SEM observation on the surface, revealing only large micrometric grains ...	93
Figure 3.4: a- STEM image showing microstructure and presence of small precipitates within the grains (arrows). b- TEM observation showing the nanostructure	94
Figure 3.5: TEM observation showing small precipitates: a- String of precipitates within a grain,	95
Figure 3.6: dislocations network observed by TEM.....	96
Figure 3.7: EBSD map with a 20 nm step size	97
Figure 3.8: a- location of the EBSD maps for grain size distribution analysis b- grain size distribution for each EBSD map	98
Figure 3.9: a- Stress-strain curve of compression test displaying brittle behavior. b- Fracture surface showing crack propagation in the microstructure	99
Figure 3.10: Stress strain curves for various temperature and pressure conditions.....	100
Figure 3.11: a- main debris rrecovered from a test b- fracture surface showing textured surface c- fracture surface showing a large grain where two fracture plane meet d- combination of large grain cleaved and nanostructured grains decohesioned	

e -crack branching within a grain f -crack propagation from a large grain to a grain boundary.	101
Figure 3.12: Fracture surface displaying nanostructured matrix decohesion and larger grain cleaved.	102
Figure 3.13 : 200 mN indent obtained with a cube corner tip displaying three radial cracks	103
Figure 3.14: a -EBSD (IQ+IPF) map with 20nm pixel size on an indent b -magnified area displayed with superposition of IQ and IPF (left) map with crack highlighted in red (right) c -magnified area displayed with an IQ map (left) with highlighted crack in red (right).....	105
Figure 3.15: Indentation and the selected crack highlighted in red. An estimation of the initial volume extracted is represented by the red dashed line	106
Figure 3.16: a -Top view of the reconstructed volume facing the indent b -View from beneath the volume where the crack reappears through a grain c -Highlighted crack around a large blue grain d -Highlighted crack fracturing two grains in blue and pink	107
Figure 3.17: a -Highlighted crack around a large blue grain b -Highlighted crack fracturing two grains in blue and pink	107
Figure 3.18: volume observed in transparency with the unindexed pixels highlighted in blue.....	108

Figure 3.19: a- An indent with three Pt layer deposited at the crack tips prior to FIB milling b- TEM thin lamella extracted with the micro manipulator	109
Figure 3.20: a- Indent with three radial cracks b- Red highlight of the crack and location of the TEM thin foil extraction area c- In-plane representation of the TEM foil extracted, as observed by STEM.....	110
Figure 3.21: a- TEM observation on extracted thin foil showing in-depth crack propagation with example of branching b- Red highlight of the crack path c- Crack tip area magnification showing no dislocation activity d- crack tip located at a GB without dislocation activity in the three surrounding grains.....	111
Figure 3.22: micropillar geometry	112
Figure 3.23: loading cycles on a micropillar with color-coded max depth, the strain is artificially shifted for display purpose	113
Figure 3.24: Stress-strain curve of micropillar compression	114
Figure 3.25: a- Pillar broken in several large segments b- Fracture surface showing both inter- and intragranular cracking.....	115
Figure 3.26: stress-strain data corrected for the linear curve foot, the Sneddon corrections and the nanoindenter displacement overestimation	116

List of Tables

Table 1: elastic constants determined by nanoindentation	51
Table 2: elastic properties determined by nanoindentation and ultrasonic measurements	51
Table 3:directional young modulus	52
Table 4: hardness and modulus by nanoindentation study for various TE materials	52
Table 5: calculated elastic constants (C_{11} , C_{12} , C_{44}) and related elastic properties: bulk modulus (B), shear modulus (G), Young's modulus (E), Poisson's ration (ν), and ductility index (B/G) of TiNiSn, in comparison with the available theoretical results.....	53
Table 6: Summary of the data recorded from indentations with the Berkovich tip	86
Table 7: summary of the data recorded from indentations with the flat punch tip.....	88
Table 8: summary of the elastic moduli values	115

General Introduction

The thermoelectric (TE) effect describes the capacity of a material to generate electrical energy from a thermal flow and vice versa. Since the discovery of this effect during the 19th century, the thermoelectric science made its first major breakthrough during the years 1950's along with the progress in the field of semi-conductors. The TE efficiency, represented by the figure of merit ZT , depends on the transport parameters of the material: the thermal conductivity, the electrical conductivity and the Seebeck coefficient. Although these parameters are tied to each other, each of them will be individually optimized with specific materials engineering techniques. Among these, the introduction of nanostructured materials lead the value of ZT above 1 in the years 2000's, at a period of time when better energy management became a new guideline for the global research effort.

Indeed, as of today, the major energy production is provided by fossil fuels, and these processes are associated to massive heat loss. Examples for such consumption are ranging from the simple combustion engines in our everyday cars to the larger scale power plant systems. Harvesting the wasted heat would enhance the efficiency of these systems, hence the attention for the thermoelectric materials. Indeed, thermoelectric generator (TEG), built with solid state thermoelectric materials, can harvest this wasted heat and convert it into electricity. This process necessitates no mechanical parts, hence a low cost over time since no maintenance or repairs are needed. In addition, an in-service TEG does not generate pollution.

Among the wide variety of existing TE materials, the Bi_2Te_3 based TE materials are the most widely produced and commercialized, in the form of thin films for cooling in optoelectronic, due to their highest efficiency at low temperature ($\sim 100^\circ\text{C}$). These alloys

are produced also in the solid state but remains as in-lab production due to the toxicity and cost issues. To produce TEG at industrial scale for energy harvesting, TE alloys such as Skutterudite, Pb-Te, and half-Heusler, are developed to match high ZT at higher temperature (500-800°C) and take advantage of a higher temperature difference. While the physical properties of TE materials are well documented, the only mechanical data available in most cases are hardness and elastic modulus values. Easy to obtain through reliable procedures, these data cannot however properly assess the relationship between the innovative microstructures leading to higher ZT and the deformation mechanisms.

As a TEG is built with a sandwich setup, where the TE materials are held in compression between two plates, mechanical data on the TE materials such as compression or flexure strength are required to predict the in-service limit of these devices. Although growing in numbers, studies on the subject are still limited to a few materials. In addition, recent developments assess the possibility to significantly enhance the ZT through phonon scattering mechanisms on dislocations. These scattering mechanisms are well described by theoretical studies and backed up by experimental proof, but comprehensive dislocation studies in TE materials exists only for Bi₂Te₃ based thermoelectric materials. Overall, as the mechanical behavior of TE materials and associated deformation mechanisms gain in interest, the available studies are limited to too few materials.

The present study will assess the deformation mechanisms of the nanostructured thermoelectric alloy p-type half-Heusler Hf_{0.44}Zr_{0.44}Ti_{0.12}CoSb_{0.8}Sn_{0.2}. Developed to reduce environmental and cost impact while maintaining high TE efficiency, this alloy is suitable for TEG application with a peak ZT=1 at 800°C. The proposed study will provide an analysis of the deformation mechanisms of this alloy at the macro- meso and micro-scale

via various original experiments and cutting-edge characterization techniques. Chapter 1 will develop the background that led to high efficiency TE materials, and assess the challenges that arise from dislocation-engineered TE materials. In addition, this section will lay down the development of half-Heusler TE alloys that contributed to the creation of the p-type half-Heusler $\text{Hf}_{0.44}\text{Zr}_{0.44}\text{Ti}_{0.12}\text{CoSb}_{0.8}\text{Sn}_{0.2}$. Based on the available description of this alloy in the literature, an experimental plan is drawn to characterize its deformation mechanisms. The tools used to carry out this experimental plan are described in the technical Chapter 2. Compression testing on bulk samples with confining pressure to enforce plasticity via dislocation activity will contribute to understand the macroscale behavior. At the meso-scale, cracks inserted by nanoindentation toughness method will be subject to Transmission Electron Microscopy observations evaluating plasticity in the crack path vicinity and at the crack tip area. In addition, 3D-Electron Backscattered Diffraction technique will support analysis of the crack path within a volume, according to its microstructure environment. At the micro-scale, compression of micro-pillar milled out by Focused Ion Beam will contribute to a deformation analysis on a reduced volume, to understand the effect of local microstructure. The outcome of these experiments will be presented in Chapter 3. In Chapter 4, these results will be analyzed, and discussed in the general discussion, the key findings of the study will be summarized in the general conclusion, and the perspectives section will lay down the future potential of this research work.

Chapter 1 : Thermoelectric Materials

1.1 Thermoelectric principles and power generation

The thermoelectric (TE) effect describes the inter-dependent character of the phonon and electrons in a material. This translates into the capacity of a material to generate electrical power when subjected to a heat gradient, and the reciprocal applies under the influence of an applied electric current, resulting in a generated heat flux.

1.1.1 Thermoelectric effects

The contemporary thermoelectric science is based upon 19th century discoveries, when the three Physicists Seebeck, Peltier and Thomson have revealed the three major properties of the thermoelectric materials[1], [2]. Currently in use 200 years later in major industries and in a large research community, these properties are an effective alternative for maximizing energy saving.

1.1.1.1 The Seebeck effect

Works led by German Thomas Seebeck in 1821 [3], have revealed the characteristics of a potential difference in a junction of two materials (A and B) presenting a difference of temperature as represented in Fig. 1.1a, where

$$\Delta T = T_{\text{hot}} - T_{\text{cold}}. \quad (1.1)$$

An open circuit electromotive force V is developed between the extremities, described as $V=S_{AB}(\Delta T)$, or $S_{AB}=V/ \Delta T$ where S_{AB} is the Seebeck coefficient between the elements A and B:

$$S_{AB} = S_A - S_B. \quad (1.2)$$

The sign of the Seebeck coefficient varies regarding the nature of the material doping. Thus the coefficient will be $S>0$ for a p-type (ie. hole carrier) and $S<0$ for a n-type (ie. electron carrier), measured in volts per kelvin ($V.K^{-1}$) or more commonly in micro volts per Kelvin ($\mu V.K^{-1}$). The Seebeck coefficient translates the sensitivity of these charges to the heat, the way the carrier concentration gradient will fluctuate when a medium is subject to a heat gradient.

1.1.1.2 The Peltier effect

In 1834, French Jean-Charles Peltier described a heat motion when a current is applied to the junction of two different materials [4] as represented in Fig.1.1b.

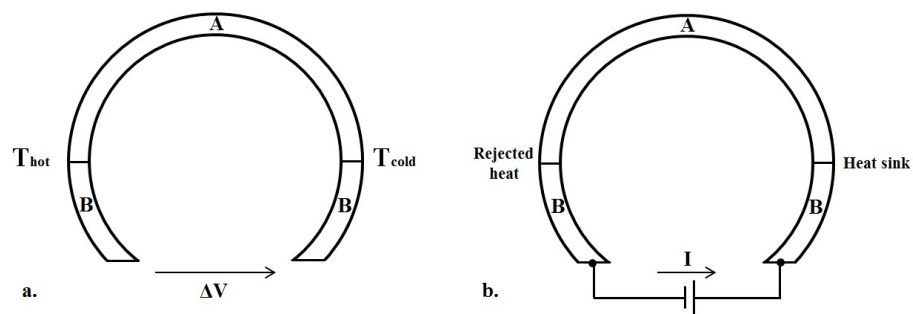


Figure 1.1: **a**-Seebeck effect **b**-Peltier effect

The cold side absorbs the heat while it is rejected on the hot side, according to the following relationship:

$$Q = \Pi_{AB}I, \quad (1.3)$$

where Q is the heat, either absorbed or rejected, Π_{AB} is the relative Peltier coefficient between material A and material B, measured in watts per ampere ($\text{W}\cdot\text{A}^{-1}$) and I is the electric current between A and B. Analogous to the Seebeck coefficient, the relative Peltier coefficient is defined by the two singular coefficients of the materials A and B as:

$$\Pi_{AB} = \Pi_A - \Pi_B. \quad (1.4)$$

1.1.1.3 The Thomson effect

Discovered in 1851 by English William Thomson (later known as Lord Kelvin), the third thermoelectric effect is a combination of principles of the two predecessors [5]. As a material is subjected to both a heat gradient ΔT , with a hot side and a cold side, and an current I , the Thomson effect shows the possibility to relate the rate of heat generation or absorption dQ with the following relationship:

$$dQ = I\beta\Delta T, \quad (1.5)$$

where β is the Thomson coefficient, which has the same units as the Seebeck coefficient ($\text{V}\cdot\text{K}^{-1}$). By convention, the Thomson coefficient is positive for heat absorption by the material when the current direction goes from the hot to the cold side.

1.1.1.4 The Kelvin relations

The three thermoelectric parameters described previously were combined in a single relationship by Lord Kelvin, with the following formulations [6]:

$$S_{AB} = \Pi_{AB}/T \quad (1.6)$$

and

$$\frac{dS_{AB}}{dT} = \frac{\beta_A - \beta_B}{T}. \quad (1.7)$$

These relationships demonstrate a direct link between the three thermoelectric parameters. The Eq.1.6 provides with an easier way to measure the Peltier coefficient, by measuring the Seebeck coefficient. The latter being an electrical measurement, a property much easier to measure than a temperature gradient along the material. In addition, the second relationship (Eq.1.7) allows calculating the relative Seebeck coefficient through the measurement of the Thomson coefficient. Overall, these relationships show the indivisible properties of the thermoelectric coefficients.

1.1.1.5 The Onsager relations

The reciprocal relations of Onsager express a symmetry in the mutual coupling of two or more irreversible processes occurring simultaneously in a system [7], [8]. These relations follow a thermodynamic reasoning, plus the additional fact that the laws of dynamics are symmetric with respect to future and past in the absence of a magnetic or Coriolis force field.

The macroscopic laws, which govern the process of rates of change of a set of measurable parameters (α_i), such as the Fick's law of diffusion or Ohm's law of electric conduction, can be expressed as

$$\frac{\delta \alpha_i}{\delta t} = \sum_j L_{ij} \gamma_j, \quad (1.8)$$

where γ_j is the driving force, and equals zero at equilibrium ($\gamma_j = \delta S / \delta \alpha_j$, with S for the entropy), and where the L_{ij} are the kinetic coefficients, are functions of the state of the system, as a measure of the coupling of the j th process on the course of the i th. The Onsager's theorem states that

$$L_{ij} = L_{ji}, \quad (1.9)$$

As the thermoelectric effect is the outcome of the mutual coupling of a heat flow, and an electric current flow in a system, the Onsager theorem applies to these entities. Based on the thermodynamics definition of heat,

$$Q = TS = W - \mu J, \quad (1.10)$$

where Q is the heat current density, T the temperature, S the entropy current density, W the energy current density, μ the electrochemical potential and J a particle current density. From this point, it was demonstrated [9] that Q and J are related by the Onsager parameters, in the absence of an applied magnetic field as

$$-J = L_{11} \frac{1}{T} \nabla \mu + L_{12} \nabla \frac{1}{T}, \quad (1.11)$$

and

$$Q = L_{12} \frac{1}{T} \nabla \mu + L_{22} \nabla \frac{1}{T}, \quad (1.12)$$

where the two equations share the parameter L_{12} . The heat conductivity (κ) can be determined from Eq. 1.11 and Eq. 1.12, from its definition as the heat current density per unit temperature gradient for zero particle current ($\kappa = -Q/\nabla T$ for $J = 0$) and expressed as $\kappa = \frac{1}{T^2 L_{11}} (L_{11} L_{22} - L_{12}^2)$. The electric conductivity (σ) is defined as the electric current density (eJ) per unit potential gradient [$(1/e) \nabla \mu$] in an isothermal system, so it is expressed as $\sigma = \frac{-eJ}{(1/e) \nabla \mu}$ for $\nabla T = 0$, hence the expression $\sigma = \frac{e^2 L_{11}}{T}$. From Eq. 1.10, Eq. 1.11 and Eq. 1.12, it is possible to express the entropy as

$$S = -\frac{L_{12}}{T L_{11}} J + \frac{(L_{11} L_{22} - L_{12}^2)}{T L_{11}} \nabla \frac{1}{T}. \quad (1.13)$$

From this expression, and the expression of the electrical and thermal conductivity, by identifying the term $S_j = -\frac{L_{12}}{T L_{11}}$, the Onsager parameters can be expressed as $L_{11} = \frac{T}{e^2} \sigma$; $L_{12} = -\frac{T^2}{e^2} \sigma S_j$; and $L_{22} = \frac{T^3}{e^2} \sigma S_j^2 + T^2 \kappa$.

From the physical definition of each of the thermoelectric coefficients, it is possible to derive their individual expressions from the expressions of the total energy of the system (Eq. 1.10) and the entropy (Eq. 1.13) which includes the Onsager parameters, whether it is a junction formed by two materials A and B (Peltier effect, Seebeck effect) or a single material (Thomson effect):

-Peltier coefficient: $\Pi_{AB} = \frac{T}{e} (S_j^B - S_j^A)$

-Thomson coefficient: $\beta = \frac{T}{e} \frac{dS_j}{dT}$

-Seebeck coefficient: $S_{AB} = \frac{1}{e} (S_j^B - S_j^A)$

These expressions directly lead to the Kelvin relations:

-Kelvin relations: $\Pi_{AB} = T S_{AB}$; $\beta_B - \beta_A = T \frac{dS_{AB}}{dT}$

1.1.2 From discovery to advanced engineering

1.1.2.1 Early development

The basis of the thermoelectric effect was settled by the mid-19th century. In this era of industrial development, the major focus of the scientific community was on metals and metallic alloys. Seebeck's discovery was the interaction of the electric charge with the heat gradient of semi-conductors, which presents a major carrier type depending on its doping. In opposition, a metal has a less distinctive carrier concentration thus leading to poor thermoelectric properties, even though they exist, causing an additional loss of interest in the field. Nevertheless, the raise of the electromagnetism science and the development of thermodynamics, set within a noteworthy energy conversion theme, supported Kelvin's work in the 1850's with his all-in-one relationship.

Based on Rayleigh's work on efficiency of the thermoelectric process [10], Altenkirch. successfully produced a theoretical model by 1909 a thermoelectric energy generation and refrigeration [11]. To allow the thermoelectric generator (TEG) reaching higher efficiency, the Seebeck coefficient has to be large, while a low thermal conductivity is necessary to

retain the heat at the junction, and finally a low electrical resistivity is required to reduce the Joule heating.

All these conclusions were transposed into a figure-of-merit, the so-called ZT, expressed as

$$ZT = \frac{S^2 \sigma T}{\kappa}. \quad (1.14)$$

In this formulation, Z has the dimension of the inverse of the temperature ($1/K$), S the Seebeck coefficient, σ the electrical conductivity, κ the thermal conductivity and T the absolute temperature, ZT is dimensionless.

1.1.2.2 Semi-conductors for carrier concentration engineering

It was found that semi-conductors reach values about $100 \mu\text{V/K}$, some of them even reaching values close to $1000 \mu\text{V/K}$, as opposed to metals which were only showing values of $10 \mu\text{V/K}$. In the 1940's and 1950's, the early stage of development took place. This was the time for realization that electronic engineering was needed to reach a higher ZT, which launched a period of 20 years of progress on the enhancement of the Seebeck coefficient [12]. Two notable alloy groups emerged, the Bi_2Te_3 -based and Pb-Te-based alloys. During the 1950's, Goldsmid [13] in the UK demonstrated the possibility of maintaining 26°C of cooling with a thermocouple consisting of Bi_2Te_3 and Bi. In addition, Ioffe in the Soviet Union led research on both cooling and power generation [14]. Fig. 1.2 shows the evolution of from the Bi alloys to the optimized, more complex BiTe alloys [1].

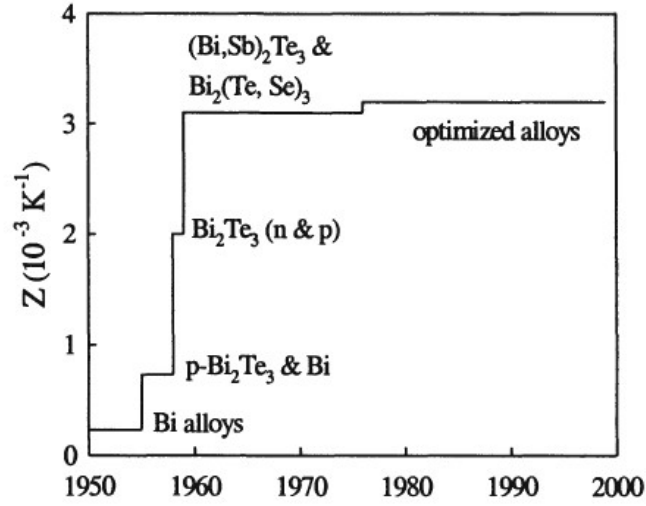


Figure 1.2: Evolution of Z for near-room temperature thermoelectric materials

Although offering a high Seebeck coefficient, the semi-conductors do not provide an electrical conductivity as high as the metals, but still more than any insulator, having an high intrinsic electrical resistivity. This is due to the relationship between the Seebeck and the carrier concentration, for metals and degenerate semi-conductors [15] (for nearly free electrons) posed as

$$S = \frac{8\pi^2 k_B^2}{3eh^2} mT \left(\frac{\pi}{3n} \right)^{2/3}, \quad (1.15)$$

where n is the carrier concentration and m the effective mass of the carrier and k_B the Boltzmann constant. The value of the Seebeck coefficient decrease with higher carrier concentrations, whereas the electrical conductivity σ would evolve as

$$1/\rho = \sigma = ne\mu, \quad (1.16)$$

where μ is the carrier mobility and ρ the electrical resistivity. Hence the electrical conductivity drops with lower carrier concentration. The advantage of the semi-conductor

alloys is to be able to tune the carrier concentration to maximize the electrical conductivity, without dropping the Seebeck coefficient value in a range too low to be interesting. A proper carrier concentration can maximize the power factor ($S^2\sigma$), which is the electrical figure found in the numerator of the expression for ZT (Eq.1.14). This is a parameter often reported in the thermoelectric literature in parallel to the ZT value. The maximum power factor can only be obtained in the semi-conductor domain, represented in Fig 1.3 [2].

In addition to the electronic parameters, the carrier concentration also interacts with the thermal conductivity. At the denominator of ZT (Eq.1.14), the total thermal conductivity can be detailed as $\kappa = \kappa_L + \kappa_E$, the sum of the lattice thermal conductivity κ_L (carrier independent) and an electronic contribution κ_E . The latter is related to the electrical conductivity through the Wiedemann-Franz law:

$$\kappa_E = L\sigma T = ne\mu LT, \quad (1.17)$$

where L is the Lorenz factor taken as $2.4 \times 10^{-8} \text{ J}^2\text{K}^{-2}\text{C}^{-2}$ a fixed value for free electrons (degenerate limit) [16]. Since the charge carriers transport both heat and charge, this relationship is commonly used to estimate κ_E from σ . Then κ_L is estimated by subtraction of κ_E from the total thermal conductivity. However, the value of L is not a constant and vary with carrier concentration toward lower values causing uncertainties, adding up to uncertainties from the bipolar thermal conductivity term [17], [18].

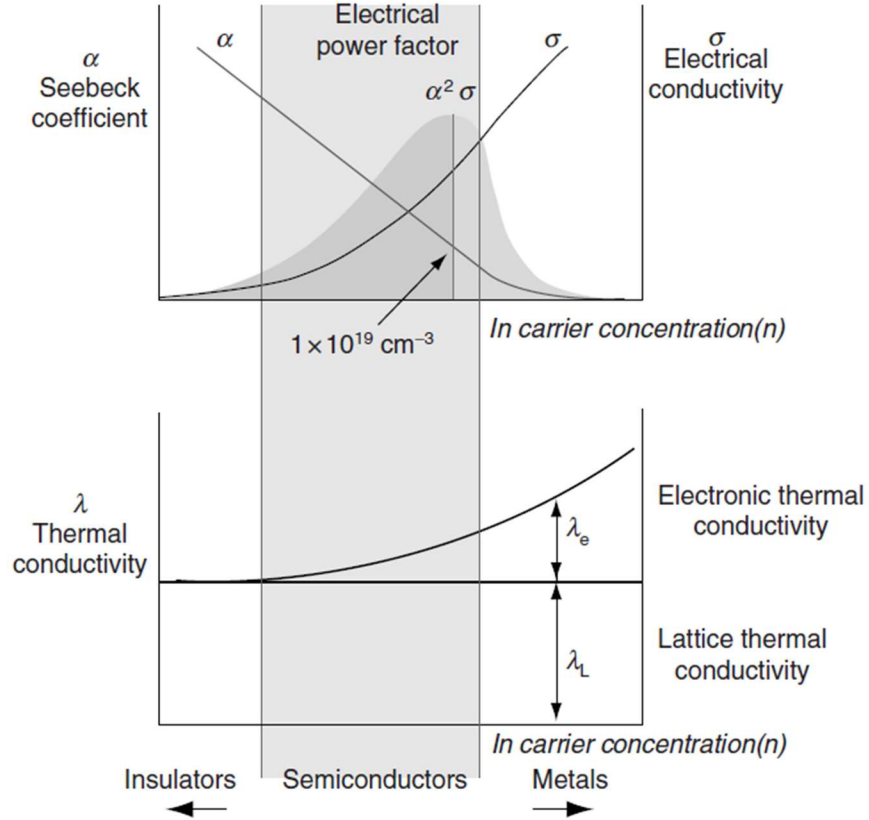


Figure 1.3: Schematic dependence of thermoelectric parameters on carrier concentration highlighting the optimum power factor where α is the Seebeck coefficient and λ the thermal conductivity

A material with a high ZT is expected to have high electrical conductivity and low thermal conductivity. However, this is restricted by the Wiedmann-Franz law, which represents an intrinsic conflict for achieving high thermoelectric efficiency. In the assumption of a high ZT material with a very low thermal conductivity and very high electrical conductivity, rewriting the ZT expression with the electrical conductivity and κ_E expressions (Eq.1.16, Eq. 1.17) where $(\kappa_L/\kappa_E) \ll 1$, leads to

$$ZT = \frac{S^2/L}{1 + \frac{\kappa_L}{\kappa_E}}, \quad (1.18)$$

where The ZT is defined now by the Seebeck coefficient.

These developments for higher electrical properties were fruitfully used by industry, applied for domestic refrigeration, cooling system, and spacecraft power generator for deep space missions by assembling TE modules. To satisfy these applications, three categories of thermoelectric were predominant in the 1970's, covering different temperature range of optimum run. The first group is the Bismuth Telluride and its associated alloys such as Sb_2Te_3 and Bi_2Se_2 . All present a maximum $ZT=1$ for both n- and p-type, and are mainly used for refrigeration with a maximum working temperature around 180°C . Two other groups, with the Group IV tellurides such as PbTe , GeTe and SnTe ($ZT\sim 0.8$) and the Silicon Germanium and its alloys ($ZT\sim 0.6$) were used for power generation, for respectively a maximum operating temperature of respectively 700°C and 1000°C . The key to fit these alloys to application is to adjust the carrier concentration, allowing ZT optimization by adjusting the maximum ZT peak at the desired temperature.

1.1.2.3 Novel material structure

For over 30 years, $ZT=1$ was commonly referred as the upper limit for thermoelectric applications leaving the community with low dynamism in the field. However, in early 1990's, the US and the French Navy addressed a request for new ideas in increasing ZT to Mildred Dresselhaus of the Massachusetts Institute of Technology. In 1993, with her PhD Student Lyndon Hicks, they published what became a major breakthrough in the thermoelectric community, with the prediction of an increased ZT using small scale structures, thin films where the electrons are confined in quantum wells [19]. Prediction on 4nm thick layers of Bi_2Te_3 quantum wells presented a factor of 2 in ZT increase, and a factor of 3 for 2 nm thick wells, compared to 3D bulk material. Then Hicks and Dresselhaus

assessed the ZT of the 1D compared to the bulk, proving that nanowires have even higher ZT than 2D materials [20].

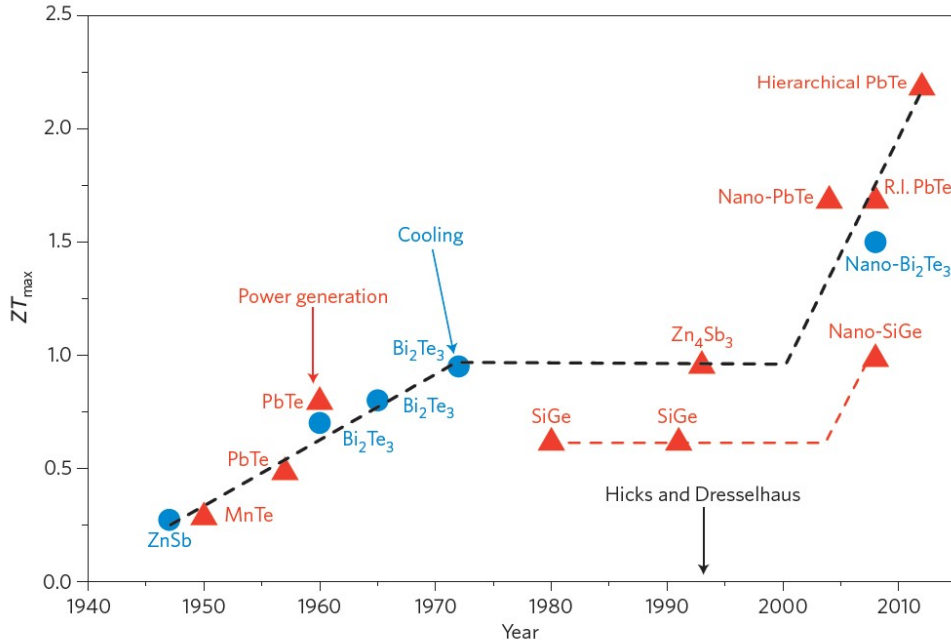


Figure 1.4: The evolution of ZT in time. The red triangles represent power generating system, and the blue circles cooling systems

With such concept, one can engineer the electronic structure in a novel way. By confining the electron wave function in one or two dimensions through nanostructuring, it is possible to tune the electronic density of states and so the power factor. Also combined for the first time with the electronic properties, Hicks and Dresselhaus have assessed the effect of a reduced phonon mean free path due to interface scattering, suggested via superlattice. A nanostructured bulk interacts on both phonon scattering and spectra through interacting with phonon mean free path and phonon wave vector respectively. These processes describe the heat wave diffusion, and so the thermal conductivity, offering possibility of engineering this parameter. These studies initiated a new wave of attention in the TE field, as shown in Fig.1.4 [21] where the ZT value raised again since the early

2000's. However, the first attempts of increasing ZT were done by a strict application of the described study, with thin films and nanowires, which is only suitable for micro-electronic but not for larger dimension scale. The goal is to aim for a 3D device, made of ingots to build a thermoelectric generator, enabling generation of a decent amount of power from a heat source. In bulk materials, this involves to lower the grain size to a nanoscaled microstructure. This was first accomplished in 2004 by Hsu et al. [22] with nanostructured clusters in a matrix leading to a doubled ZT in PbTe-based alloy, and then in 2008 by Poudel et al. [23] with a bulk-nanostructured Bi₂Te₃-based alloy. These works showed a 50% increase in ZT. The Hicks and Dresselhaus theory led to a breakthrough with a TE material with $ZT > 1$, showing that not only the nanostructure is necessary, but a fine tuning at atomic, nanoscale, and mesoscale is possible. An example of this is demonstrated with the PbTe endotaxially nanostructured with SrTe at 4 mole percent and mesostructured with powder processing and spark plasma sintering, where the ZT was raised to 2.2 at 915K [24] as reported in Fig.1.4. This material has a specific chemical composition, contains nanoprecipitates and the SPS method ensure a homogeneous refined grain size.

Since reduction of the thermal conductivity leads to promising results, the process will eventually reach the amorphous limit in bulk materials, considered as the lower limit the thermal conductivity can reach on a material with the same chemical composition. As the maximum level of disorder is reached, the phonon scattering is maximal as well, and consequently their lifetime and mean free path are minimal [25]. In addition, in nanostructured materials, the Seebeck coefficient is predicted to be higher as well [19], [20], and investigations for enhancements of the electronic properties were conducted, with remarkable results. In PbTe the ZT was doubled to 1.5 at 773K with distortion of the

electronic density of states [26], convergence of the electronic bands raised the ZT of PbTeSe to 1.8 at 850K [27]. This shows that even with low thermal conductivity through nanostructure, the work on electronic properties, although occasional, may be paving the way for future TE materials.

1.1.3 Motivations for new thermoelectric materials

1.1.3.1 Global context

In parallel to the scientific developments in the TE field, the recent progresses are also motivated by the heavy concerns about energy. Indeed, the early 21st century is witnessing a critical turn in the energy field as fossil energies became questionable regarding processing, availability, and pollution, in a context of constantly growing energy demand. The US energy consumption in 2016, reported in Fig.1.6 [28], shows how the energy, produced from different power sources, is used and rejected. Over the year 2016, only 34.2% of the produced energy has been serviced while the rest was rejected, massively from electricity generation and transportation fueling. Furthermore, this trend was not restricted to 2016 but observed in the precedent years as well.

Similar observations regarding the energy production in France for the year 2016 can be made with 36% of energy rejected before consumption, as reported in the chart Fig.1.5 [29]. Although the France energy chart do not detail how the energy is serviced, similar conclusion can be drawn between the two countries by comparing the energy loss associated to both electricity production and transportation:

1) In both cases, there is more energy lost than consumed through electricity generation. Whereas France is massively relying on the nuclear for electricity production, the U.S are relying on a variety of energy resources such as coal and natural gas in addition to nuclear. All these processes result in massive energy loss through heat rejection since electricity is generated by steam turbine which is associated to escaping heat.

2) Petroleum products consumption is similar in both countries, representing around 35% of the total energy consumption. The US chart shows that the transportation field is rejecting 75% of the input energy. This rejection occurs mainly through combustion engines, due to characteristically low thermodynamic efficiency associated to heat loss.

The thermoelectric material comes as a solution since the wasted heat energy can be converted in electrical power. To do so, the first step is to build a thermoelectric couple containing a p- and an n-type TE material that must be selected regarding their maximum ZT temperature. In addition, considering the future service environment, one must assess their mechanical reliability before assemblage as a module which would be placed at the heat source for generating electricity, and perhaps mechanical stress.

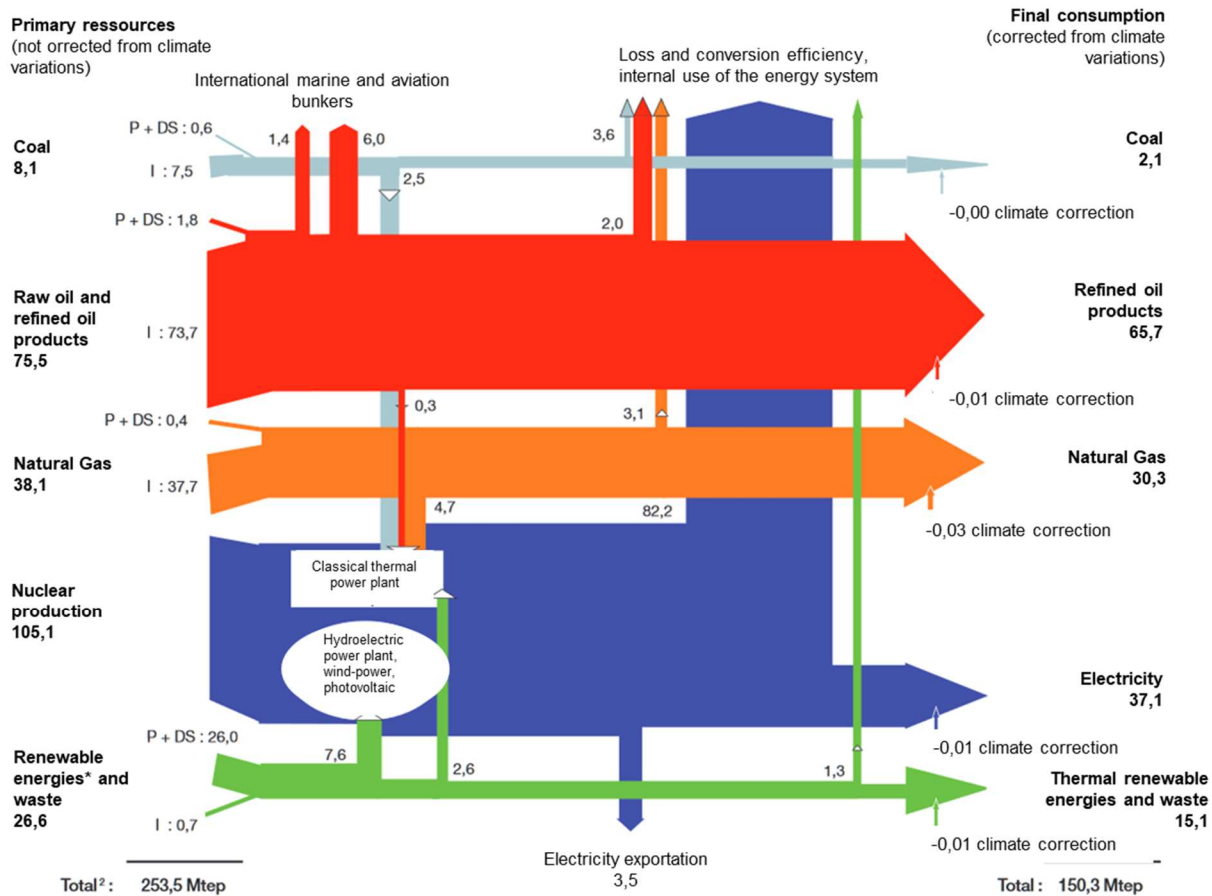


Figure 1.5: France energy consumption in 2016 in MTeps (P: production, I: import, DS: destock, *including hydroelectric, wind-power, photovoltaic)

1.1.3.2 The thermoelectric module

A thermoelectric couple, which can be used either as a generator or a cooler, contains both p- and n- type TE materials which are connected electrically in series and thermally in parallel. They are connected by an electrical conductive material with low TE properties, while they are sandwiched between ceramic plates for electrical insulation and in favor to the thermal flow. The thermoelectric couple is represented in Fig.1.7 [30], and has the same design for either demonstrating the Peltier effect for cooling or the Seebeck effect for power generation.

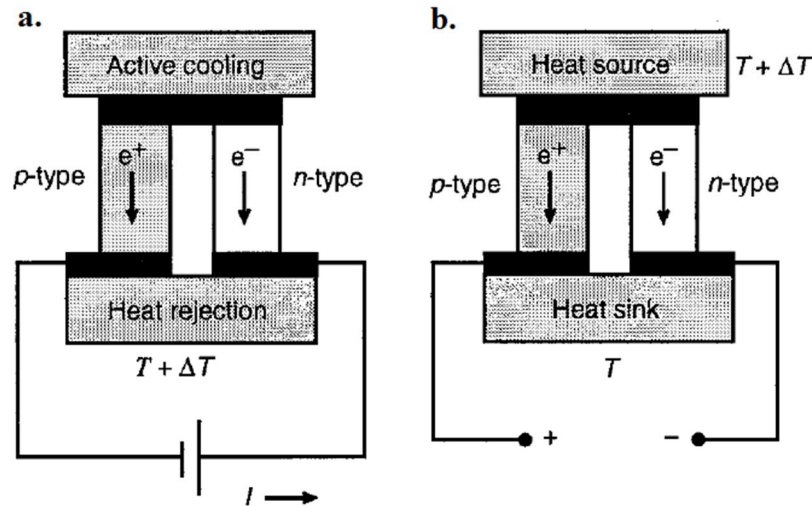


Figure 1.7: **a**-Cooler setup : a current is applied to the device, the heat flow follows the carrier movement, cooling one end and rejecting the heat at the other. **b**-Generator setup : the heat flux directs the charges where the two semi conductors are separated, creating a potential difference

The cooling setup is represented in Fig.1.7a, where a current I is applied to the junction initially in a stable state. This causes a response in the charge repartition in the junction, dragging the charge carriers to one side, triggering the pumping process of the calories, from the cooling end to the heat rejection end. The power generation setup is represented in Fig.1.7b where the couple, initially in a stable state, is subject to a heat flow

which now drives the charges along its path to the heat sink end. This process takes the thermoelectric couple out of equilibrium state, where the new charge repartition will generate an electrical current. The output voltage is determined by Seebeck coefficient of the couple in proportion to the temperature difference ($V=S\Delta T$).

The TE materials are assembled as a TE couple which is considered to be a reliable apparatus for two reasons. First because of the nature of a thermoelectric module; they are made of non-mobile parts, with no liquid involved or machinery and then no maintenance needed. Then, such an apparatus can be down-scaled as in opto-electronics for cooling of infrared sensors.

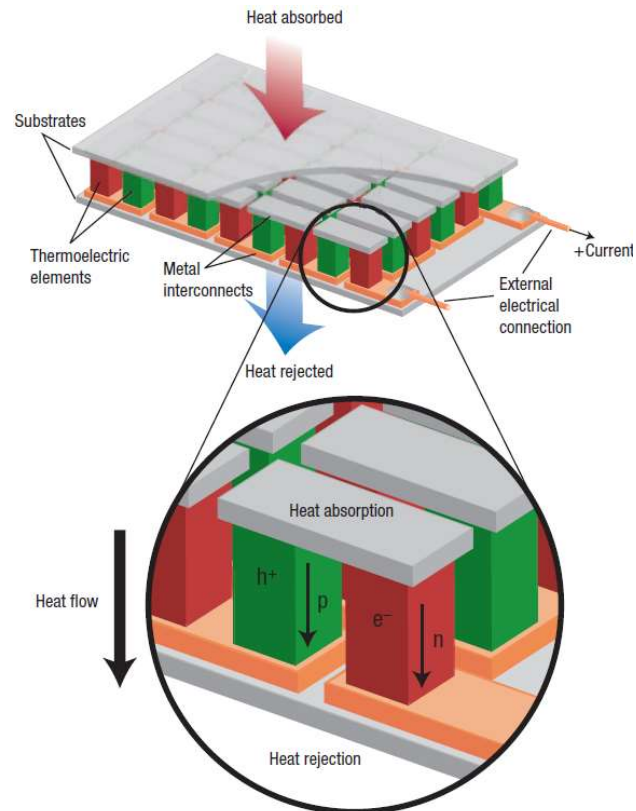


Figure 1.8: An assembled thermoelectric module showing the charge flow for both cooling and power generation setup

These modules designed for power generation can be assembled in series as a thermoelectric generator (TEG) as represented in Fig. 1.8 [31]. The assembly is constituted of two ceramic plates holding the TE couples connected to the open circuit. The generator setup is commonly used in space programs, as on the *Pionner* and *Voyager* spacecrafts, where too far from the sun for solar powered systems, the generator provides power from the radioisotopes heating (Radioisotopes Thermoelectric Generator, “RTG”). In this case, these devices take advantage of high ΔT caused by low temperature environment. For instance during the manned Apollo missions on the moon, a RTG was used as a portable generator, providing power to scientific experiments, with no failure reported.

With no moving parts likely to fail or wear out, the TEGs represents highly reliable devices. For instance, up to now, the NASA has accumulated over 300 years of service for missions with RTG. The Peltier cooler setup is commonly found in opto-electronics, for small scale cooling systems using thin films-scaled apparatus. It is also used in commercial heating/cooling system in car seats with bulk scale devices. The latter were developed in 1998 by Gentherm, which sold for this product over half a billion USD [21]. As the thermoelectric involvement in the energy field seems quite isolated, the recently developed TE materials brings new insights and possibilities about enhancing the energy output of a thermal system with higher ZT and novel processing routes.

The figure of merit, ZT , may efficiently characterize a single material but characterizing a TEG requires extra considerations. Indeed, such a TE apparatus is characterized by its efficiency, calculated as the ratio of the electrical energy produced W_{elec} to the thermal energy absorbed by the hot face Q_H , for which the expression Eq.1.19 includes the ZT of the module as a parameter with

$$\eta_{max} = \frac{W_{elec}}{Q_H} = \frac{\Delta T}{T_H} \cdot \frac{\sqrt{1 + ZT} - 1}{\sqrt{1 + ZT} + \frac{T_C}{T_H}} \quad (1.19)$$

where the $T = (T_H + T_C)/2$ as the average temperature between the hot and the cold side. The parameter Z of the two TE materials constituting the junction can be expressed with the thermal conductivities κ_n and κ_p , the Seebeck coefficients S_n and S_p and the electrical conductivities σ_n and σ_p , as

$$Z = \frac{(S_p - S_n)^2}{\left[\left(\frac{\kappa_p}{\sigma_p} \right)^{\frac{1}{2}} + \left(\frac{\kappa_n}{\sigma_n} \right)^{\frac{1}{2}} \right]^2} \quad (1.20)$$

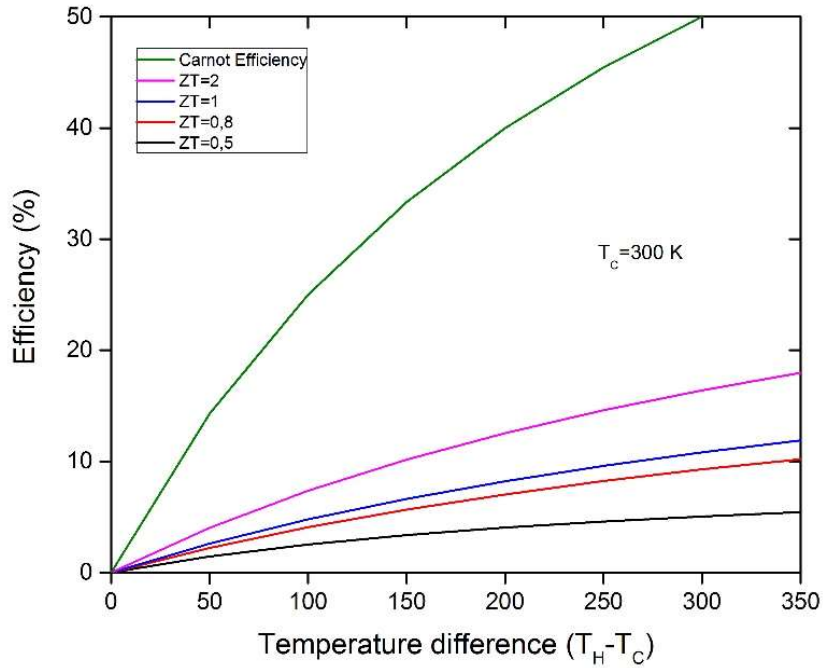


Figure 1.9: Efficiency of a TEG (Eq 1.11) for various ZT values

The efficiency versus ΔT for various values of ZT is reported in Fig.1.9, and are compared to the Carnot efficiency, where $ZT=1$ with a $\Delta T=300K$ corresponds to a 10% efficiency. On one hand this is an encouraging picture for laboratories and manufacturers as the newly developed alloys provide a ZT between 1 and 2. But as the TEG goal is to harvest wasted energy, possibly at a large industrial scale, the environmental and cost arguments must be considered.

For instance, the Pb-based TE alloys, regardless of how attractive the ZT at mid-range temperatures, these materials are environmentally toxic, and must be replaced by other alloys or compositions. In addition, the cost-associated issues due to expensive elements are moving the field to provide variations of TE alloys compositions, while not downgrading the ZT . Finally, the recent progress in the TE field are associated to more complex microstructures over time, necessary to provide high ZT materials. Considering all these parameters, the conception of a higher efficient TE modules becomes subtle.

As the generation of enhanced nanostructured thermoelectric materials is currently studied and produced in research laboratories, and closing on viable applications, industrial scale production will require more than just a good ZT value. Indeed, such alloys, assembled in a TEG, will require to be as well competitive when it comes to mechanical reliability. For the medium range temperature (300°C to 500°C), various alloys can be considered. As shown in Fig.1.10 [32], the half-Heusler alloys have a correct $ZT\sim 1$ at medium temperature even though lower than its competitors, PbTe/PbSe and Skutterudite. However, the toxicity and the anticipated weak mechanical properties of the Pb-based materials along of Skutterudite downsides such as low thermal stability and elements

limited supplies [32], make the half-Heusler good compromise for the medium temperatures.

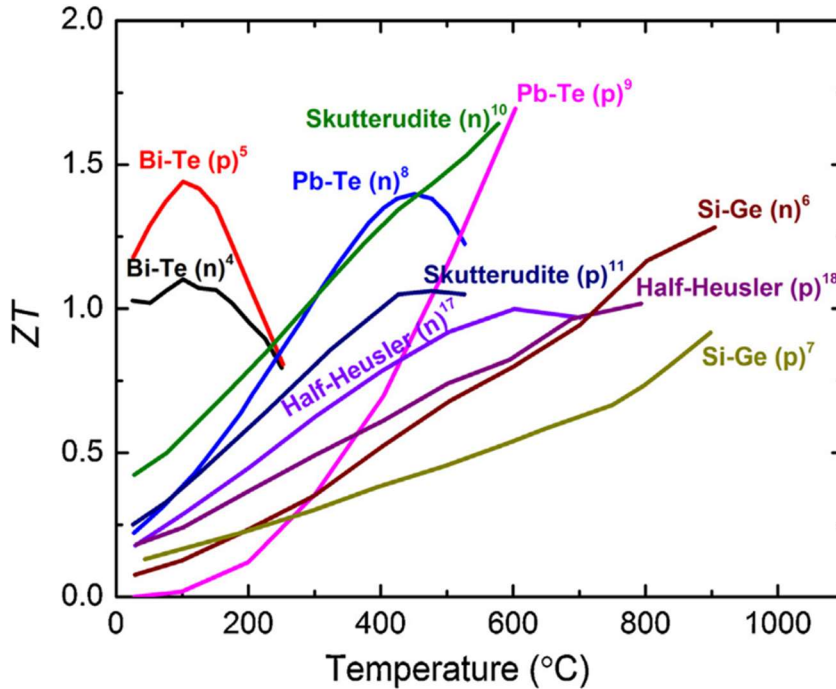


Figure 1.10: Main TE materials sorted by ZT vs temperature in 2013

Considering that the exhaust gas in a car engine are is 500°C, the idea of generating power from this heat has motivated several companies to develop a TE generator fitting to such application [21]. The knowledge of the ZT by itself is insufficient, indeed the mechanical properties of these alloys are of equal importance, to obtain alloys matching the service environment.

1.2 Mechanical properties of thermoelectric materials

Hardness and elastic modulus are the two main mechanical properties studied TE materials, using respectively Vickers hardness and Resonance Ultrasound Spectrometry [33]–[35]. Recently, deeper insights in mechanical properties of TE materials were gained via measurement of the elastic properties of a nanostructured half-Heusler, through

combined nanoindentation and AFM study [36]. In addition, the nanoindentation/AFM combination have provided a comparison table of nanoindentation hardness and elastic modulus between the TE categories [37].

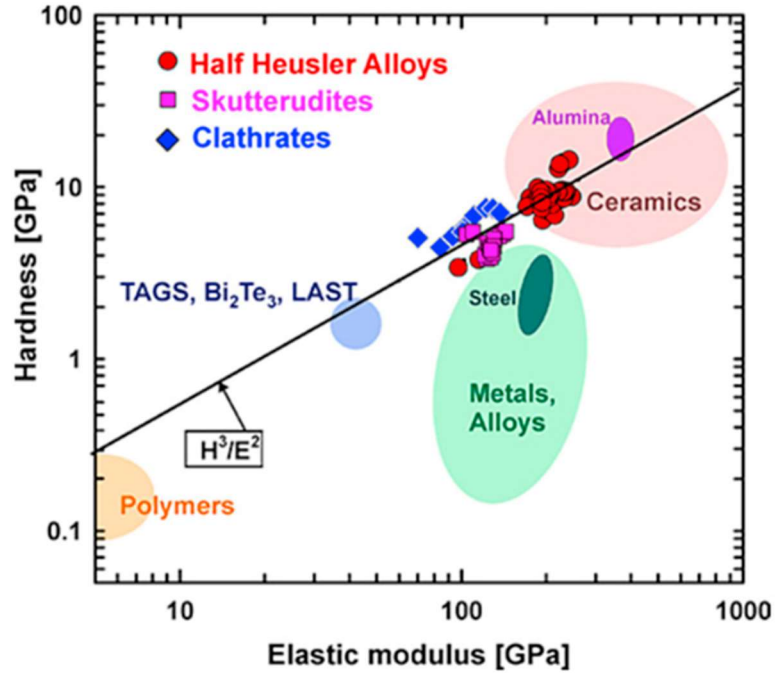


Figure 1.11: Hardness vs Elastic modulus of various TE materials

The TE materials are commonly known as brittle [38], and a hardness versus elastic modulus diagram such as the Fig.1.11 [35] shows half-Heusler alloys are comparable to ceramics regarding these parameters.

The elastic modulus directly influences the fracture toughness (K_{IC}) of a material. Estimations of half-Heusler fracture toughness shows $1.8 \text{ MPa}\cdot\text{m}^{1/2} < K_{IC} < 2.3 \text{ MPa}\cdot\text{m}^{1/2}$ [35], whereas the values for Skutterudites will be lower ($1.1 \text{ MPa}\cdot\text{m}^{1/2} < K_{IC} < 2.2 \text{ MPa}\cdot\text{m}^{1/2}$) [39]. Among the TE materials with the lowest elastic moduli, the K_{IC} value for Bi_2Te_3 alloys stands around $1 \text{ MPa}\cdot\text{m}^{1/2}$, and for PbTe $K_{IC} < 0.5 \text{ MPa}\cdot\text{m}^{1/2}$ [40].

Additional data from bending tests are available, with examples on Bi_2Te_3 systems [41], [42], Skutterudite [43], Pb-Te based alloy [34], but these experiments are still uncommon, confined to few alloys for certain TE materials. One of the reasons for the paucity of these mechanical properties is because the TE community relies solely on the hardness and elastic modulus, which is considered as a tool of comparison for processing. Indeed, to adjust the compound proportions of an alloy to be processed, one will consider favoring a good match between TE properties and mechanical properties. But the industrial interest in such materials requires the knowledge of the mechanical behavior, in accordance to its physical properties. Indeed, a TE device, although efficient, must maintain a good resistance against mechanical solicitations. Finally, at a deeper level of understanding, the deformation mechanisms, involved in the TE alloys failure process, are also absent from the literature.

Crack opening and propagation, as well as dislocations production, are phenomena which are competing to lead to the material failure under various stress conditions. For instance, a severe plastic deformation (SPD) process, the high-pressure torsion (HPT), was used to refine the grain size in Skutterudite [44]–[47]. Extremely brutal, the HPT generates micro cracks and dislocations. The study of annealing on TE parameters may suggest these generated defects have a consequent impact on ZT.

In addition to the material itself, environmental stress must be considered. The design of a TEG is quite complex, as each TE leg is connected by a welded metal for electrical conductivity, while sandwiched in compression between ceramic plates as represented in Fig 1.12 [38]. In a single TEG, the large number of connections between the p and n legs are a possible source of early cracking due to interface mechanics.

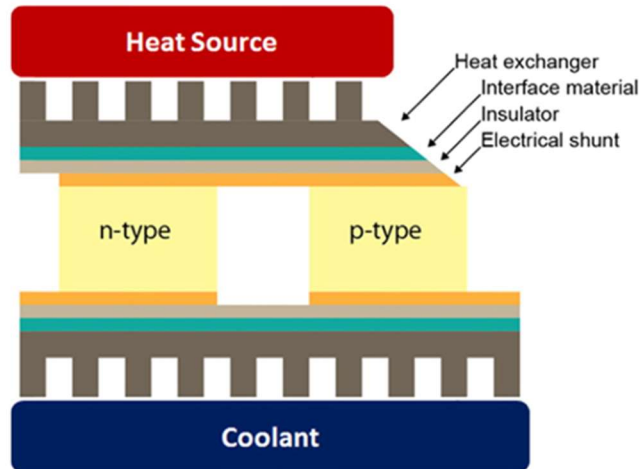


Figure 1.12: Schematics of one thermoelectric couple in a TEG system

In a single TE leg, the heat gradient between, the hot and the cold size results in a coefficient of thermal expansion gradient along the leg [48]. The material expansion is restricted by the sandwich setup, where the successive TE couples are held in compression between the ceramic plates. These design considerations add numerous sources of stress to the TE materials which yield the necessity of a deeper understanding of the mechanical properties and deformation mechanisms of the TE materials. In addition, defects are now engineered toward higher ZT , such as the dislocations which are known to interact with the physical properties of TE materials. Nevertheless, isolating the effect of a defect to influence the material ZT can be a challenging task.

1.3 Dislocations and thermoelectric materials

1.3.1 Dislocation influence on thermoelectric parameters

The thermoelectric effect must be considered as a set of three physical parameters, used into the expression of ZT : the electrical resistivity, the Seebeck coefficient and the

thermal conductivity. When a phenomenon is reported to influence the ZT, its individual effect on the three TE parameters must be considered.

1.3.1.1 Electrical resistivity

The dislocation resistivity has been widely studied in metals, in which the electrical conductivity is a critical point. R.A. Brown [49] has developed, based on theoretical development and in comparison with experimental measurements, a relationship linking the electrical conductivity and the dislocation density. This relationship is expressed as

$$\Delta\rho = \frac{4\hbar V_0\beta}{e^2 \sum_j n_j}, \quad (1.21)$$

where ρ is the electrical resistivity, β the dislocation density length per unit volume, \hbar the Planck constant, V_0 the primitive cell volume (*ie.* fermi volume), j the index on the Fermi surface, n_j the number of carriers per primitive cell inside sheet j of the Fermi surface. A correction for a random distribution is imported from Kaner and Ferldman and expressed as

$$\left(\frac{\Delta\rho}{\beta}\right)_{random} = \frac{8\hbar V_0}{3e^2 \sum_j n_j}. \quad (1.22)$$

Expressed in terms of dislocation density, Eq. 1.22 provides a figure for the effect of dislocations on both carrier types, independently from the band or metal. This relationship predicts a linear increase of the electrical resistivity with the dislocation density, due to the the associated lower carrier mobility.

1.3.1.2 Seebeck coefficient

Silicon nanowires have shown an influence with the introduction of dislocation and dislocation loops, enhancing the Seebeck coefficient by widening the band gap. The introduced dislocations filter the low-energy carriers by creating a potential barrier, however such defects are slowing down the carriers, causing higher electrical resistivity [50]. In Si nano-layers, such effect on electrical resistivity is overcome by a 70% enhancement of the power factor, even though slower carriers motion and lower carriers concentration are reported due to the defects presence [51]. In dislocation engineered Bi_2Te_3 , dislocations presence at grain boundaries plays in favor of a higher Seebeck coefficient [52].

1.3.1.3 Thermal conductivity

The evaluation of the thermal conductivity in the presence of defects requires to identify the phonon scattering terms of each of these defects (dislocation, grain boundary, vacancy...) and implement them in a calculation model. The interaction of a dislocation with the thermal resistivity is due to the phonon scattering through two mechanisms analytically developed in the P.G. Klemens works on second-order perturbation theory for phonon scattering rates [53], [54]. The first scattering mechanism is a long-range effect due to the elastic strain field induced by the lattice. The dislocation long-range phonon scattering rates by the elastic strain field of the screw τ_S and edge τ_E dislocations are expressed as

$$\frac{1}{\tau_s} = \frac{2^{\frac{3}{2}}}{3^{\frac{3}{2}}} N_D^S b_S^2 \gamma^2 \omega, \quad (1.23)$$

and

$$\frac{1}{\tau_E} = \frac{2^{\frac{3}{2}}}{3^{\frac{3}{2}}} N_D^S b_E^2 \gamma^2 \omega \left[\frac{1}{2} + \frac{1}{24} \left(\frac{1-2\nu}{1-\nu} \right)^2 \left(1 + \sqrt{2} \left(\frac{v_L}{v_T} \right)^2 \right)^2 \right]. \quad (1.24)$$

Where v_L and v_T stand respectively for the longitudinal and the transverse component of sound velocity, ν is the Poisson's ration, b_S and b_E are the magnitudes of the Burgers vectors of screw and edge dislocations respectively, γ is the Grünsen parameter, and ω the phonon frequency. In the case of a mixed dislocation, the magnitude b_M is the sum of the magnitudes of the screw and edge dislocation, leading to

$$\frac{1}{\tau_M} = \frac{2^{\frac{3}{2}}}{3^{\frac{3}{2}}} N_D^S b_S^2 \gamma^2 \omega \left\{ b_S^2 + b_E^2 \left[\frac{1}{2} + \frac{1}{24} \left(\frac{1-2\nu}{1-\nu} \right)^2 \left(1 + \sqrt{2} \left(\frac{v_L}{v_T} \right)^2 \right)^2 \right] \right\}. \quad (1.25)$$

These expressions can be modulated by a parameter, labelled η , for which the value is based on the dislocation orientation, the temperature gradient and the phonon wave vector. The adjustment factor η works as follows : for a dislocation line perpendicular to the temperature gradient, $\eta=1$, and $\eta=0.55$ for a random orientation [54].

The second mechanism is the action of the dislocation core, a short range influence considered here to be equivalent to the deficit of two mass points per atomic plane along

the dislocation line, in accordance with the density change due to dislocations [55]. The phonon scattering rate due to a dislocation core is expressed as

$$\frac{1}{\tau_{DC}} = N_D \frac{V_0^{\frac{4}{3}}}{v^2} \omega^3. \quad (1.26)$$

Where N_D is the dislocation density, including both screw and edge, the term v represents the particle velocity. Comparing the core effect Eq.1.26 with the strain field effect Eq.1.25, the latter varies as the cubic of the frequency (ω^3) and the first linearly (ω). This difference in sensitivity vanishes for high frequencies, where the two effects become comparable at the Debye frequency. All these relationships are describing sessile dislocations; the consideration of glissile dislocation lines implies more scattering due to re-radiation, described for all frequencies in Granato and Lücke works [56].

It is possible to calculate the thermal conductivity with a model developed by J. Callaway [57] using these scattering terms in τ_c with

$$\kappa = \left(\frac{T k_B}{\hbar}\right)^3 \frac{k_B}{2 \Pi^2 v} \int_0^{\theta_D/T} \frac{\tau_c (x^4 e^x)}{(e^x - 1)^2} dx, \quad (1.27)$$

where k_B is the Boltzmann's constant, \hbar is the Planck constant, T is the absolute temperature, v is an average sound velocity, ω is the phonon frequency and $x = \hbar\omega/k_B T$. The term τ_c is the combined relaxation time, which following the Matthiesen rule is expressed as $\tau_c^{-1} = \sum_i \tau_i^{-1}$, where τ_i are the individual scattering terms considered for the model. In addition to the dislocation scattering terms, other scattering terms from microstructural features can be considered, developed as well by Klemens [53] such as the

boundary scattering term (τ_B^{-1}), independent from the phonon frequency ω and the point defect scattering term (τ_{PD}^{-1}) which is ω^4 dependent. Also working the reverse way, these models were used to estimate the dislocation density from the thermal conductivity in simple medium such as single crystals [58], [59]. Modelling the thermal conductivity with this model is a common task. One of the latest examples is in a dislocation-engineered Bi_2Te_3 : it served as a base for developing a deeper understanding of the scattering terms [52], [60], assessing how the dislocation scattering terms are weighting in the Matthiessen's equations, supported by experimental data.

Only few materials have been subjected to studies aiming at understanding the relationship between dislocations activity and thermal conductivity. Among the first reported is a study on LiF, supported by both experimental [61], [62] and analytical studies [59]. One of the critical outcomes of these studies is the demonstration that thermal conductivity decreases as the deformation of LiF specimen increases as shown in Fig. 1.13 [62]. These observations are then correlated to the dislocation density observed on etched surfaces at various stage of deformation, showing a T^3 to $T^{3.5}$ sensitivity, as predicted by Eq.1.27 with a T^3 sensitivity.

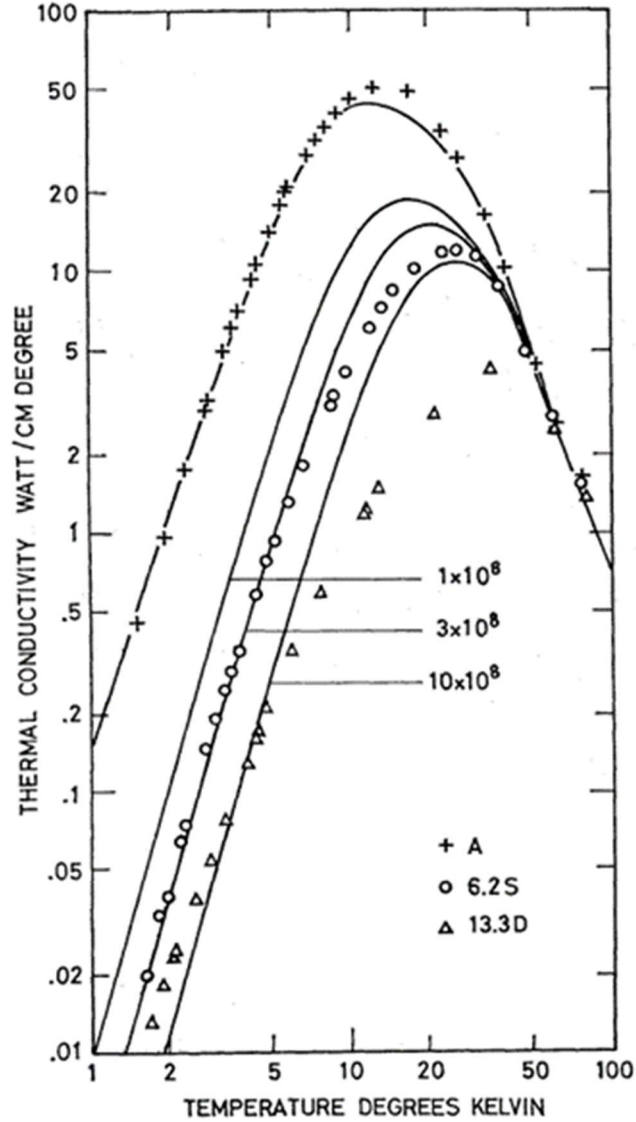


Figure 1.13: thermal conductivity vs temperature in LiF for various density of etch pits in slip bands in cm^{-2} for various amounts of deformation. The solid lines are theoretical work from Srpoull and the identified lines are experimental work from Suzuki.

Additional studies show similar behavior in GaN thin film, where the dislocation density evolves with the film thickness. It demonstrates with correlated experiments and calculations that a dislocation density increase can cause a sudden drop in thermal conductivity [63], [64]. The results are reported as dislocation density vs. thermal conductivity at 300K, where the thermal conductivity is constant until the dislocation

density reaches $5 \times 10^6 \text{ cm}^{-2}$, causing the linear constant decrease with higher dislocation density as reported in Fig. 1.14 [64].

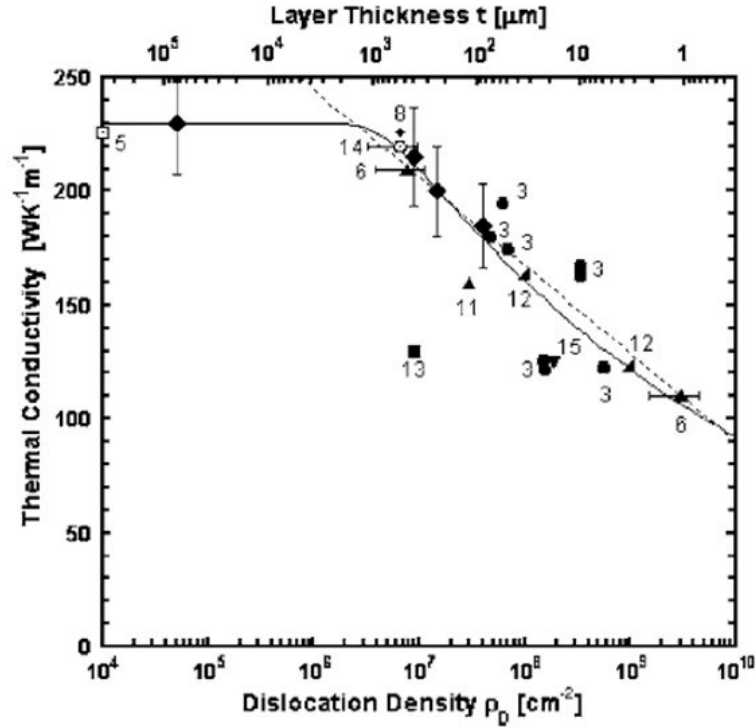


Figure 1.14: Thermal conductivity vs dislocation density in GaN showing a plateau until constant slope decrease

1.3.2 Dislocations studies in thermoelectric materials

Dislocation studies in TE material are rare, as most of the authors have limited the dislocations-related content to dislocation density and qualitative observations such as the location of the dislocations in GB surroundings. The study of dislocations in TE materials can be sorted either as focusing on as-processed materials or on deformed materials as in the cases of LiF (deformed) and GaN (as-processed) previously described.

1.3.2.1 Post-processing dislocations

The dislocations in TE materials have been thoroughly studied in Bi_2Te_3 materials which has an hexagonal lattice. A study shows a dislocation density of 10^9 cm^{-2} in this material, where dislocations possess a long-range strain field [65]. The dislocations are described as sensitive to heat, easily moving when subject to the heat induced by the electron beam during TEM observations. This study demonstrates an easy glissile dislocation motion within the basal plane while being under the focused electron beam in the TEM, by successive hopping from the pinning sites, through kink formations. In the bulk, straight dislocations are observed, as well as loops and half-loops about 10nm in size. In addition, a higher dislocation density is reported at the low-angle grain boundaries (Fig. 1.15), due to pile-up.

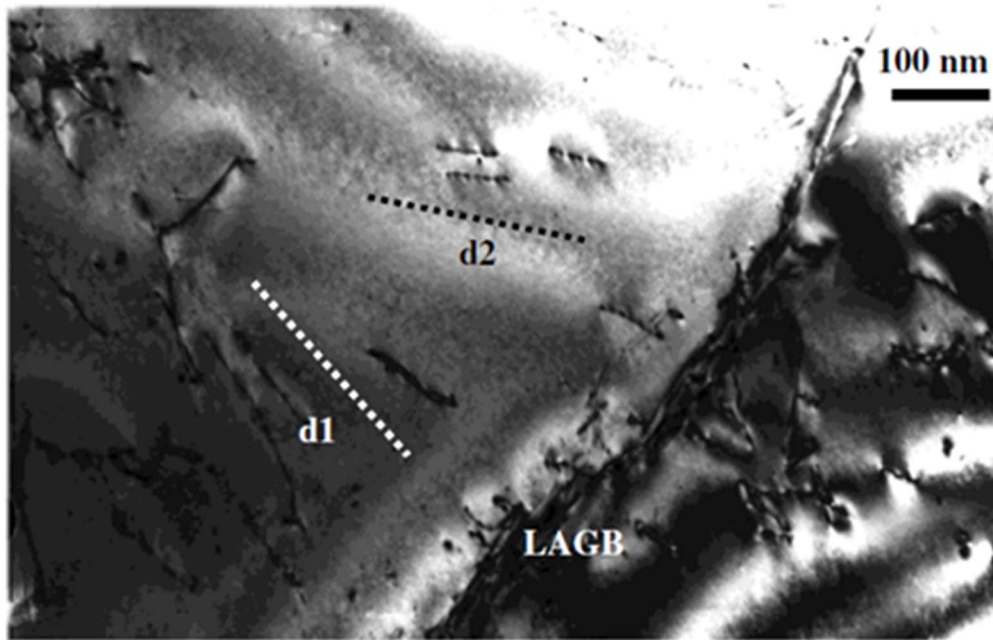


Figure 1.15: TEM bright-field images of dislocations in n-type bismuth telluride under two-beam conditions with presence of dipoles (d1, d2) and small loops and a low angle grain boundary (LAGB).

A complementary study provides a more comprehensive dislocation description [66]. Mixed dislocations are reported with a Burgers vector parallel to $[110]$, line direction $[2\bar{7}\bar{1}1]$, on the basal plane as glide plane. Reported glide velocities of $10 \text{ nm}\cdot\text{s}^{-1}$ to $100 \text{ nm}\cdot\text{s}^{-1}$, and are activated by a shear stress of 10 MPa (Fig. 1.16).

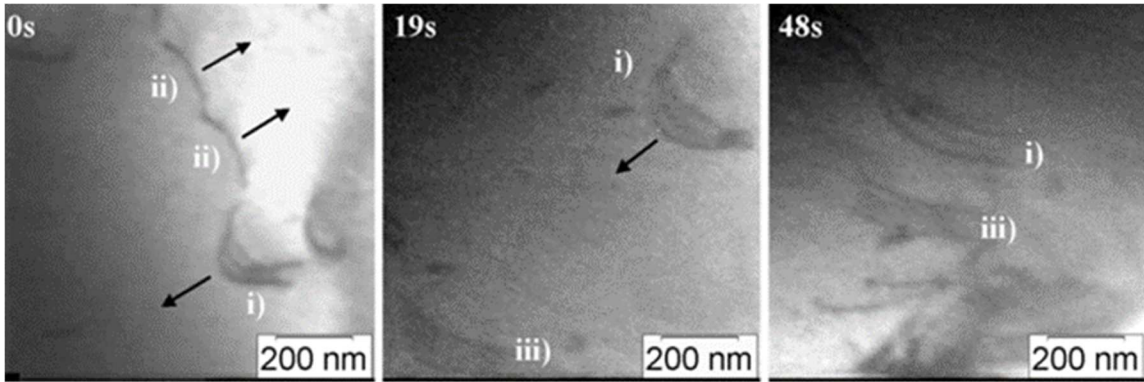


Figure 1.16: Video sequences acquired by TEM in Bi_2Te_3 material of free standing dislocations (i) and (ii) at different times, gliding in opposite directions indicated by arrows. The motion of dislocations (i) stopped in front of a dislocation pileup (iii)

The study is completed by scattering measurements of phonon on dislocations. The dislocations are proved to scatter the phonon with their associated strain field, with an estimated phonon mean free path of $800 \mu\text{m}$ at 3 K. It is known that the dislocation contribution to the variation of phonon density of states is more significant at lower temperatures [67], but other studies show similar results at higher temperatures in same material [68].

In addition, ultrasound attenuation is determined in relation with the dislocation density of the Bi_2Te_3 single crystal, in good standing with the dislocation resonance theory of Granato and Lücke [56]. This theory predicts an interaction between phonons and dislocations acting as oscillating strings, absorbing the phonons and thus decreasing the thermal conductivity.

Such in depth approach, combining dislocation study and associated phonon scattering properties has only been provided for Bi_2Te_3 , which can be explained by its longtime use in electronic and cooling devices since the 1960's and commercial, thus relying on a comprehensive literature. The Bi_2Te_3 alloys are among the first choice for advanced engineering in the TE field. The first application of the nanostructure in bulk TE material [23], and the first TE material with an engineered periodical dislocation array at grain boundary [61] were carried out on Bi_2Te_3 . These techniques are used toward enhanced phonon scattering, to decrease the thermal conductivity.

In addition to Bi_2Te_3 few additional studies are assessing dislocations in as-processed TE material. In p-type PbTe-SrTe , the microstructure surrounding endotaxially placed nanoscale precipitates is analyzed to assess the dislocation content [69]. A recent study on InSb , assessing the role of defects on the transport properties, shows thermal transport sensitivity due to the presence of dislocations and stacking faults at grain boundaries [70], but with no further observations.

1.3.2.2 Deformation-induced dislocations

In addition to the previous example on LiF , deformation induced dislocation study was performed in Skutterudite. Caused by the severe plastic deformation process “high pressure torsion” (HPT), the dislocation density variation was assessed but with no further extent to dislocation properties or deformation mechanisms and dislocation observation [44], [45]. By comparing HPT processed with ball milled $\text{Ba}_{0.06}\text{Co}_4\text{Sb}_{12}$ [44], the study shows HPT processing decreases the grain size from 109 nm to 47 nm and increases the dislocation density from 10^{12} - 10^{13} m^{-2} to $7 \times 10^{14} \text{ m}^{-2}$. As the focus of TE material study is the refined grain size for phonon scattering properties, dislocation content is of secondary order.

Overall, as the dislocations can be considered as a mean to tune TE properties, the study of these defects, primordial in both processed and deformed TE materials is lacking data.

1.3.2.3 Dislocation engineering

Dislocations, which are among common research subjects in the semi-conductors field, are now in the spotlight in the TE field as a viable mechanisms for microstructural engineering toward higher ZT. As mentioned in previous sections, analytical studies on phonon scattering due to lattice defects have been thoroughly conducted by a few authors such as P.G. Klemens and Calaway. Relying on this work, the first study involving engineered dislocations enhancing the ZT was published in 2015 [52]. This study describes a method for dislocation engineering at grain boundaries in a $\text{Bi}_{0.5}\text{Se}_{1.5}\text{Te}_3$ alloy. The initial powder composition contains an excess of Te which forms a eutectic phase during sintering as described in Fig.1.17a where the melt-spun stoichiometric $\text{Bi}_{0.5}\text{Sb}_{1.5}\text{Te}_3$ (S-MS) is indicated with the blue arrow and the 25 wt. % Te excess $\text{Bi}_{0.5}\text{Sb}_{1.5}\text{Te}_3$ (Te-MS) is indicated with the red arrow. While the sintered alloys cools down, the Te excess, which has the lowest melting point, forms a liquid phase at the GBs. Assisted by a high pressure compacting, the liquid Te excess expelled, creating stress fields and promoting dislocation nucleation at GBs, allowing the grains to arrange with a low-angle misorientation. The resulting effect is a material with low angle boundary and periodic arrays of dislocations at GBs. As an engineered microstructure, such process supports an enhanced phonon scattering at GBs, resulting in an additional 29% reduction in κ_{lattice} due dislocation core and strain field scattering [60].

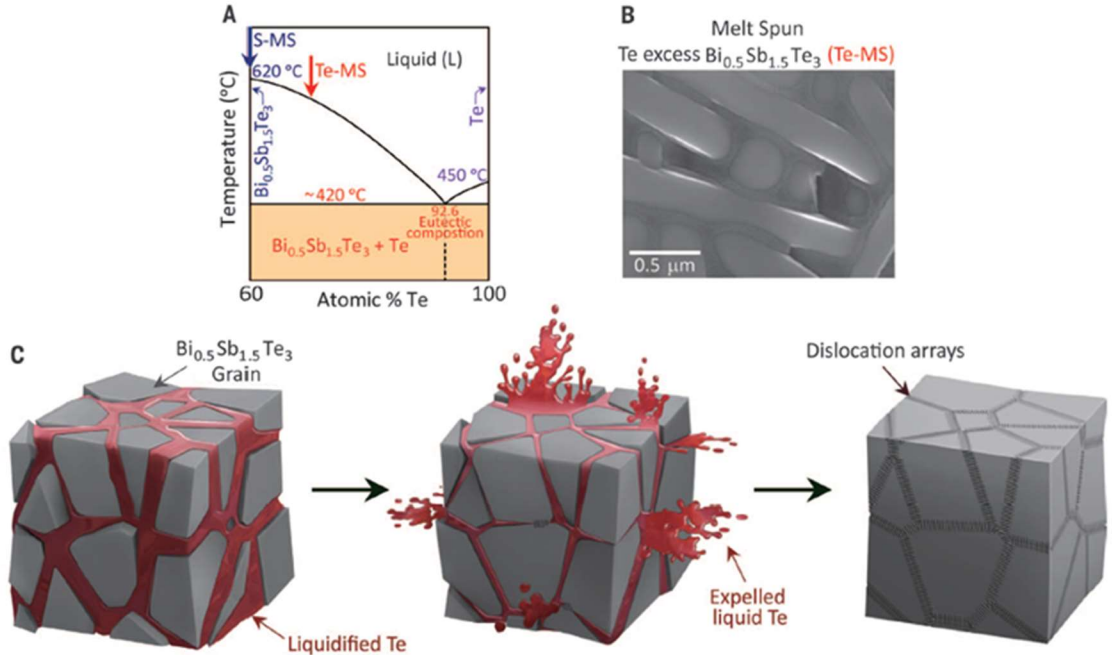


Figure 1.17: **a**-phase diagram of Bi_{0.5}Sb_{1.5}Te₃-Te.. **b**- SEM image of melt-spun ribbon of Te-MS material showing the Bi_{0.5}Sb_{1.5}Te₃ platelets surrounded by the eutectic phase of Bi_{0.5}Sb_{1.5}Te₃-Te mixture. **c**- Illustration of the dislocation arrays generation during the liquid-phase compaction process.

These results offer additional proof that scattering due to material defects may provide an alternate path to higher ZT, and also improves the understanding of the associated scattering mechanisms. To model the grain boundary scattering in these samples, the addition of the scattering terms τ_{DC}^{-1} and τ_{DS}^{-1} were necessary since the terms Umklapp (τ_U^{-1}), point defect (τ_{PD}^{-1}) and boundary (τ_B^{-1}) scattering terms were not sufficient any more. These results reported in Fig.1.18 [52] are supporting new models where dislocation scattering is replacing the usual GB scattering and are considered as a part of the GB [60].

This study has shifted the notions about dislocations from a metallurgical parameter to a tuning tool for higher ZT in the TE community, as they are now proven to effectively

reduce the medium frequencies of the phonon spectrum whereas nanostructure and point defects act on the extremums.

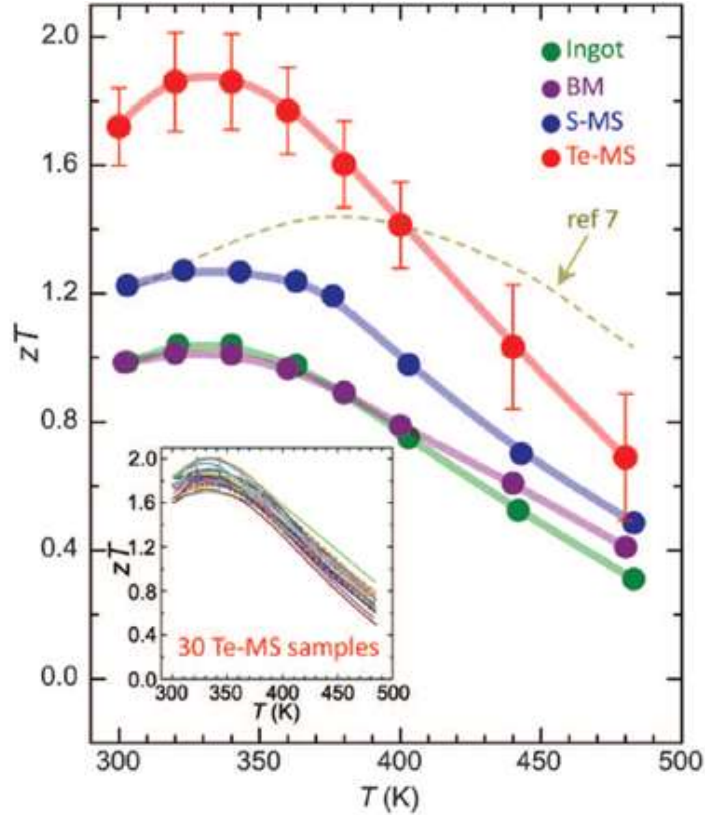


Figure 1.18: ZT vs temperature for each step of sample processing : the green plot is the ingot, the violet the ball milled (BM), the blue plot the melt-spun with stoichiometric proportion (S-MS) and the red plot the melt-spun with an excess of Te (TE-MS).

New dislocation-engineered TE alloys with enhanced ZT were since developed such as PbTe with lattice dislocations [71], vacancy-induced dislocations in PbSe [72] which by detailing the isolated effect of dislocations with modeling and experimental work, provide complementary understanding to the dislocation effect on κ_{lattice} .

While dislocation interaction with thermal conductivity possess a strong basis, the methods to grant TE materials higher ZT via defect engineering just started. Nevertheless, dislocation studies are still very rare for TE materials. To build a TE devices and produce

TE alloys that can match the service conditions, such study must be conducted, by determining the yield point and analyze the plastic behavior of a deformed material.

1.3.3 The case of metallic TE alloys

One of the limitations of the ZT lies into the inter-dependence between electron and phonons properties [73]. A straight forward example can be given by comparing ceramics to metals. While ceramics will provide high electrical and thermal resistivity, it will be the opposite with metals. Therefore, semi-conductors are developed to tune these properties to reach a compromise in bulk materials, as demonstrated in previous sections. However, tuning materials indefinitely eventually reach a limit, which will be the amorphous limit in bulk materials.

For this reason, new ways to enhance thermal energy conversion are under development such as the spin-Seebeck effect [74], occurring in thin metal films deposited on ferromagnetic substrates. The thermal gradient in the ferromagnet translates into a magnetization gradient. As free electrons are sensitive to localized magnetization, a heat flux driving the magnetization dynamics in the ferromagnet can generate electrical energy in the adjacent metal. This effect was proven more efficient at scattering phonon than classical TE process at cryogenic temperature in thin InSb film [75]. Initially isolated to thin films, the spin-Seebeck effect was then extended to bulk nanocomposites [76] which are suitable for large scale energy-conversion application as opposed to thin films. At bulk scale, the additional contribution of magnon-electron drag is considered. Proven to dominate the thermopower of Fe, Co and Ni[77], this magnetic mechanism acts on the electronic part of the thermal conductivity, providing an additional opportunity to optimize

metallic thermoelectric alloys. On this basis, thermoelectric generators made of metals with high power factor can be build [78].

These metal-based TEG would benefit from the ductile nature of metals, that can be shaped as needed through processing routes and deformation, in opposition to brittle semi-conductors. Hence, new design for TEG could be developed. These could be shaped to perfectly fit a hollow space, or even be directly welded to thermal exchanger. As material ductility can be associated with dislocation activity, the deformation mechanisms study provides a necessary basis to the material reliability.

1.4 Half-Heusler thermoelectric alloys

The p-type half-Heusler $\text{Hf}_{0.44}\text{Zr}_{0.44}\text{Ti}_{0.12}\text{CoSb}_{0.8}\text{Sn}_{0.2}$ was chosen here to carry on the deformation mechanisms study. Especially developed to answer issues related to cost, toxicity and effectiveness, it was processed with advanced compositions and microstructure for a TE material.

1.4.1 Development of the p-type half-Heusler MCoSb

The half-Heusler structure is of MgAgAs type, composed of three interpenetrating face-centered-cubic sublattices and one vacant sublattice [79]. Most of the research effort was based on MAB (M for metal) systems, such as MCoSb and MNiSn where M- can be Ti, Zr, or Hf, taking advantage of the high substitutability of the three lattice sites for thermoelectric tuning. Elemental substitution of the A- and B- sites can be done to reduce the lattice thermal conductivity while the carrier concentration, hence the electrical conductivity, can be tuned by M- site elemental substitution [80]. The half-Heusler alloys are considered as medium- to high-temperature thermoelectric and have a promising

position among TE materials for power generation. The half-Heusler TE alloys were improved through several steps.

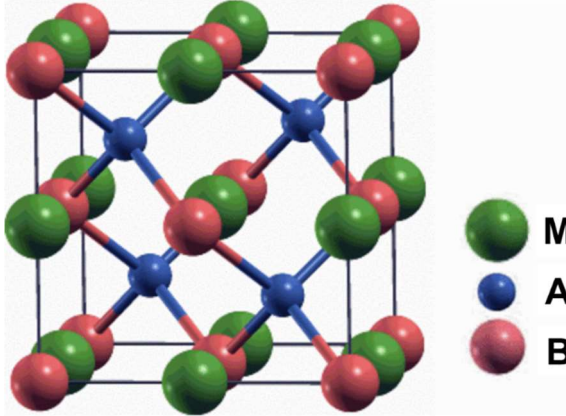


Figure 1.19: Crystal structure of the half-Heusler

The first step toward higher ZT was to change the microstructure to a nanocomposite resulting in an increased ZT in both p-type and n-type. This way, the ZT was raised from 0.5 to 0.8 for the p-type $\text{Hf}_{0.5}\text{Zr}_{0.5}\text{CoSb}_{0.8}\text{Sn}_{0.2}$ [81] and from 0.8 to 1 with the n-type with the $\text{Hf}_{0.75}\text{Zr}_{0.25}\text{NiSn}_{0.99}\text{Sb}_{0.01}$ [82]. The enhanced ZT is due to the decreased grain size and the presence of nanoprecipitates, with an average grain size about 100nm to 300nm which enhance phonon scattering and so lowers the thermal conductivity of respectively 23% for the p-type and 29% for the n-type. The second step was to increase the change in atomic mass for M in the half-Heusler phase, based on early work assessing the link between variation in Ti, Zr and Hf amount on thermal conductivity in n-type (Ti, Zr, Hf)NiSn [83]. Investigations on binary composition for M raised the ZT to 1 at 800°C for the $\text{Hf}_{0.8}\text{Ti}_{0.2}\text{CoSb}_{0.8}\text{Sn}_{0.2}$, a 25% enhancement over the $\text{Hf}_{0.5}\text{Zr}_{0.5}\text{CoSb}_{0.8}\text{Sn}_{0.2}$ composition [84].

In fine, the M sites can be either a single atom (Ti, Zr or Hf), a combination of two atoms (Hf-Zr, Hf-Ti, Zr-Ti) [84], or a combination of the three [85]. The choice of the single, binary or ternary phase resides in the thermoelectric properties it grants the processed material, where the more complex the phase, the more refined the tuning of the properties can be. The latest trend in half-Heusler improvement is the ternary composition by combining various ratio of Ti/Zr/Hf. The compositions and the associated ZT are reported in Fig 1.20 [80]. These compositions can mediate cost-related issues with the expensive Hf as well as high thermoelectric properties with for instance the p-type $\text{Hf}_{0.44}\text{Zr}_{0.44}\text{Ti}_{0.12}\text{CoSb}_{0.8}\text{Sn}_{0.2}$, built to contain less Hf and match the thermoelectric performance of the $\text{Hf}_{0.5}\text{Zr}_{0.5}\text{CoSb}_{0.8}\text{Sn}_{0.2}$.

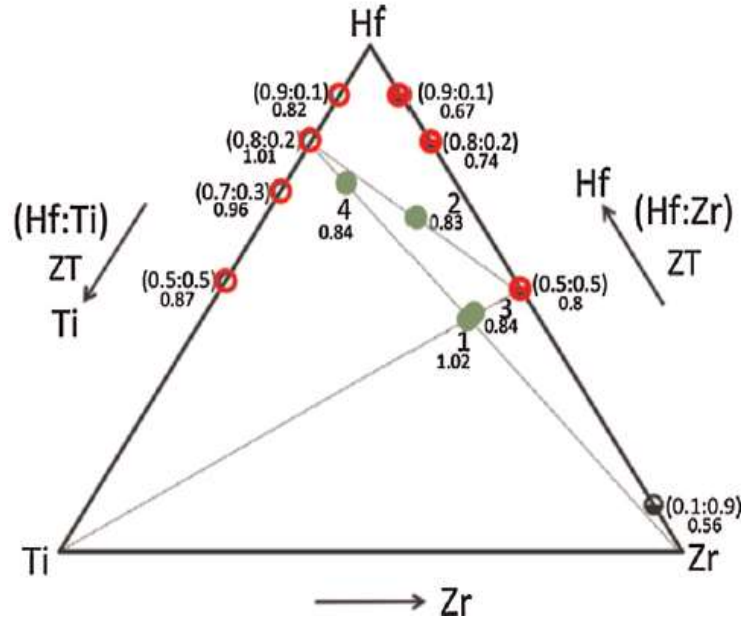


Figure 1.20: $(\text{Ti, Zr, Hf})\text{CoSb}_{0.8}\text{Sn}_{0.2}$ ternary phase diagram. The ternary compositions are: $\text{Hf}_{0.44}\text{Zr}_{0.44}\text{Ti}_{0.12}\text{CoSb}_{0.8}\text{Sn}_{0.2}$ (1); $\text{Hf}_{0.65}\text{Zr}_{0.25}\text{Ti}_{0.1}\text{CoSb}_{0.8}\text{Sn}_{0.2}$ (2); $\text{Hf}_{0.45}\text{Zr}_{0.45}\text{Ti}_{0.1}\text{CoSb}_{0.8}\text{Sn}_{0.2}$ (3); and $\text{Hf}_{0.72}\text{Zr}_{0.1}\text{Ti}_{0.18}\text{CoSb}_{0.8}\text{Sn}_{0.2}$ (4).

1.4.2 Properties of the p-type $\text{Hf}_{0.44}\text{Zr}_{0.44}\text{Ti}_{0.12}\text{CoSb}_{0.8}\text{Sn}_{0.2}$

1.4.2.1 Synthesis

The p-type half-Heusler $\text{Hf}_{0.44}\text{Zr}_{0.44}\text{Ti}_{0.12}\text{CoSb}_{0.8}\text{Sn}_{0.2}$ is processed in the TcSUH facilities at the University of Houston by Dr. Zhifeng Ren's group. This nanostructured material is processed as follows [85], [86]. Ingots arc melted at 1200 °C under Ar atmosphere are flipped and re-melted twice to ensure homogeneity. These ingots are then milled by stainless steel balls (12.7 mm diameter) for 5 hours to reduce to them to powder size of 10nm. This nanopowder is sintered in a fast-direct current assisted hot press at 1125°C with a temperature rising rate of 100°C per minute. The powder is pressed at 80 MPa, and the peak temperature is maintained during 2min, forming the final pellets. This specific composition is derived from the prior compositions, containing higher amount of Hf ($\text{Hf}_{0.5}\text{Zr}_{0.5}\text{CoSb}_{0.8}\text{Sn}_{0.2}$, $\text{Hf}_{0.8}\text{Ti}_{0.2}\text{CoSb}_{0.8}\text{Sn}_{0.2}$). The Hf expense is a major issue in these alloys, so optimization via binary or ternary composition in the p-type MCoSb proceeds to meet thermoelectric requirements with more freedom in the M composition. The p-type half-Heusler $\text{Hf}_{0.44}\text{Zr}_{0.44}\text{Ti}_{0.12}\text{CoSb}_{0.8}\text{Sn}_{0.2}$ is reported with a relative density of 99.4% and a an average grain size of 200nm (Fig.1.21) [85].

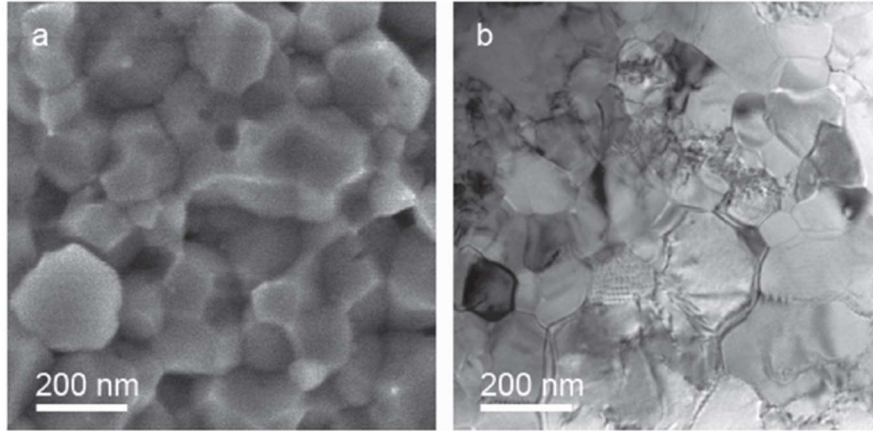


Figure 1.21: Reported microstructure of $\text{Hf}_{0.44}\text{Zr}_{0.44}\text{Ti}_{0.12}\text{CoSb}_{0.8}\text{Sn}_{0.2}$ with **a-** Scanning electron microscopy observation of a fractured surface **b-**Microstructure observed by transmission electron microscopy

1.4.2.2 Thermoelectric properties

Among the binary compositions, $\text{Hf}_{0.5}\text{Zr}_{0.5}\text{CoSb}_{0.8}\text{Sn}_{0.2}$ [81] has a maximum ZT of 0.8, and $\text{Hf}_{0.8}\text{Ti}_{0.2}\text{CoSb}_{0.8}\text{Sn}_{0.2}$ [85] a maximum ZT of 1. On this basis, ternary composition (Hf, Zr and Ti) was tested in various amount, reaching the best composition possible, while trying to reduce the amount of Hf. With a ZT of 0.97 at 700°C and superior to 1 at 800°C, the composition $\text{Hf}_{0.44}\text{Zr}_{0.44}\text{Ti}_{0.12}\text{CoSb}_{0.8}\text{Sn}_{0.2}$ shows highest ZT. Comparisons of these three kinds of p-type half-Heusler are reported in Fig. 1.22 [85], showing higher TE properties for the $\text{Hf}_{0.44}\text{Zr}_{0.44}\text{Ti}_{0.12}\text{CoSb}_{0.8}\text{Sn}_{0.2}$. This composition has a consistent ZT around 1 for medium temperature, as the n-type at similar temperatures, suggesting a combination of the two would be ideal for a TEG design.

Nevertheless, the mechanical robustness should also be similar, but mechanical properties are uncommon in the TE field, and the deformation mechanisms are yet to be known, since they are crucial for industrial design.

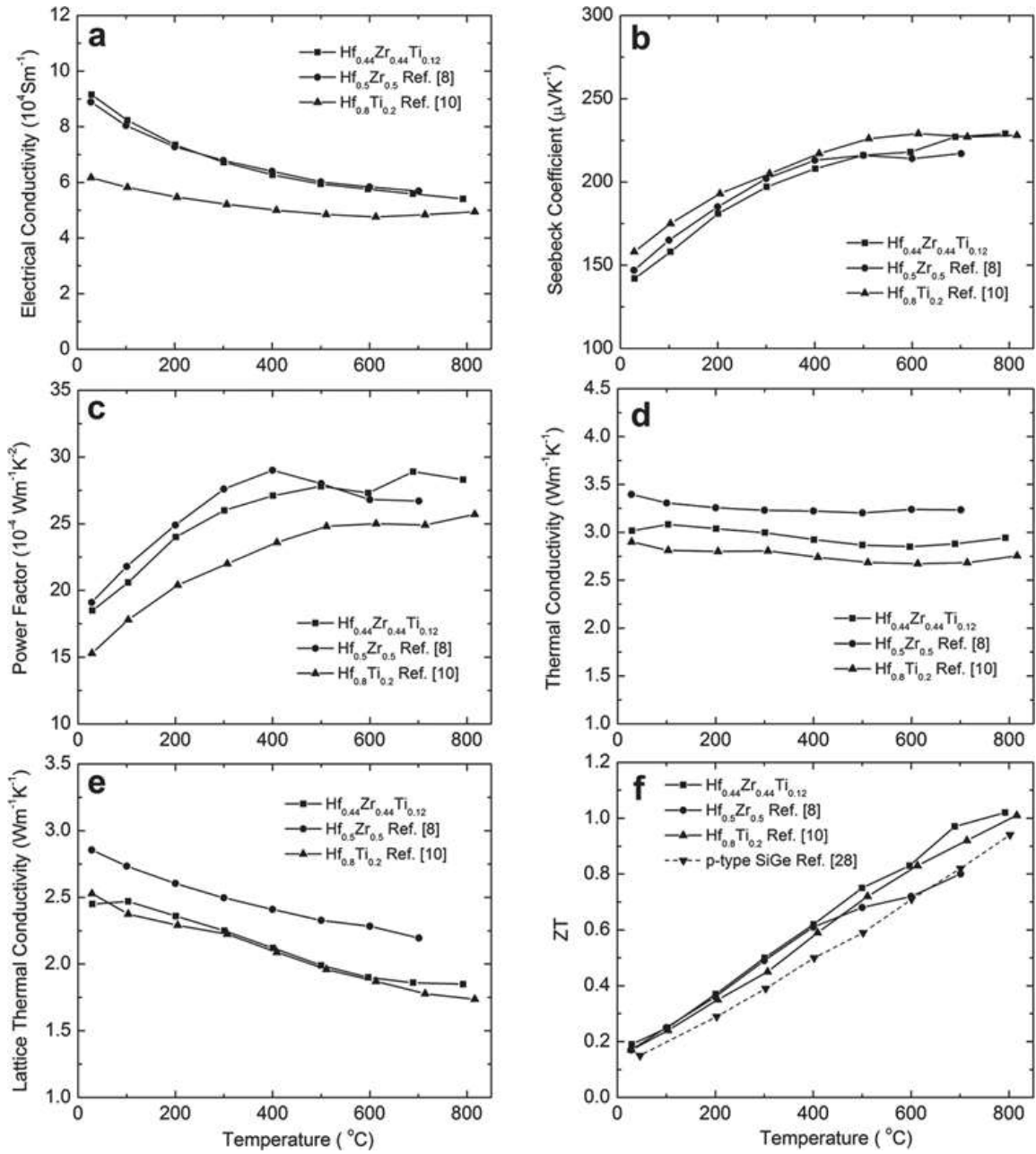


Figure 1.22: **a**-electrical conductivity, **b**-Seebeck coefficient, **c**-power factor, **d**-thermal conductivity, **e**-lattice thermal conductivity, and **f**-ZT of $\text{Hf}_{0.44}\text{Zr}_{0.44}\text{Ti}_{0.12}\text{CoSb}_{0.8}\text{Sn}_{0.2}$, $\text{Hf}_{0.5}\text{Zr}_{0.5}\text{CoSb}_{0.8}\text{Sn}_{0.2}$, and $\text{Hf}_{0.8}\text{Ti}_{0.2}\text{CoSb}_{0.8}\text{Sn}_{0.2}$. The p-type SiGe has been added in (f) for comparison

1.4.2.3 Mechanical properties and dislocations

Mechanical properties are reported in the literature on the $\text{Hf}_{0.44}\text{Zr}_{0.44}\text{Ti}_{0.12}\text{CoSb}_{0.8}\text{Sn}_{0.2}$. Nanoindentation study [36] provided much information regarding this alloy, with the determination of the elastic constants (Table1, [36]).

Table 1 : elastic constants determined by nanoindentation

	Berkovich indenter (95% Confidence interval)	Conical indenter (95% Confidence interval)
S_{11} ($\times 10^{-3}$ GPa $^{-1}$)	3.92 (1.31, 6.46)	4.12 (3.16, 5.16)
S_{12} ($\times 10^{-3}$ GPa $^{-1}$)	-0.69	-0.91
S_{44} ($\times 10^{-3}$ GPa $^{-1}$)	11.66	12.09
C_{11} (GPa)	275	277
C_{12} (GPa)	58	79
C_{44} (GPa)	86	83

Elastic properties were determined as well, giving all necessary information to carry on simulations of this material (Table 2, [36]).

Table 2: elastic properties determined by nanoindentation and ultrasonic measurements

	Berkovich indenter	Conical indenter	Ultrasonic method	$\text{Al}_2\text{O}_3 + 0.3\% \text{MgO}^{21}$
Poisson ratio (ν)	0.175	0.221	0.252	0.24
Average Young's modulus (Voigt's approx) (GPa)	229	222	—	—
Average Young's modulus (Reuss's approx) (GPa)	227	221	—	—
Reported isotropic Young's modulus (GPa) (Ran <i>et al.</i> , 2014)	225	—	198	358.0
Axial compressibility (GPa $^{-1}$)	2.55×10^{-3}	2.30×10^{-3}	—	—
Volume compressibility (GPa $^{-1}$)	7.65×10^{-3}	6.90×10^{-3}	—	—
Bulk modulus (B) (GPa)	116	145	—	234.5
Zener (anisotropy) ratio	0.79	0.83	—	—

Finally, the crystal elastic anisotropy was assessed via nanoindentation work in grains large enough to accommodate the testing dimensions (Table 3, [36]). The study provided the directional young modulus, showing a rather limited anisotropy, which is understandable regarding the FCC structure of the alloy, and values for Young's modulus ranging from 208 GPa to 255 GPa.

Table 3:directional young modulus

Berkovich Indenter (GPa)			Conical Indenter (GPa)		
$E_{\langle 100 \rangle}$	$E_{\langle 110 \rangle}$	$E_{\langle 111 \rangle}$	$E_{\langle 100 \rangle}$	$E_{\langle 110 \rangle}$	$E_{\langle 111 \rangle}$
255	220	211	242	216	208

The p-type half-Heusler $\text{Hf}_{0.44}\text{Zr}_{0.44}\text{Ti}_{0.12}\text{CoSb}_{0.8}\text{Sn}_{0.2}$ has relatively high elastic modulus (~ 221 GPa) and hardness (12.8 GPa) (Table 4, [37]) when compared to other TE materials as reported in Fig 1.11, which suggests brittleness as it stands within the ceramic mechanical properties. The fracture toughness of this alloys was estimated to average around $1.7\text{-}2.2 \text{ MPa}\cdot\text{m}^{1/2}$ with single edge notch band experiments (SENB) [40], [87].

Table 4: hardness and modulus by nanoindentation study for various TE materials

specimen composition	nanoindentation		after AFM corrections	
	hardness (GPa)	modulus (GPa)	hardness (GPa)	modulus (GPa)
p-type half-Heusler	13.9 ± 0.3	231.0 ± 6.2	12.8	221.0
n-type half-Heusler ^a	9.9 ± 1.2	213.9 ± 17.6	9.1	186.5
p-type $\text{Bi}_{0.4}\text{Sb}_{1.6}\text{Te}_3$ ^a	1.5 ± 0.1	48.7 ± 4.4	1.1	41.5
n-type $\text{Bi}_2\text{Te}_{2.7}\text{Se}_{0.3}$ ^a	1.4 ± 0.1	42.8 ± 5.6	1.2	38.8
p-type SKU ^a	6.8 ± 0.4	144.0 ± 11.0	5.6	129.7
n-type SKU ^a	7.1 ± 2.2	152.2 ± 21.9	5.8	136.9
n-type $\text{Si}_{0.8}\text{Ge}_{0.2}\text{P}_2$	11.9 ± 0.7	175.2 ± 7.1	10.8	166.3
p-type $\text{Si}_{0.8}\text{Ge}_{0.2}\text{B}_5$	11.8 ± 0.9	163.9 ± 4.6	10.7	155.6
p-type $\text{In}_{0.005}\text{PbSe}$	0.7 ± 0.1	74.1 ± 5.9	0.6	65.9

DFT calculations were performed by *ab initio* simulations on the deformation mechanisms of (Ti, Zr, and Hf)NiSn half-Heusler compounds [88]. This study shows the lowest theoretical shear stress is associated to the $\langle \bar{1}10 \rangle \{111\}$ slip system at a stress level of 10.52 GPa in the TiNiSn system, as reported in Fig. 1.23a. The influence of the elements for a (Ti, Hf, Zr)NiSn system on the shear stress required to trigger slip activity is very limited, as reported in Fig. 23b.

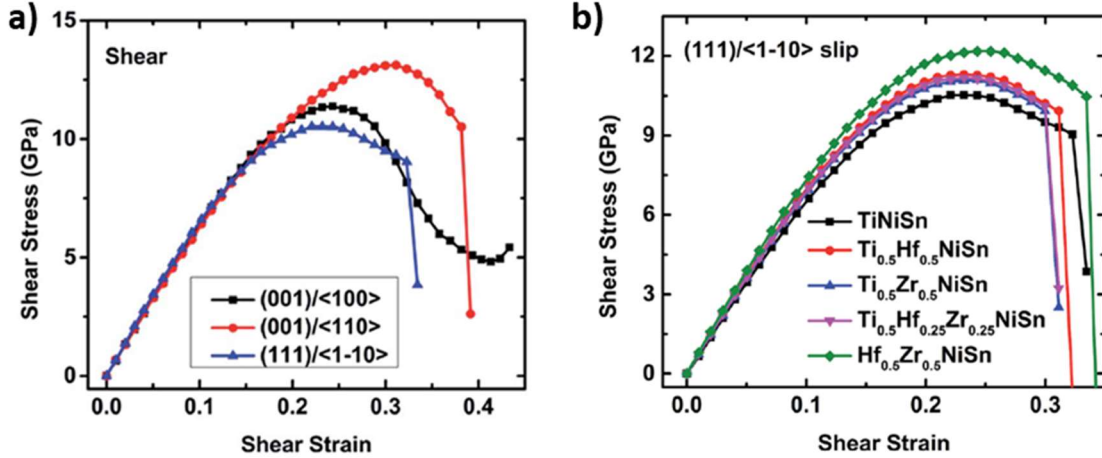


Figure 1.23: **a**-calculated stress vs. strain of TiNiSn under various slip systems **b**- calculated stress vs. strain of (Ti, Zr, and Hf)NiSn under $\langle 110 \rangle \{111\}$ shear loading

Although not identical to the $\text{Hf}_{0.44}\text{Zr}_{0.44}\text{Ti}_{0.12}\text{CoSb}_{0.8}\text{Sn}_{0.2}$ alloy, the TiNiSn example can be used for comparison. With a minimal shear stress level of 10.52 GPa required to activate a slip system, this study shows very high stresses are required to do so. In comparison, the elastic constants for the TiNiSn are presented in Table 5 [88], for which equivalent data are reported in Table 1 for $\text{Hf}_{0.44}\text{Zr}_{0.44}\text{Ti}_{0.12}\text{CoSb}_{0.8}\text{Sn}_{0.2}$. The two dataset shows the values of the elastic constant of TiNiSn are lower compared to the one of $\text{Hf}_{0.44}\text{Zr}_{0.44}\text{Ti}_{0.12}\text{CoSb}_{0.8}\text{Sn}_{0.2}$ except for C_{12} , so the 10.52 GPa shear stress is a good approximate to the value necessary to trigger plasticity in $\text{Hf}_{0.44}\text{Zr}_{0.44}\text{Ti}_{0.12}\text{CoSb}_{0.8}\text{Sn}_{0.2}$.

Table 5: calculated elastic constants (C_{11} , C_{12} , C_{44}) and related elastic properties: bulk modulus (B), shear modulus (G), Young's modulus (E), Poisson's ration (ν), and ductility index (B/G) of TiNiSn, in comparison with the available theoretical results

Method	C_{11} (GPa)	C_{12} (GPa)	C_{44} (GPa)	B (GPa)	G (GPa)	E (GPa)	ν	B/G
Our PBE	223.85	81.25	64.54	128.78	67.16	171.65	0.28	1.92
PBE + U	216.22	81.84	62.65	126.63	64.43	165.26	0.28	1.96
PBE ²²	196.41	82.16	60.61	120.24	59.19	152.54	0.29	2.03
PBE ³⁸	—	—	—	128	75.52	189.28	0.25	1.69
PBE ²³	264.94	89.24	87.85	147.81	87.84	219.96	0.25	1.68
Expt ³⁹	—	—	—	121	—	—	—	—

1.5 Summary

Since the discovery of the TE effects, various improvements were brought to the TE materials to raise the value of ZT . As a result, the microstructure reached the nanoscale to lower the thermal conductivity through phonon scattering process.

Among the new TE materials with high ZT , those suitable for medium to high temperatures such as the half-Heusler alloys would be a fit for building new TEG. Harvesting the wasted heat with a TEG to produce electrical power is a valuable step forward in terms of energy management. Indeed, such progress could enhance the output of a thermal engine, without increasing the initial fuel consumption nor its service conditions.

If data on TE parameters are extensive, data on mechanical properties of TE materials are often limited to hardness and elastic modulus, as they are used as a guidance to process new materials. There is thus a lack of mechanical data in the TE literature, and deformation mechanisms remain unknown except for very few examples.

With time, the processing methods for higher ZT , such as nanostructuring, become as complex as ingenious. In addition, dislocations are being considered as a tool to tune TE properties. Indeed, it is common knowledge for dislocations to impact the electrical resistivity, or the thermal conductivity via various mechanisms. Today, studies with dislocation-engineered TE materials are published, perhaps opening the way to defect-engineered processing routes. As a part of deformation mechanisms, microstructural defects play a major part in materials engineering as witnessed with the semi-conductors. Therefore, there is a necessity to study their properties in the TE field.

As the literature review suggests, an increased dislocation density in a TE material has the potential to enhance the ZT. The prospect of increasing the ZT by plastically deforming a sintered pellet is valuable from both scientific, and technical perspectives. This would translate into an extra processing step, right after sintering, where the formed pellet would be deformed by compression to attain the required amount of strain for ZT optimization. From this perspective, the following goals were initially set for the present study:

1)-Study the plasticity of a TE material

This first step allows to understand to what extent the material tested can deform plastically. To maximize the chances to trigger plasticity, the original uniaxial compression experiment under confining pressure (Paterson machine) is proposed as a proven method to enable plasticity mechanisms by dislocation activity in usually brittle materials. With this experiment, the amount of plastic strain available from the material is determined as preliminary data to goal n°2, as well as the deformation mechanisms associated. In addition, the dislocation density is determined for as-processed samples, which associated to the ZT values already published will constitute the first data point for the study of dislocation density vs. ZT

2)-Increase of the dislocation density

The material is deformed to various amounts of plastic strain with the Paterson machine. The dislocation density is characterized as a function of the plastic deformation via TEM observations.

3)-Fundamental approach to study the evolution of ZT vs. dislocation density

Plastically deformed TE material specimen are tested for their ZT, Seebeck coefficient, thermal conductivity, electrical conductivity values in a Physical Properties Measurement System (PPMS). This process enables an understanding of how the dislocation density impacts the TE properties.

However, the present study in Chapter 3 demonstrates that the goal n°1 for the study of plasticity is clearly not possible, supported by the exclusively brittle behavior of the material in the Paterson machine. Hence, goals n°2 and n°3 had to be dropped, and the whole workplan was transformed into a study of deformation mechanisms.

The p-type half-Heusler $\text{Hf}_{0.44}\text{Zr}_{0.44}\text{Ti}_{0.12}\text{CoSb}_{0.8}\text{Sn}_{0.2}$ has been selected for the deformation mechanisms analysis of this dissertation. To assess these mechanisms, a multi-scale approach is proposed:

- Bulk compression testing will gather additional engineering data on the material and provide a first assessment of the plasticity in this alloy. To push the study further the Paterson machine will be used with the goal to enforce plasticity in the alloy by using a hydrostatic pressure environment to prevent crack nucleation and propagation.
- At the meso-scale, defects will be inserted in the material by nanoindentation toughness procedure. This method generates radial cracks, which could carry plasticity at the crack tips. Fracture path and potential plasticity events will be analyzed by TEM and 3D-EBSD techniques.

- Small scale compression testing on micropillars will give access to elementary deformation mechanisms and assess eventual size effects.

This multi scale set of experiments will provide a comprehensive mechanical study on the p-type half-Heusler $\text{Hf}_{0.44}\text{Zr}_{0.44}\text{Ti}_{0.12}\text{CoSb}_{0.8}\text{Sn}_{0.2}$.

Chapter 2 : Experimental methodology

2.1 Microstructure characterization

2.1.1 Surface preparation

The following two methods provided ceramographic surface preparation throughout this project.

Preparation 1: Successive mechanical polishing with SiC abrasive paper 600, 800 and 1200 grit, then with diamond suspended solution with successively 1 μ m and 0.25 μ m particle size

Preparation 2: following preparation 1, a complementary polishing is applied in colloidal silica suspended solution in a vibrometer for 24 hours.

2.1.2 Focused Ion Beam (FIB)

The FIB used for this study is located in the FEI Helios Nanolab G3CX dual-beam at the PPrime Institute. It is used for milling tasks involved in this work, using a Ga⁺ ion source at specific voltage and currents. The FIB is used in various procedures that will be described independently.



Figure 2.1: NANOLAB FIB at PPrime Institute, University of Poitiers

2.1.3 Scanning Electron Microscopy (SEM)

2.1.3.1 SEM imagery

The majority of SEM images were acquired with the JEOL 7001F-TTL (PPrime Institute), equipped with a Field Emission Gun (SEM-FEG) for high resolution and an Energy-dispersive X-ray spectroscopy (EDS) detector for chemical analysis as well as a secondary electron and backscattered electron detectors. The SEM scans a surface, generating an image from the interaction of the focused electron beam with the surface atomic layers. A variety of signals is incoming from the surface along the path of the electron beam such as secondary electrons, back-scattered electrons, X-rays, as detailed in Fig.2.2. The secondary electrons will provide high resolution topography information, while the backscattered, will be sensitive to topography and chemistry of samples. This SEM is used for microstructural analysis, fracture surface analysis, in addition to a ZEISS Gemini LEO 1525 SEM located at University of Houston. In addition, the electron column

in the FEI Helios Nanolab G3CX dual-beam provides imagery during procedures involving FIB milling, and post-milling verifications.

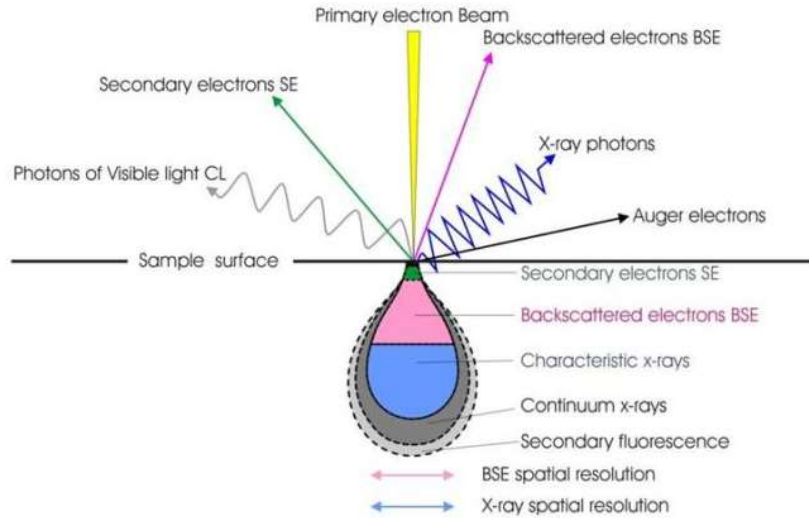


Figure 2.2: Electron interaction bubble with the scanned surface

2.1.3.2 Energy-dispersive X-ray Spectroscopy (EDS)

The EDS detector collects emitted X-ray from the surface due to the electron beam-surface interaction. When a sample is bombarded with an electron beam, electrons of the atoms in the interaction bubble ($\sim 1\mu\text{m}^3$) are ejected from their orbitals. These vacancies are filled with higher states electrons, which release energy by emitting an X-ray during the radiative transition. The energy of the emitted X-ray is characteristic of the element it is originated. The EDS detector will measure the intensity of the emitted X-rays and their respective energy and translate it into an atomic proportion in presence at a pixel location. On a wider scale, this process can be used to generate color-coded maps for each element in presence.

Surface preparation:

The surface for SEM and EDS observations were prepared following preparation 1.

2.1.3 Scanning Transmission Electron Microscopy (STEM) and Transmission Electron Microscopy (TEM)

The thin foil for TEM observation were prepared either by FIB lift-out technique from surfaces following preparation 2 or by mechanical preparation on surfaces following preparation 1:

1) The lift-out technique allows to extract a lamella, followed by ion beam thinning. The parameters for milling TEM foils are 30kV acceleration voltage and 9nA current, then 3nA for finer milling. Once ready for observation, these thin foils can be pre-checked for electron transparency with the STEM detector built in the same apparatus, prior to be observed in the TEM JEOL 3010 operated at 300 kV for better resolution. The procedure is illustrated in Fig. 2.3.

2) The mechanically prepared thin foils were first thinned down to 70 μ m to 100 μ m thickness by mechanical polishing. The sample is then thinned using a dimpler equipped with a rotating textile wheel sprayed with 0.25 μ m diamond paste with the force applied on the sample adjusted continuously to be minimal but acting on the sample topography. As soon as a hole is created, the sample is taken to a Precision Ion Polishing System (PIPS) for extra thinning around the hole with two successive PIPS procedure. First, the sample is thinned down with a beam angle of $\pm 8^\circ$ at 3 rpm, 3 keV and 13 μ A for 2 hours, then for

precision thinning the parameters are $\pm 4^\circ$ beam angle, 1.7keV, 3 μ A and 20min. This procedure creates an electron transparent band around the hole where TEM observations can be carried out.

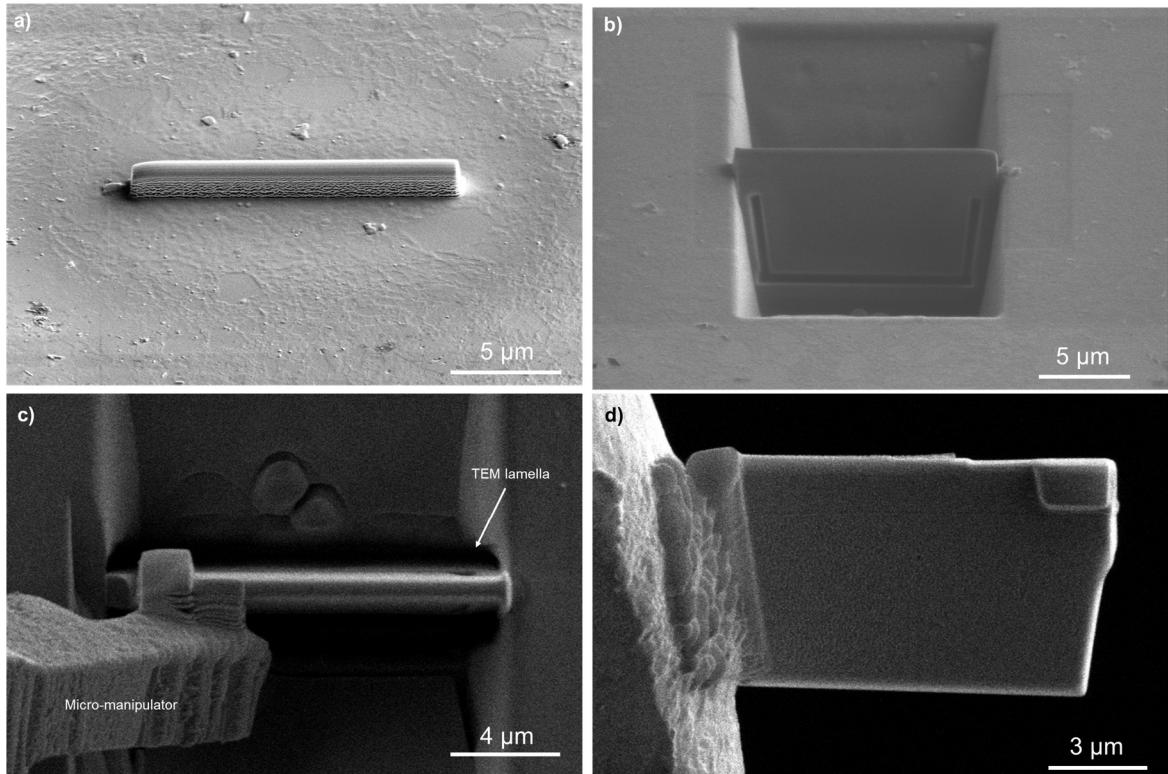


Figure 2.3: **a**-Pt layer deposited before FIB milling **b**-TEM lamella milling under progress **c**-Lift-out technique under progress **d**-TEM lamella Pt-welded to the Cu grid before thinning

2.1.4 Electron BackScattered Diffraction (EBSD)

The EBSD maps are collected with an EDAX HIKARI Super PV 5500/SU-H camera from EDAX, located in the FEI Helios G3 CX Dual-Beam, with identical parameters regardless the pixel size: 10kV and 22nA. The collected maps are then treated and analyzed with the OIM 7 software.

The camera collects backscattered electrons from the surface, tilted at 70 degrees from horizontal, and 20° from the electron beam as represented in Fig 2.4 [89]. Diffracted by various crystallographic plans, backscattered electrons will form Kikuchi patterns that will be indexed at each position of the electron beam.

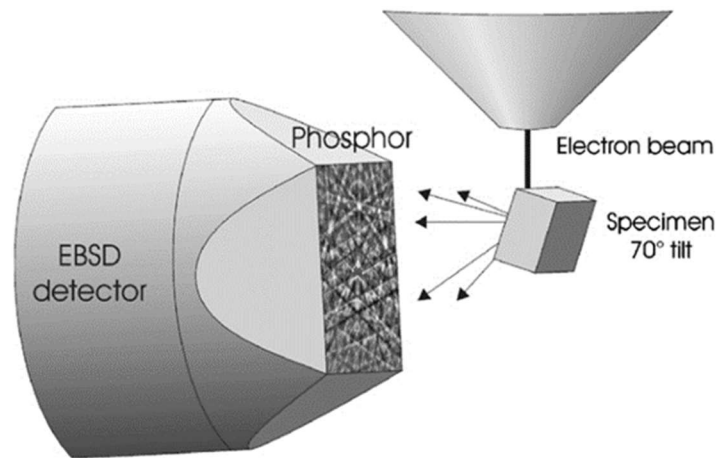


Figure 2.4: EBSD setup

This way, the crystallographic structure and orientation in presence can be determined with the inverse pole figure (IPF). The IPF information can be converted into map, that will be colorized according to the crystallographic environment in presence. EBSD data also provides Image Quality (IQ), which is a metric describing the quality of a diffraction pattern. An IQ map is constructed by mapping the IQ value measured for each diffraction pattern. The IQ is sensitive to the lattice in presence in the diffracting volume, in a sense that a perfect lattice would provide a perfect diffraction pattern. However, an elastically strained lattice for instance would not satisfy the Bragg condition, hence a more diffuse diffraction pattern. In the case of plastic deformation, the presence of dislocations will reflect as set of regions of slightly different orientations with respect to one another, that will superpose and result as well in a more diffuse pattern [90]. IPF and IQ data can

be superposed in a single map. The different maps and imagery available are represented in Fig 2.5.

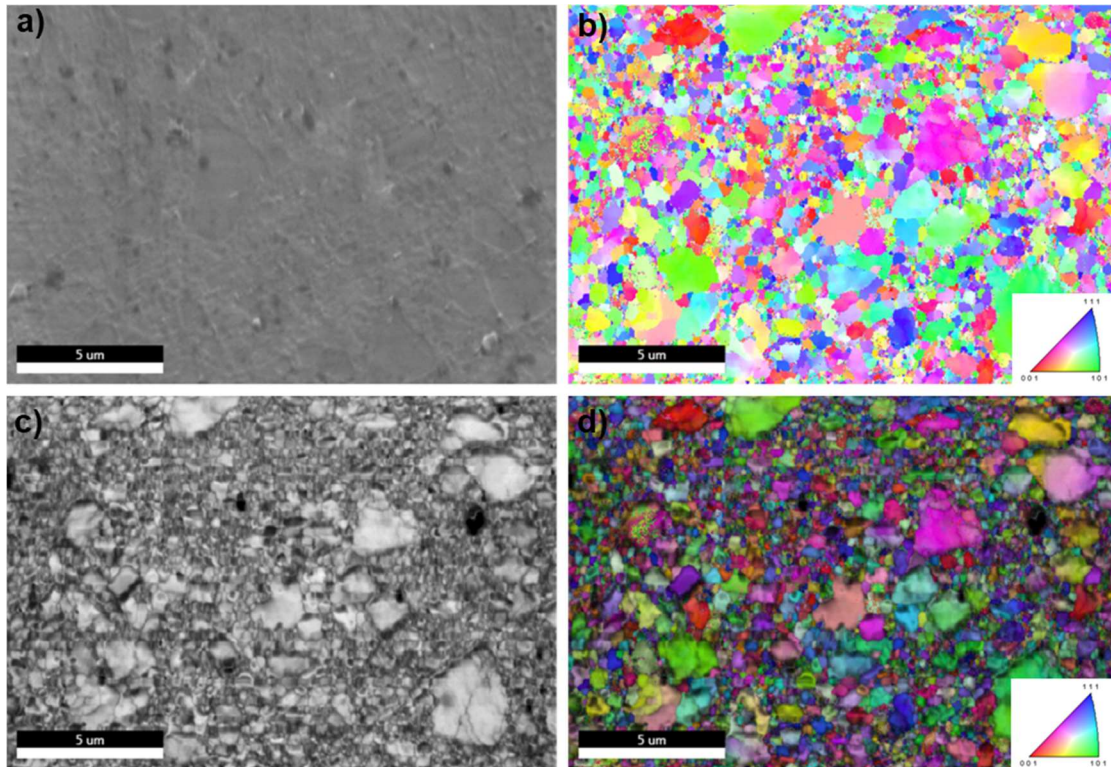


Figure 2.5: imagery from EBSD with a 10nm pixel size of the same area seen as: **a**-SEM image; **b**-IPF map; **c**-IQ map; **d**-Superposition of IQ and IPF map

2.1.5 3D Electron BackScattered Diffraction

2.1.5.1 FIB serial sectioning procedure

SEM characterization is a surface related technique which cannot provide volume-related data. This is why FIB sectioning procedure was developed to study a volume, by a 3D imagery technique. This procedure is conducted in a dual-beam machine, such as the Helios G3CX Nanolab Dual-Beam, where the presence of both ion and electron column is the optimum combination for high resolution slicing and imaging. At first, a selected volume is prepared, by milling out wide trenches around it by FIB. This allows the electron

beam to scan the carved surface as represented in Fig. 2.6 [91]. After a first SEM acquisition, the image is collected, and a layer of this surface is removed by FIB. The thickness of the layer has to be consistent with the material features to be imaged (grains, coating thickness...). The fresh surface is imaged by SEM, contributing to the future stack of images of the volume analyzed. Indeed, the procedure consists in a repetitive sequence of imaging by SEM and slicing by FIB of the prepared volume. Then the stack of images can be reassembled as a 3D-volume for analysis. This whole procedure is also known as “slice-and-view”.

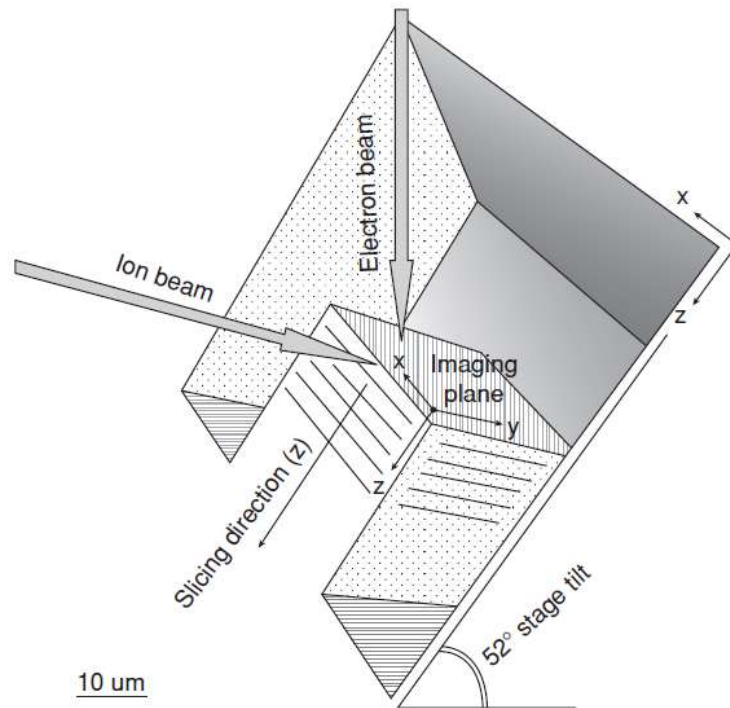


Figure 2.6 illustration of the FIB serial sectioning procedure

2.1.5.2 Evolution toward 3D-EBSD

Initially developed for 3D SEM imagery [92], the slice-and-view method can as well be adapted to EBSD mapping. Beyond regular imagery, 3D-EBSD provides data

describing the structure and crystallography of grain-level microstructure, in three dimensions. This technique combines EBSD mapping and FIB machining, as the FIB slices down a volume of interest while each fresh surface is scanned by EBSD. However, as the EBSD mapping necessitates the surface is oriented with a narrow angle of 20° from the electron beam (Fig. 2.4), the FIB sectioning technique requires adaptation.

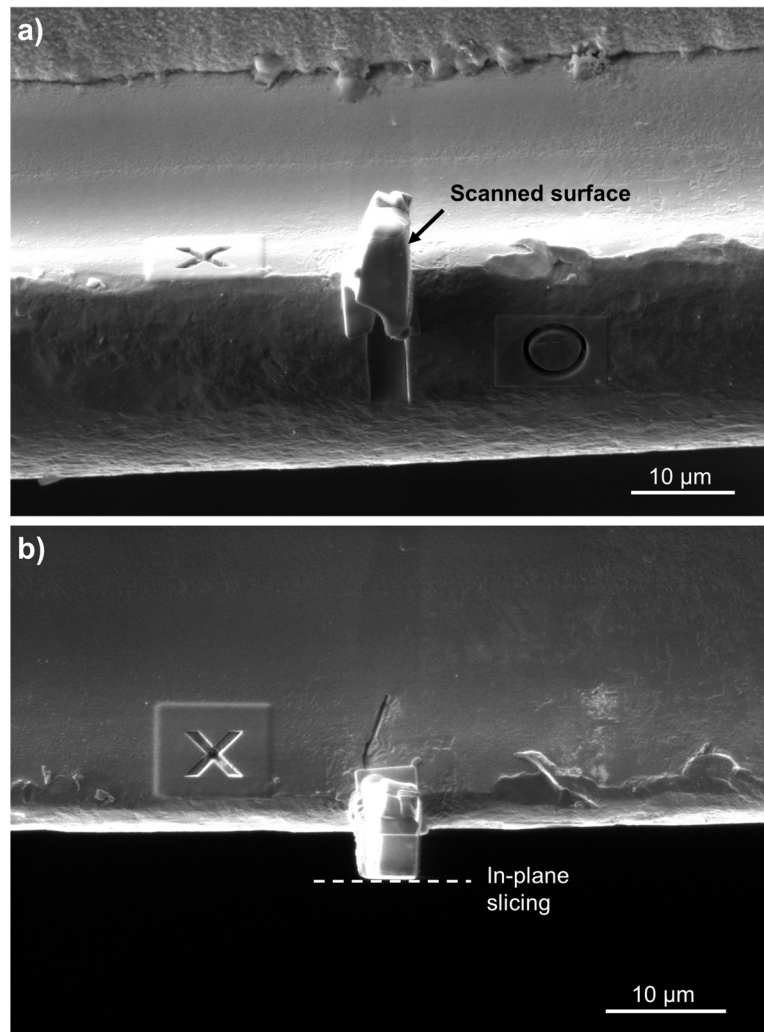


Figure 2.7: a- Front view of a cubic specimen showing the surface scanned by EBSD b- Upper view highlighting the incident ion milling procedure

The major difference with the classical slice-and-view procedure consists in excavating the volume of interest with the lift-out technique and solder it to a TEM grid via Pt deposition prior to the unchanged “slice and view” steps. The first step consists of acquiring an EBSD scan on a selected surface with a 20nm pixel size (Fig. 2.7a). Once this scan is collected and stored, a 50nm layer of the mapped surface is milled out by FIB (Fig. 2.7b). The new surface is subject to the same slice and view process, adding an EBSD map to the stack at each iteration. This method generates a stack of EBSD maps spaced of 50nm from each other in the original volume. The EBSD maps are treated with the OIM 7 software, for correction of pixels assimilated to noise in the signal. This whole treated stack is analyzed with the Avizo 9 software where each slice is connected to each other with particular attention to avoid any artificial shift. The 2D grains are extrapolated in the third direction to fill the gap originally existing between the maps, rendering the 3D volume as a single dataset, with a voxel size of $50 \times 20 \times 20 \text{ nm}^3$. An example of a 3D assembled stack of EBSD map is presented in Fig. 2.8, with a specimen of Ti-6Al-4V [93], [94], with a 250 nm^3 voxel size and a total volume of $35 \times 35 \times 55.5 \text{ } \mu\text{m}^3$.

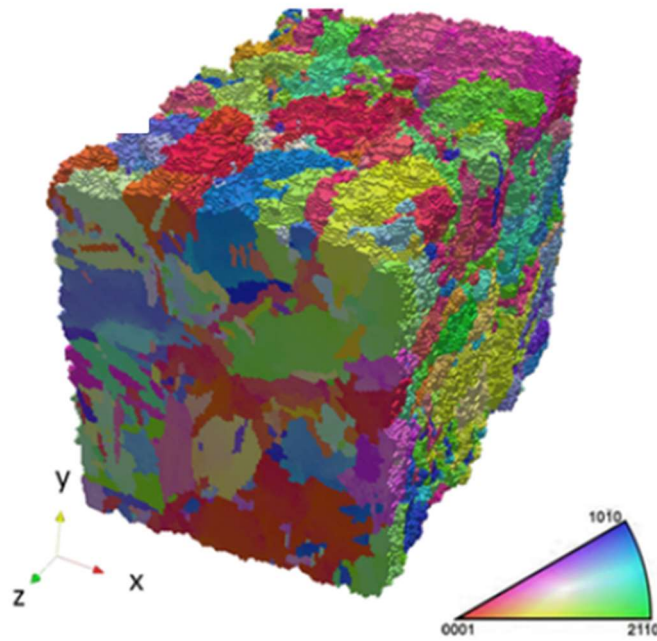


Figure 2.8: example of a reconstructed volume via 3D-EBSD of Ti-6Al-4V

2.1.6 X-Ray diffraction

The material was analyzed by X-ray diffraction in a Bruker D8 at the PPrime Institute, equipped with a Cu anode (associated wavelength $K\alpha_1 = 0.15406$ nm, $K\alpha_2 = 0.15444$ nm) at 40kV and 40mA. The sample is scanned by X-rays with the Bragg-Brentano $\theta-2\theta$ setup, from 20° to 100° with a step size of 0.02° and a pause of 2s at each step. During the process, only the X-rays source and the detector are un movement while the sample stays in its original position and orientation, and data are collected with the software XRD Commander. The generated spectrum is intensity vs. angle of diffraction which allows to identify the phases in presence. The diffractogram analysis is done with the software EVA to match it with a database.

2.1.7 Grain size analysis

Intercept method on TEM images

This method applies to microscopy images of a microstructure to determine the average grain size in presence [95]. Several lines are drawn, and each grain boundary encountered along the line is marked. Then the line length is divided by the number of marks, for which the result is associated to the average grain size diameter along this line. To ensure result validity, several lines must be drawn, along various direction. This method can be applied and only if the grain shape is rather isotropic, as the grain size determination by line along preferential direction would not be valid or relevant.

EBSD scan analysis

The software OIM 7 allows to use several methods to determine the grain size in presence. The intercept method is one of them where the number of lines can be determined as an input parameter. However, this is rather limited when the informations collected in a EBSD map are considered. Indeed, as each indexed pixel corresponds to a crystallographic orientation, it is possible to calculate the grain size more accurately, by using the parameters “minimum grain size” and “grain tolerance angle”. The minimum grain size has to be accounted for in relationship with the pixel size used for the scan and the microstructure in presence. Indeed, this parameter has to be set to as least the size of a few pixels (5 to 10) to ensure that isolated pixel cluster will not be considered as a grain. The grain tolerance angle must be carefully adjusted if the grain size is textured, or if substructures are present within grains. Indeed, if the grain tolerance is set to high values, neighbor pixels with an orientation differing within the tolerance angle will be considered

as a single grain. In opposition, if the value is set too low, local misorientation could be identified as separated grains.

2.2 Mechanical Characterization

2.2.1 Classical compression test

The samples tested are cuboids with a typical size of $4 \times 4 \times 5 \text{ mm}^3$ and are tested in compression at room pressure (RP) and room temperature (RT) between SiC rods with a flat end in an Instron 5584 load frame at a strain rate of $8 \cdot 10^{-4} \text{ s}^{-1}$ until failure. For this setup, the sample is placed between two SiC rods that are connected to the machine with stainless steel fixtures. The top fixture is assembled in a load cell with a 100 kN tolerance and the bottom one is assembled to the load frame. The critical part of a compression test is to ensure the surfaces of the SiC rods are parallel to ensure homogeneous force repartition during the test. The sample is loaded at the designated strain rate, and the displacement is recorded at the extremities of the specimen with an optical setup. The test is complete upon sample failure.

Surface preparation:

Cuboids samples are cut with a diamond coated blade mounted in a surface grinder. The typical size of these samples is $4 \times 4 \times 5 \text{ mm}^3$. Each surface of the samples is then prepared following preparation 1. The goal of this polishing procedure is to minimize surface defects where crack propagation could initiate.



Figure 2.9: Compression Setup at the University of Houston, here equipped with a furnace

2.2.2 Compression test with hydrostatic pressure environment

Originally designed to reproduce the earth mantle conditions in pressure and temperature for rock deformation, the Paterson machine performs uniaxial compression with a surrounding isostatic pressure environment with the possibility to raise the temperature of the tested sample [96]. This apparatus is conceived with a high-pressure chamber, pressurized with Ar gas with a capacity up to 600MPa, which is equipped with a furnace that can reach 1400K.

The sample is inserted in a sample-holder column, made of successive alumina and zircon pistons, all wrapped in an annealed Fe jacket. The force and the displacement are recorded from below the sample, the deformation speed can be set between $5 \cdot 10^{-2} \mu\text{m} \cdot \text{s}^{-1}$ and $500 \mu\text{m} \cdot \text{s}^{-1}$, and the load cell limit reach 100 kN.

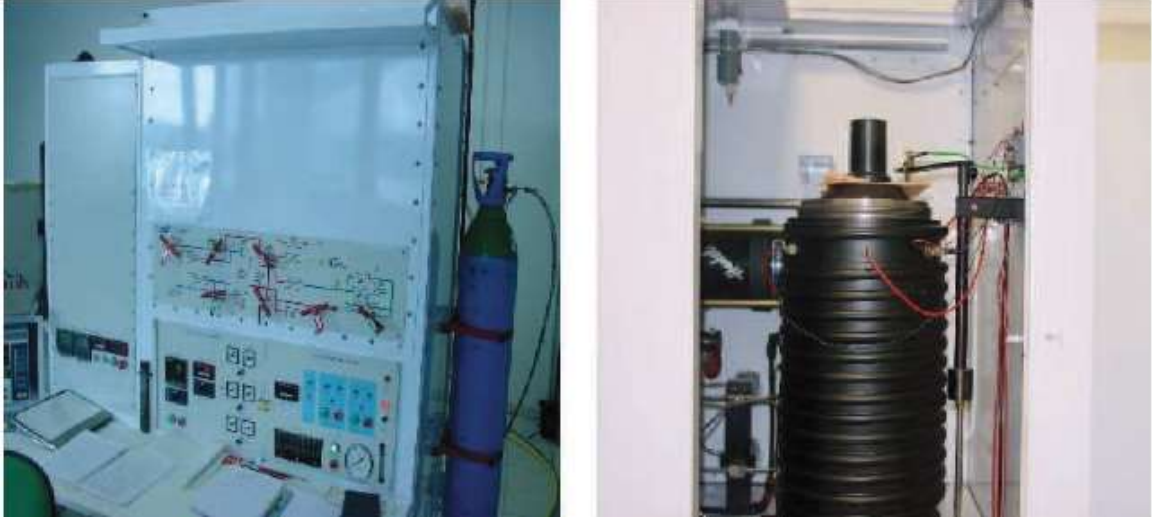


Figure 2.10: Paterson Machine at the PPrime Institute

The samples are cuboids cut from a pellet with a wire diamond-coated saw. To fit in the assembly, a circular column, these are inserted in an aluminum jacket with a circular exterior cross-section, while the internal cross section is cubic to fit the sample. When the sample is inserted into the Al jacket, the sample-jacket assembly is stacked between successively an alumina disc and a zirconia piston on both sides. The nature of these pistons is chosen on purpose: the alumina allows a heat conductivity and the zirconia helps to prevent the heat conduction farther from the stacking. On both sides of the sample, the zirconia pistons are drilled with a hole that guides a thermocouple to the alumina disc as possible to the sample as represented in Fig. 2.11 [97] . The whole piston and sample assembly is then inserted in an external annealed iron jacket, forming the sample-holder assembly. Both ends of that assembly are plug in the external compression pistons, sealing the system.

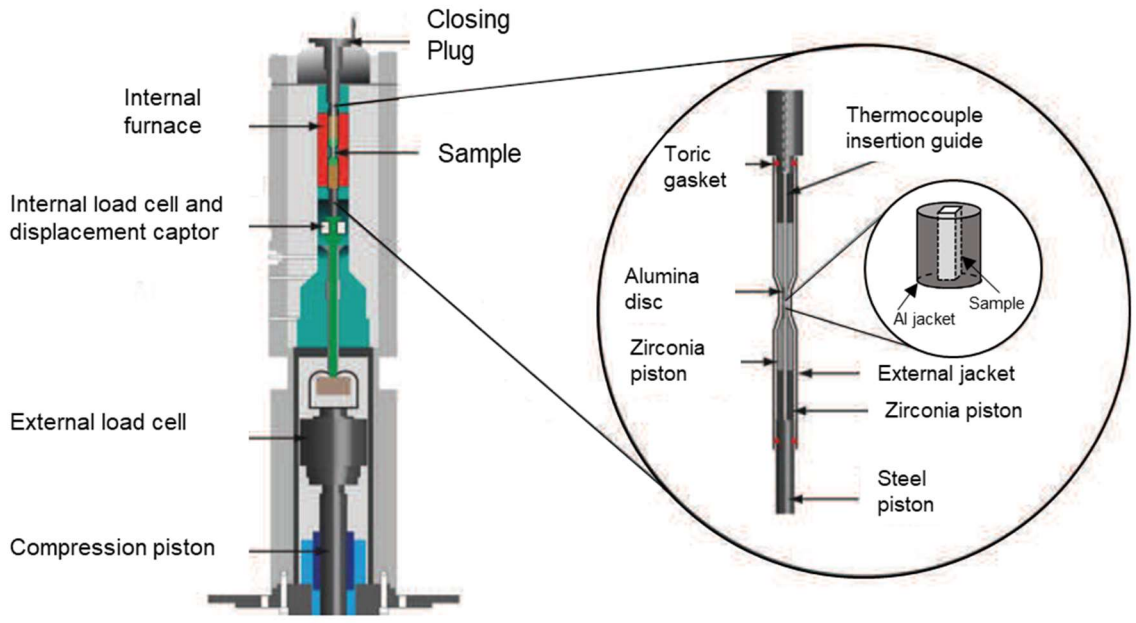


Figure 2.11: Schematics of the pressure vessel and sample column

The testing procedure occurs as follows. At first the hydrostatic pressure “P” is applied inside the pressure vessel containing the sample assembly, then the uniaxial stress component “ σ ” is applied along the 33 axis with a strain rate of 10^{-4}s^{-1} . The stress application on the sample can be represented as

$$\sigma_{total} = \begin{pmatrix} P & 0 & 0 \\ 0 & P & 0 \\ 0 & 0 & P + \sigma \end{pmatrix}. \quad (2.1)$$

After a test, the collected stress-strain curve contains information on both the sample and the Al jacket need. These data require deconvolution to separate the aluminum jacket and the sample stress contributions, to access to the stress independently applied on the Al jacket and on the sample. This is done by using a rule-of-mixture law, with the following parameters: the volume fraction of the sample (χ_{sample}) and of the Al jacket

(χ_{jacket}), the stress applied to the sample plus jacket assembly ($\sigma_{assembly}$), the stress applied to the sample alone (σ_{sample}) and the stress applied to the jacket alone (σ_{jacket}) and is expressed as

$$\sigma_{assembly} = \sigma_{sample}\chi_{sample} + \sigma_{jacket}\chi_{jacket}. \quad (2.2)$$

As the stress information collected from the Paterson apparatus is $\sigma_{assembly}$, one can use Eq 2.2 to isolate the stress applied to the sample (σ_{sample}). At this stage, two values are unknown, σ_{jacket} and σ_{sample} . The value of σ_{jacket} is obtained from a benchmarking experiment on a plain cylindrical Al sample, tested in the same conditions. This experiment produces a stress-strain curve that is modeled to fit the strain obtained on the curve $\sigma_{assembly} = f(\epsilon_{assembly})$, which allows to evaluate σ_{jacket} and calculate values for $\sigma_{sample} = f(\epsilon_{sample})$.

Previous studies with the Paterson apparatus allowed to trigger the plasticity in brittle materials, reaching higher stress using the Paterson apparatus than using a classical compression test set up at ambient pressure [97]–[100].

Surface preparation:

The sample surface preparation is identical to the classical compression test specimen preparation (preparation 1). When the sample is inserted into the Al jacket, one end of the assembly (sample and jacket) is grinded so both elements match the exact same height. The goal of this sample preparation is to remove any surface defect where crack propagation could initiate on the surface and remove any possible surface hardening caused by the sawing.

2.2.4 Mesoscale testing: controlled crack insertion by nanoindentation

2.2.4.1 Nanoindentation

Nanoindentation is a widely used method to measure material properties such as hardness and elastic modulus at small scale, with the standard apparatus represented in Fig.2.12 [101]. Using ultra low load in the mN range, a nanoindenter is a compression testing machine with high resolution in load and displacement. A nanoindentation test is analogous to a classical hardness test where a pointy head will penetrate the surface, giving access to specific materials properties. The indenter is a diamond tip that can have many shapes, and the surface of the created indents can be characterize by AFM analysis and SEM observations.

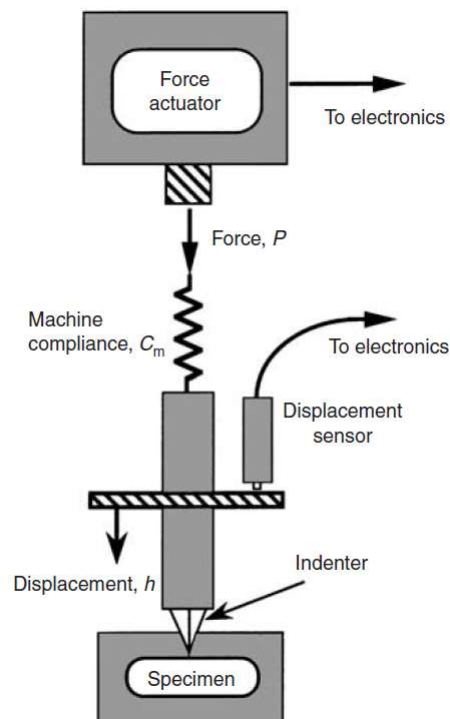


Figure 2.12: schematics of a nanoindenter

The nanoindenter model used in this study is the *MTS Nanoindenter XP* located at the University of Houston, and the data are processed by the Testworks 4 software. As the nanoindenter is sensitive to environment variations such as acoustic vibrations and temperature, the maximum drift value allowed for a test to start is 0.50nm/s. In addition, the machine compliance is assessed by a calibration on a fused silica specimen.

The nanoindenter is adapted to small scale mechanical experiment, conducted either in load or displacement control. In addition, the variety of tip shapes allows to transfer classical macroscale testing to a nanoindentation procedure. For instance, fracture toughness can be performed at small scale with a cube corner tip, and compression of micro-specimen is possible with a flat-punch tip.

Surface preparation:

For nanoindentation experiments, the surface preparation follows the preparation 2 as the surface needs to be flat, and defect free.

2.2.4.2 Controlled crack insertion

To characterize a crack propagation in the material, the nanoindentation fracture toughness method is applied for controlled crack insertion with a cube corner tip, which is commonly used for nanoindentation toughness studies [102]. This tip is a three-sided pyramid that has the geometry of the corner of a cube, where the center-line to face angle is 35.3° . For comparison this value for the Berkovich tip is 65.3° . The narrow angle of the

cube corner tip translates into inducing higher stress at the indent location, useful for inserting cracks in the affected area.

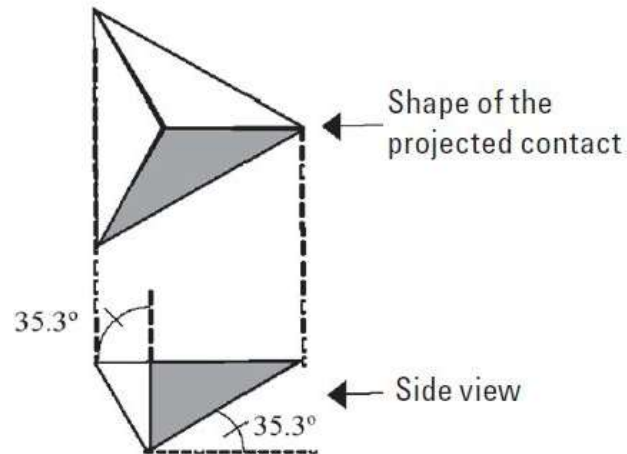


Figure 2.13 : Cube corner tip profile

For our study, the indents are generated with a load control procedure. The loading procedure is a 30s loading phase and a 10s of load holding before unloading. Initially, a grid of indents is inserted in the surface, with a load increment of 5gf from 5gf to 30gf, with 20 indents per load (Fig 2.13a).

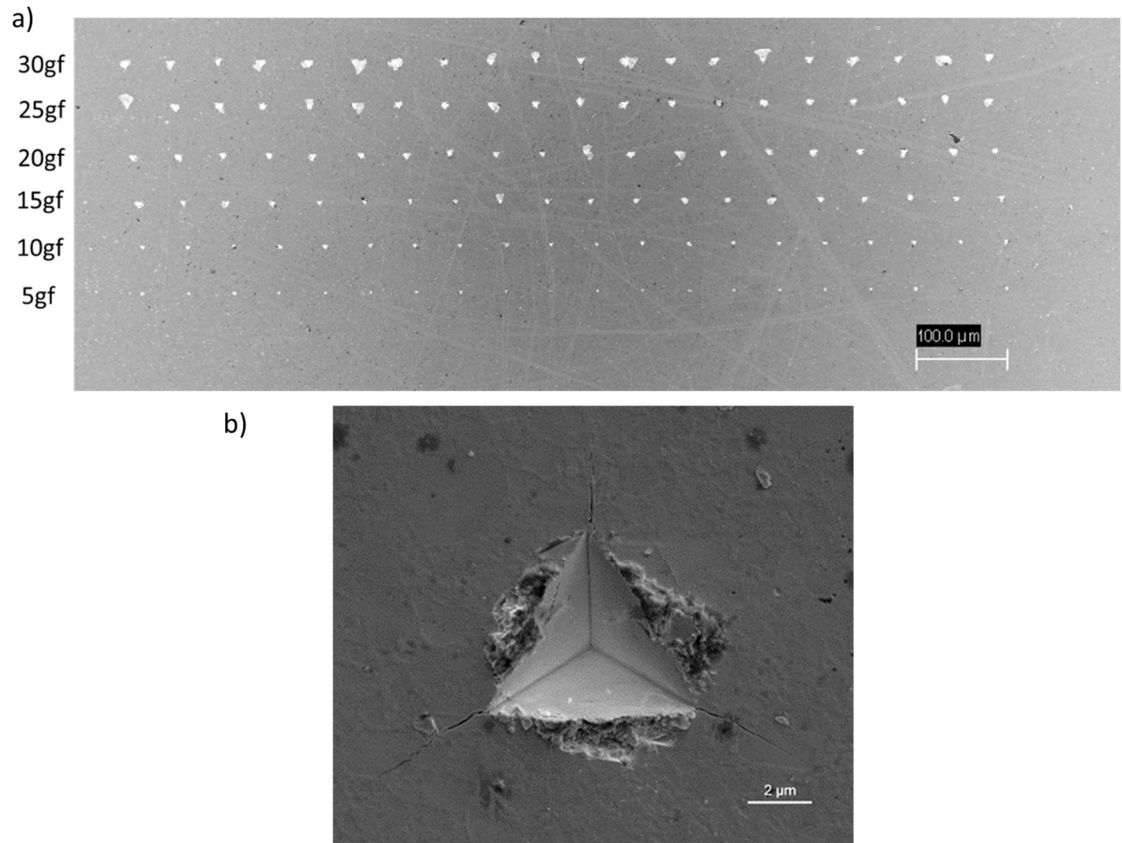


Figure 2.14: **a**-Grid of indentation generated with the cube corner tip from 5gf to 30gf **b**-example of a 20gf (~200mN) indent selected for the study

One indent generates three radial cracks departing from the indent tips (Fig. 2.14b). These radial cracks are then subject to three kinds of observation:

- 1) Surface observation of indented region (SEM and EBSD)
- 2) Extraction of TEM thin foil at the crack tip for dislocation analysis
- 3) 3D-EBSD tomographic reconstruction of an extracted volume containing the crack

The indent size and the associated crack length increase with the load applied as shown in Fig. 2.14a. Indents made with 20gf load were chosen for the study, as the associated crack

length (approx. $4\mu\text{m}$) fits into the limitations of the 3D-EBSD method, where considering the machine-time necessary to complete the slice and view process, a reasonable volume is about $5\times 5\times 5\mu\text{m}^3$.

2.2.5 Micro-compression

While bulk testing of a material can assess the material resilience to environmental stress, local mechanical investigation will enable to trigger intrinsic deformation phenomenon and unveil possible size effects [103]. A set of rectangular pillars are milled out by FIB at random location, rendering a representative microstructure of the alloy with the goal of assessing local plasticity. This type of experiment will also help to assess the fracture behavior and mechanisms associated with opening a grain boundary between the large grains and the small-grain matrix.

2.2.5.1 Pillar preparation

On a surface prepared following procedure 2, the procedure for making the micropillars starts with a 200nm thick Pt deposition on the material surface. This will act as a mask to protect the selected volume from Ga implantation-induced defects, where the pillar will be machined by FIB. The volume around the future pillar is then milled by FIB (30kV, 9nA), with a sufficient size so the nanoindenter tip can compress the pillar without touching the original surface. Then a finer milling (30kV, 3nA) is done on the pillar to give it its final shape and size, $6\mu\text{m}$ height with a $2\times 2\mu\text{m}^2$ square cross section.

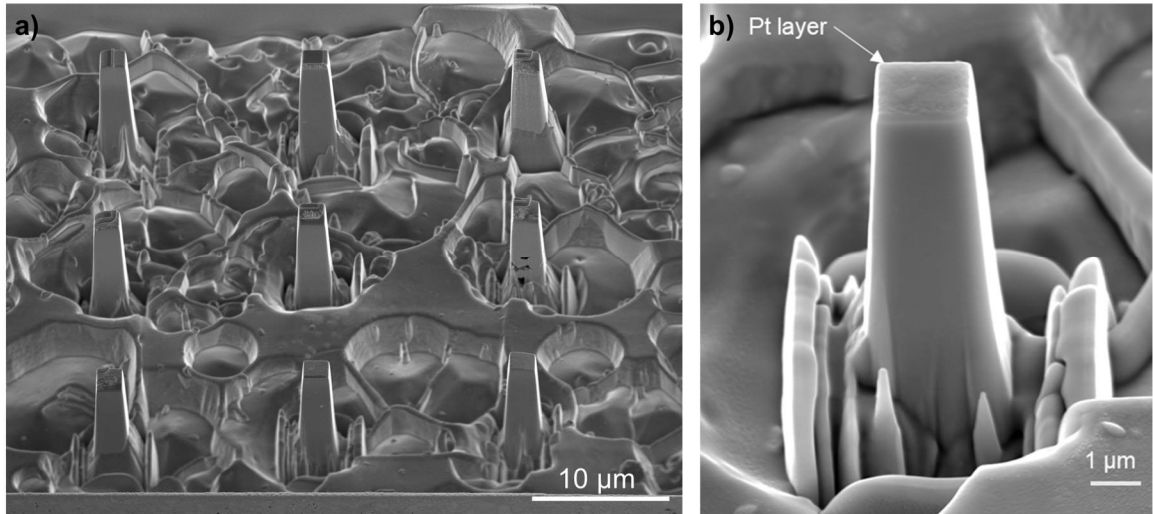


Figure 2.15: **a**-A set of 9 micro-pillars milled out by FIB **b**-A single micropillar ($2 \times 2 \times 6 \mu\text{m}^3$) with the Pt layer on the top

2.2.5.2 Nanoindentation procedure

-Surface altitude recording

The nanoindenter is equipped with a flat punch tip of $10 \mu\text{m}$ diameter, to ensure a wide contact with the pillar top surface and avoid indenting it. The procedure starts by recording the surface altitude of the sample by touching the surface with the tip in a selected location nearby the pillar cavity. With this information stored, during a test, the speed of the tip will decrease accordingly to avoid crashing on the pillar. When the contact with the pillar surface is detected, the speed of compression will match the speed imposed by the operator to conduct the compression test.

-Pre-loading

Before initiating the deformation of the micro-pillar, a pre-loading is applied with a minimal depth target, usually up to the thickness of the Pt layer (200nm). The sample

pre-loading ensures the tip detects the pillar surface correctly, and compress the Pt layer to later minimize its effects during the pillar compression.

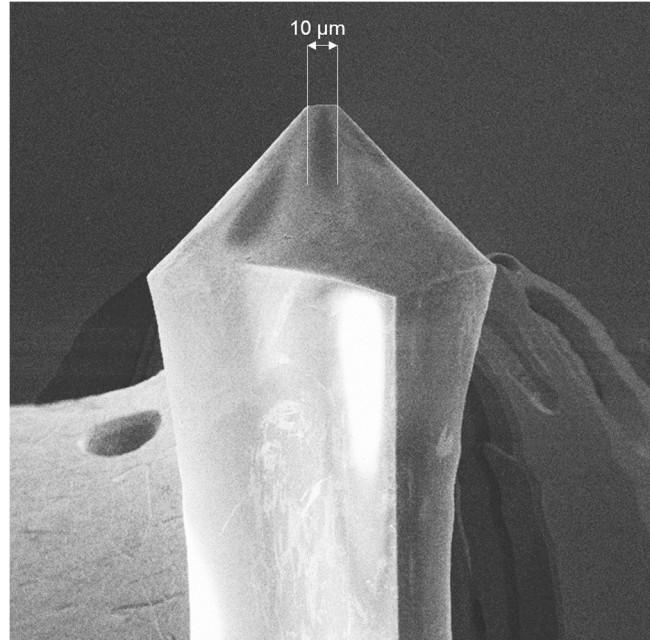


Figure 2.16: Flat punch tip with 10 μm diameter used to compress the pillars

-Compression

The *Nanoindenter XP* is exclusively working with a load control procedure, meaning only a load is authorized as an input value. This procedure has been altered into a depth control procedure. Thus, when the tip detects the pillar surface, it will then reach the depth value chosen by the operator. As the strain rate is imposed by the machine (0.05 s^{-1}), the speed of compression is tied to the depth target. To observe eventual signs of plasticity on the stress-strain curve without breaking the micropillar specimen, the depth input was successively increased test after test. During a test, the nanoindenter records the load and the displacement, therefore, the stress is calculated by dividing the load by the area of the top of the pillar.

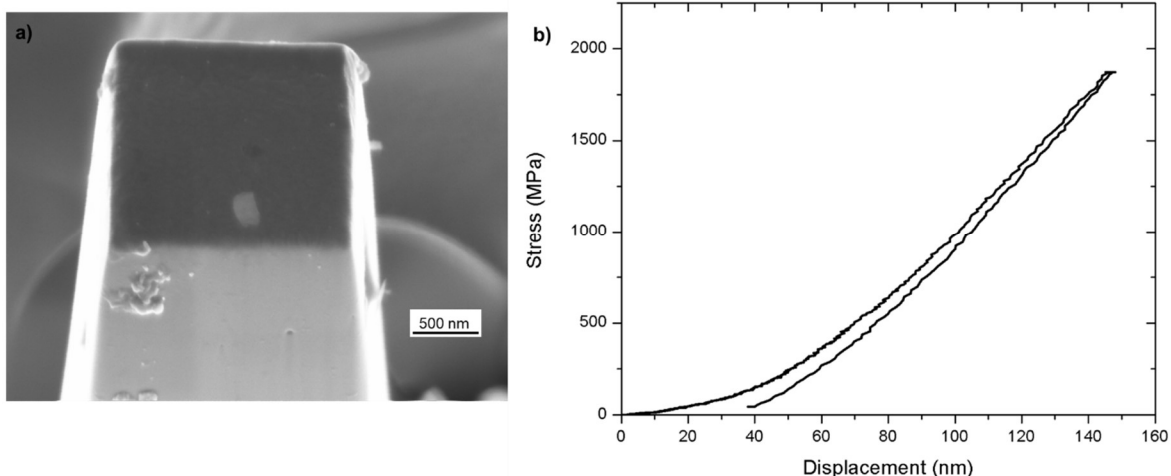


Figure 2.17: **a**-pillar surface after pre-loading with Pt debris **b**-stress-strain curve of a pre-loading

2.2.5.3 The Sneddon correction

The raw stress-strain curves obtained for micro-pillar compression do not display the true behavior of the specimen tested. Indeed, the overall stiffness recorded during a nanoindentation micro-compression test accounts for the combined effects of the compliance of the pillar itself as well as the compliance of the pillar acting like a flat punch indenter, elastically deforming the bulk material beneath it. In order to calculate the true pillar stiffness, this additional compliance needs to be removed as demonstrated in past studies on micro-pillar compression [104]. Sneddon described a solution for a perfectly rigid circular flat punch indenting into an isotropic elastic half space [105], for which the expression provided is

$$C_{Sneddon} = \frac{\sqrt{\pi}(1 - \nu^2)}{2E\sqrt{A}}. \quad (2.2)$$

In this expression, E is the elastic modulus of the material, ν its Poisson's ratio, and A is the area of the pillar cross-section. The pillar stiffness (S_{Pillar}) is then calculated by subtracting the Sneddon compliance ($C_{Sneddon}$) from the inverse of the stiffness measured by the nanoindenter (S_{nano}) as

$$S_{Pillar} = \frac{1}{(1/S_{nano}) - C_{Sneddon}}. \quad (2.3)$$

With the true pillar stiffness value, the corrected elastic modulus ($E_{Sneddon}$) is calculated from the relationship

$$E_{Sneddon} = \frac{S_{Pillar} L}{A}. \quad (2.4)$$

2.2.5.4 Nanoindentation data

To ensure the validity of the micro-pillar compression data, a set of experiments is proposed to reveal if the nanoindenter data recording is a source of errors. To do so, a set of experiments is proposed on fused silica, a material widely used for nanoindentation calibration. The first set is carried out with a Berkovich tip, where 10 indents are inserted with the load control method, with a peak load of 10 mN. The depth measured at the peak load is then set as the depth target for a second batch of 10 indents inserted with the displacement control method. This way, it is possible to crosscheck the dataset acquired

from both methods. A second set of experiments is then carried out with the flat punch tip, following the same methodology. This whole procedure will determine if the nanoindenter is performing correctly regarding the load and displacement parameters.

-Berkovich tip

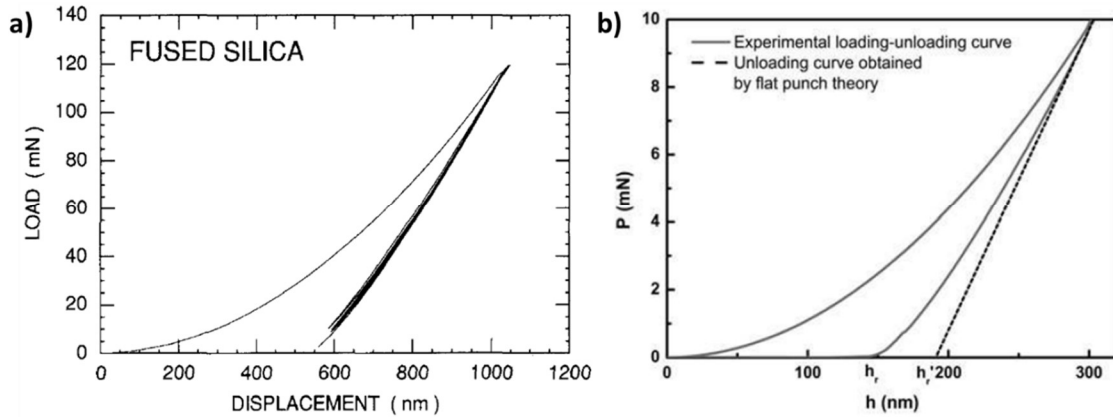


Figure 2.18: Literature data on nanoindentation loading cycles acquired with a Berkovich tip on fused silica with **a-** load vs. displacement with 120 mN peak load from Oliver and Pharr, and **b-** load vs. displacement with 120 mN peak load from Guillonneau *et al.*

The literature contains examples of loading cycles on fused silica with a Berkovich tip, with data from a study from Oliver and Pharr, and a detailed loading cycle up to 10mN from Guillonneau *et al.* (Fig. 2.18b) [106], [107]. The data obtained for this study with the Berkovich tip in load control, presented in Fig. 2.19 are matching data from the literature data from Fig. 2.18. This is a clear indicator that the machine records appropriately the load and the displacement.

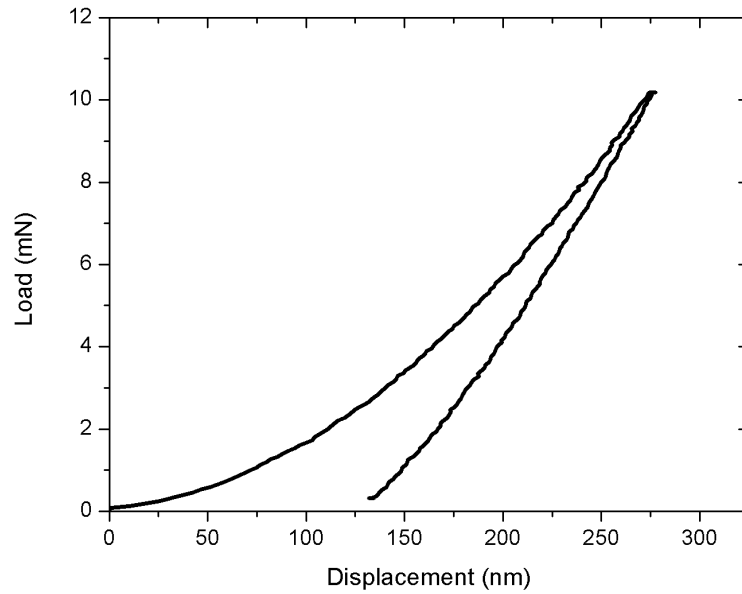


Figure 2.19: Load controlled loading cycle on fused silica with a Berkovich tip and a 10 mN peak load from the *Nanoindenter XP*

From the batch of indents generated from the load control method, such as the loading cycle presented in Fig. 2.19, a maximum depth was identified at 280 nm, and was set as the depth target for the next batch with the displacement control method. In Fig. 2.20 is presented a comparison between a loading cycle from the load control method and one from the displacement control method.

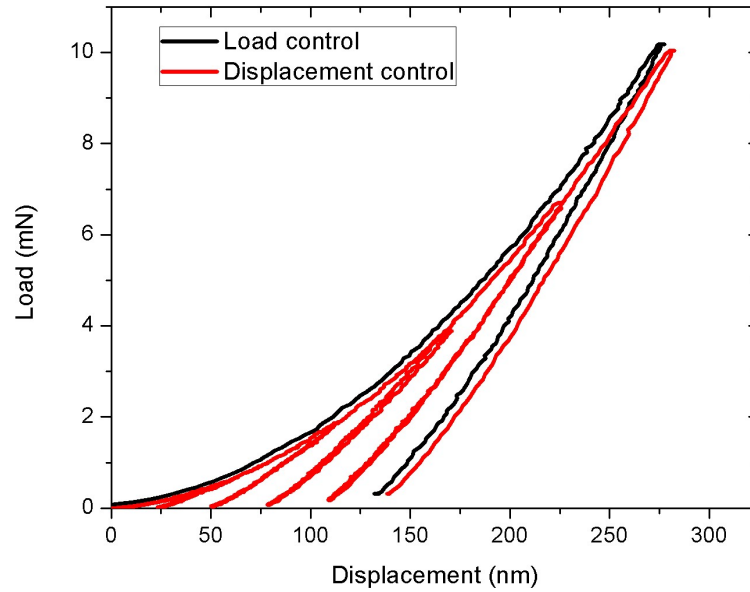


Figure 2.20: indentation loading cycle with the Berkovich tip, from the load control method (black curve) and from the displacement control method (red curve)

The displacement-controlled loading cycle, in red in Fig. 2.20, was completed in this case with 5 incremental loading cycles, method useful to exploit multiple unloading curves from a single experiment, with no data variation from a single loading cycle. The comparison of the curves suggests there is a slight shift in displacement between the two methods, although by very small amount, which is not reflected by the summary Table 6.

Table 6: Summary of the data recorded from indentations with the Berkovich tip

<u>Berkovich</u>	Load control	Displacement control
Average max. load	10.15 mN (min : 10.06 – max: 10,18)	10.34 mN (min : 9.2 – max: 11)
Average max. depth	279 nm (min : 274.5 – max: 294)	280 nm (min : 272 – max: 295)

-Flat punch tip

This method is now transposed to a flat punch tip, the same used for micro-pillar compression. In a general manner, the load displacement-controlled loading cycles are very consistent. However, two observations are made from the comparison between the load-controlled and displacement-controlled results, where on a first hand, some loading cycles perfectly match between the two methods used as shown in Fig. 2.21.

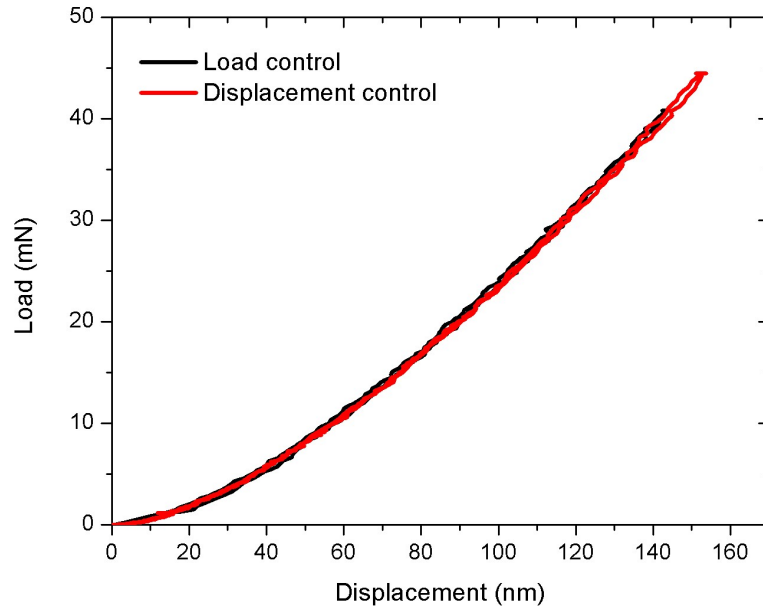


Figure 2.21: indentation loading cycle with a flat punch tip

On another hand, the displacement-controlled loading cycle can exhibit an over-estimation of the displacement, where the maximum shift recorded is 20 nm, as shown with an example in Fig. 2.22. Overall, various values of displacement over-estimation occur, all between 0 and 20 nm. It is possible to correct this offset from the dataset, at which point, the two loading cycles from load control and displacement control perfectly superpose.

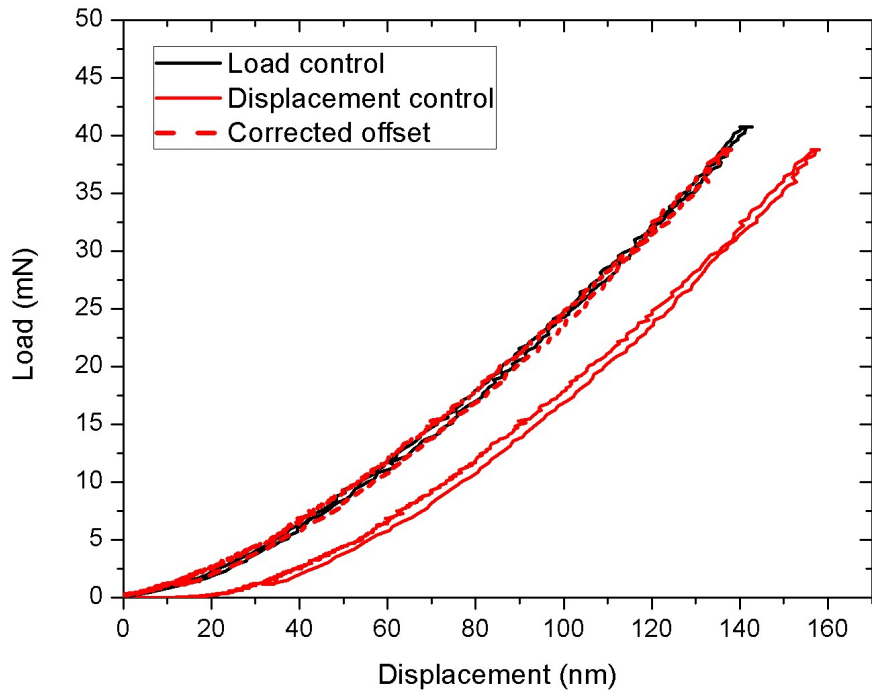


Figure 2.22: loading cycles from both methods, showing a displacement over-estimation for the displacement control method

The data from maximum depths and maximum loads attained for both methods re summarized in the Table 7, which shows the displacement over-estimation is clearly impacting the data.

Table 7: summary of the data recorded from indentations with the flat punch tip

<u>Flat Punch</u>	Load control	Displacement control
Average max. load	40.7 mN (min : 40.5 –max: 41)	42 mN (min : 36 – max: 47)
Average max. depth	142 nm (min : 132 – max: 158)	156 nm (min : 152 – max: 163)

After micro-pillar compression, datasets will be corrected by the Sneddon correction and for the nanoindenter displacement over-estimation.

2.3 Summary

The experimental techniques presented in this chapter assess the multi-scale approach suggested in Chapter 1, necessary to study a nanostructured alloy such as the p-type half-Heusler $\text{Hf}_{0.44}\text{Zr}_{0.44}\text{Ti}_{0.12}\text{CoSb}_{0.8}\text{Sn}_{0.2}$.

At first the alloy will be studied for its metallurgical aspects, to characterize its crystallographic structure, chemical composition, and grain size.

Then mechanical testing will be conducted with bulk experiment at first to assess the macroscopic behavior of the alloy under compression solicitation. This will generate useful engineering data, as well as give a first evaluation of the plastic behavior of this material, especially with the Paterson experiment.

At the meso-scale, the crack insertion via indentation toughness method will serve an assessment of both fracture mechanisms and plasticity in the crack path vicinity. To do so, 3D-EBSD technique will be applied to a volume containing a whole crack to study its path in relation with the crystallographic environment, and a TEM lamella will be extracted from the crack tip to study dislocation activity.

At the micro-scale, micro-pillar milled-out by FIB will be tested in compression by nanoindentation technique. Compression testing on a reduced volume will help determine eventual local plasticity events and provide a better understanding of how the

microstructure relates to the deformation mechanisms. In addition, it provides a complementary set of data and observations to compare with the upper-scale experiments.

Chapter 3 : Results and discussion

3.1 Metallurgical analysis of $\text{Hf}_{0.44}\text{Zr}_{0.44}\text{Ti}_{0.12}\text{CoSb}_{0.8}\text{Sn}_{0.2}$

3.1.1 Crystalline structure and composition

3.1.1.1 X-Ray Analysis

Analysis using X-ray diffraction is used to determine the phase in presence. The intensity peaks from the scan are a match with the half-Heusler phase NiSnZr [79] in the f-43m space group symmetry. The intensity peaks are sharp and defined, no extra peaks were detected within instrument resolution, indicating the purity of the phase overall the pellet, in addition it compares with data published on this material [37].

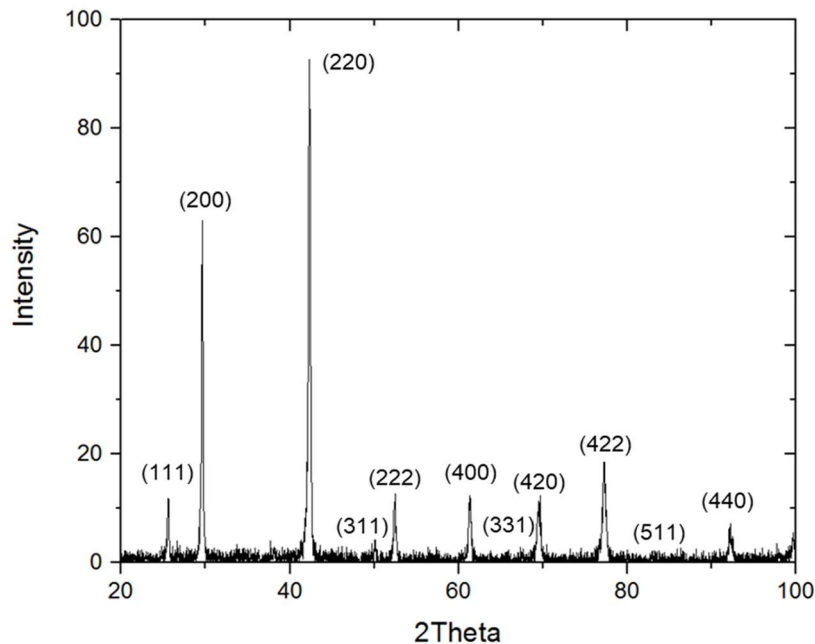


Figure 3.1: X-ray analysis confirming the half-Heusler phase presence

3.1.1.2 EDS Analysis

The alloy composition, $\text{Hf}_{0.44}\text{Zr}_{0.44}\text{Ti}_{0.12}\text{CoSb}_{0.8}\text{Sn}_{0.2}$ is confirmed by EDS analysis. Rare inclusions of pure Hf were spotted at random location and in random size, as reported in Fig. 3.2.

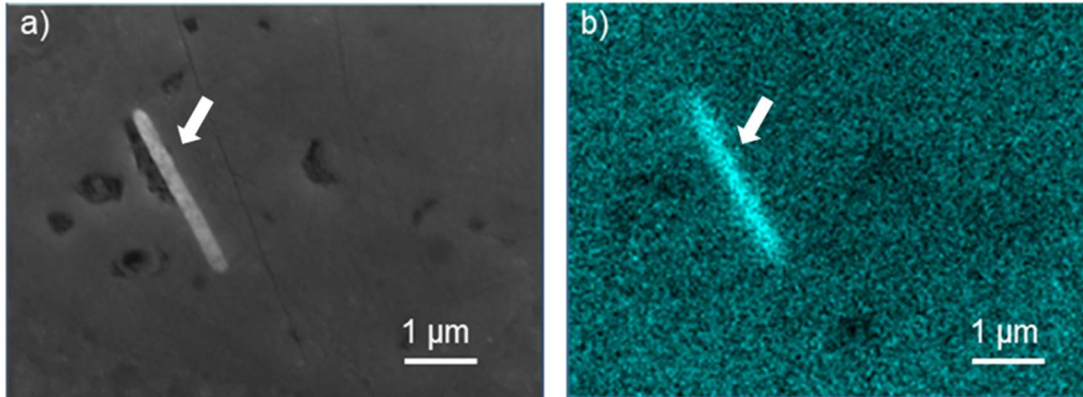


Figure 3.2: **a-** SEM observation of the surface in backscattered electron mode **b-** Hf map from EDS scan highlighting an area of high Hf concentration

3.1.2 Microstructure

3.1.2.1 SEM Observations

Observations by SEM on a Half-Heusler surface suggests at first a multi-modal microstructure. Large grains are spotted, with a size of the micrometer order in a range from $1\mu\text{m}$ to $10\mu\text{m}$. These large grains are surrounded by smaller grains non-discernible on a SEM picture as in Fig. 3.3. This suggests local observation is required to image the smaller grains. Then, an EBSD analysis conducted at an adapted pixel size will link the observations at each scale, in addition to TEM.

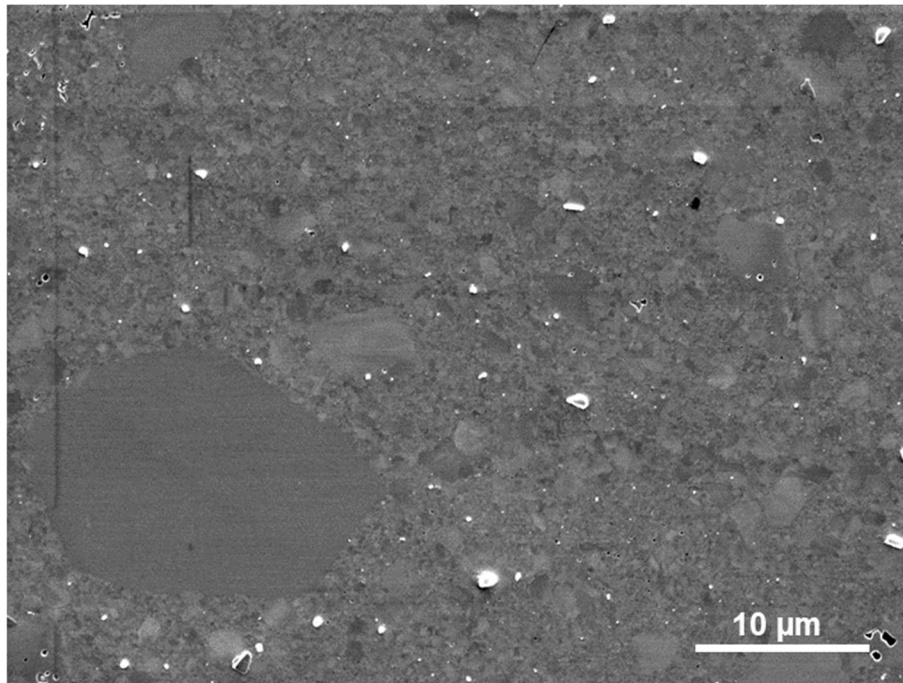


Figure 3.3: SEM observation on the surface, revealing only large micrometric grains

3.1.2.2 STEM and TEM Observations

The STEM and TEM observations complement the SEM observation by accessing small grain observations. The intercept method on these images (Fig 3.4) determines the grain size of the nanostructure: mean size 110nm, ranging from 70nm to 140nm.

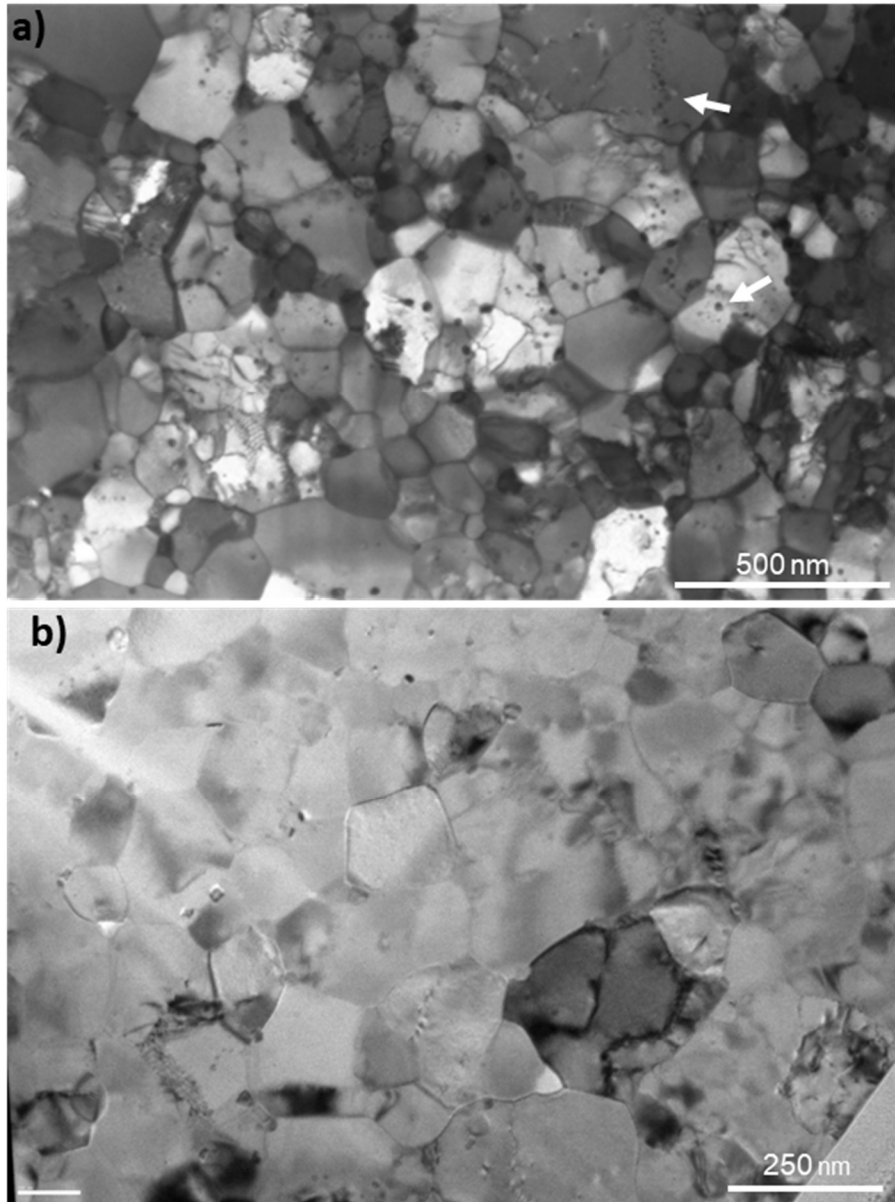


Figure 3.4: **a**-STEM image showing microstructure and presence of small precipitates within the grains (arrows). **b**- TEM observation showing the nanostructure

In addition, very small precipitates, 10nm to 20nm diameter, showing Moiré fringes, are spotted within the grains (Fig 3.5a) and at grain boundaries (Fig. 3.5b). The intra-granular precipitates are likely to have formed along former grain boundaries as some of them are disposed along a distinct path.

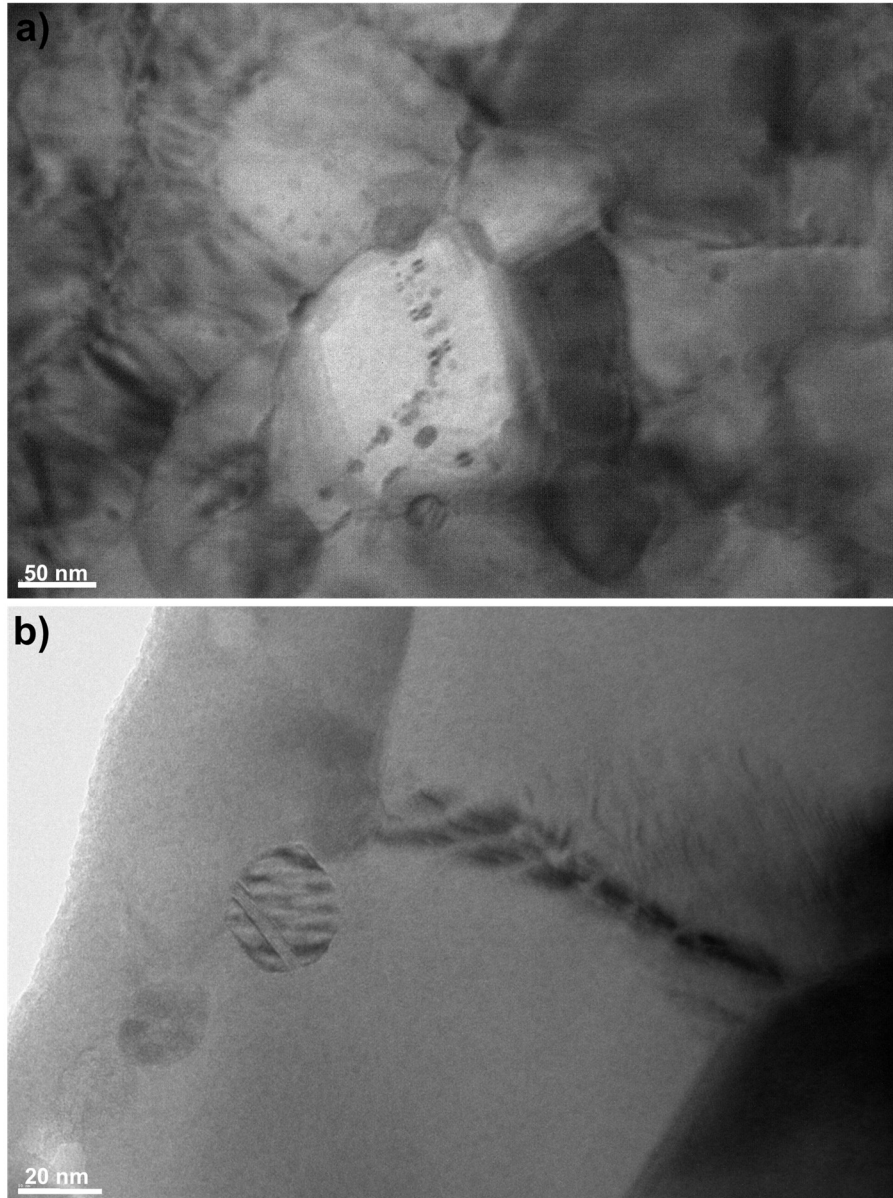


Figure 3.5: TEM observation showing small precipitates: **a-** String of precipitates within a grain, **b-** Individual precipitates at a grain boundary

Finally, the TEM observations show the presence of dislocations networks within grains as indicated by a white arrow in Fig. 3.6.

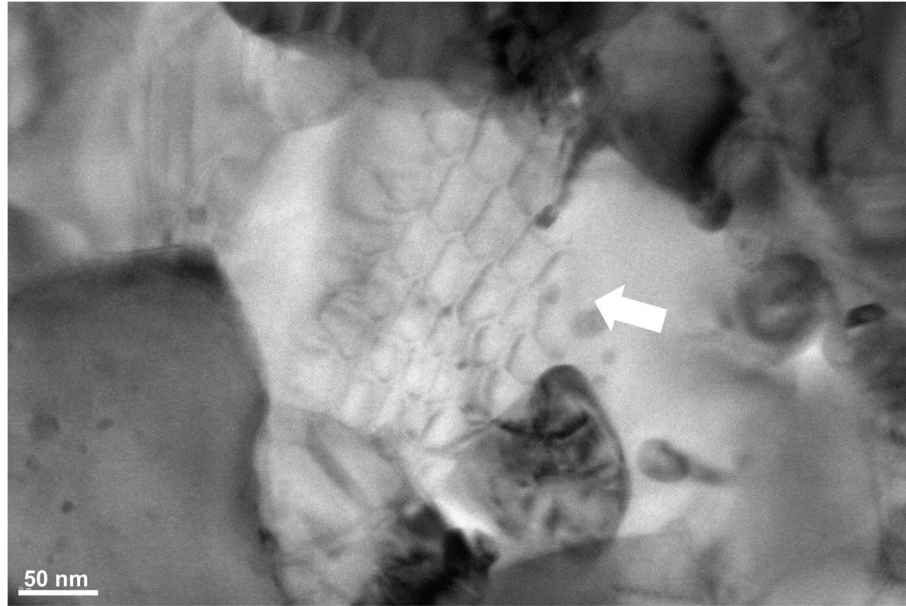


Figure 3.6: dislocations network observed by TEM

3.1.2.3 EBSD analysis

An EBSD map with 10nm pixel size confirms and complements the information gathered from SEM and TEM observations, showing a grain size distribution containing both nanostructured and micrometric grains. The EBSD map displays a random grain orientation, suggesting that the fabrication process does not induce any string texture. Although the microstructure could be interpreted as bimodal, a grain size distribution histogram from EBSD scan may suggest another trend in the grain size distribution.

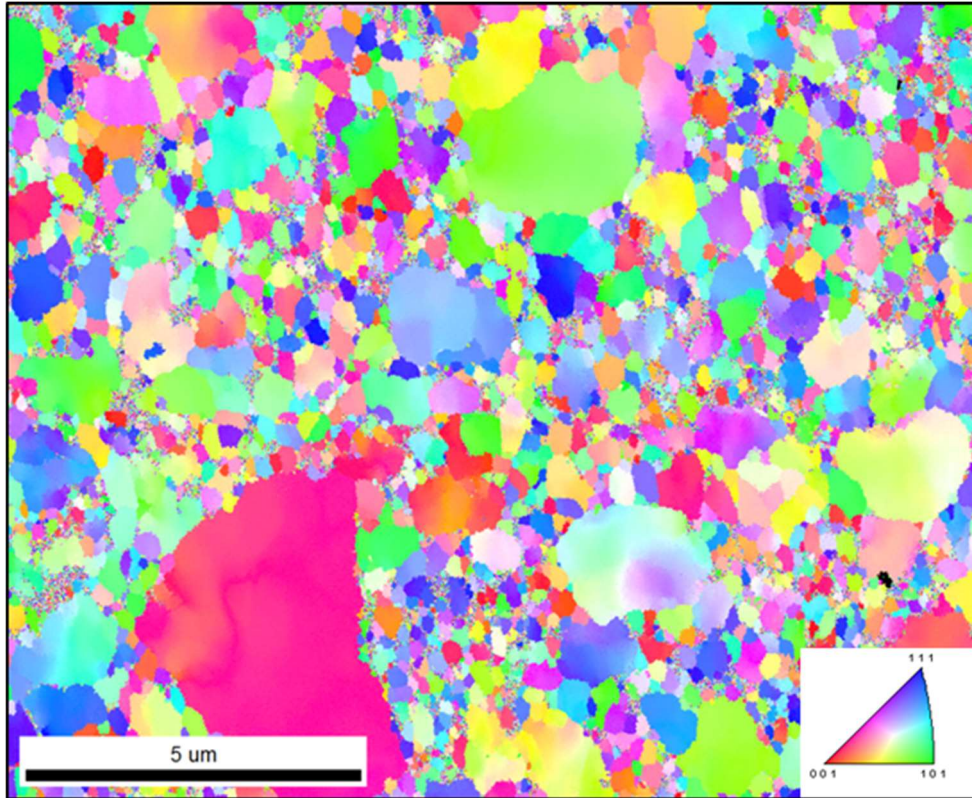


Figure 3.7: EBSD map with a 20 nm step size

The processed samples are a circular pellet of 12.7 cm diameter, where the grain size distribution is analyzed with three large EBSD maps collected successively from the center to the edge of the sample in Fig. 3.8. As the area analyzed approaches the center, the grain size distribution contains larger grains as the largest grain size recorded tends to double from one map to another. This suggests the SPS processing do not provide a homogeneous grain size distribution from the center to the edge of the sample in this case, perhaps due to a thermal gradient while processing.

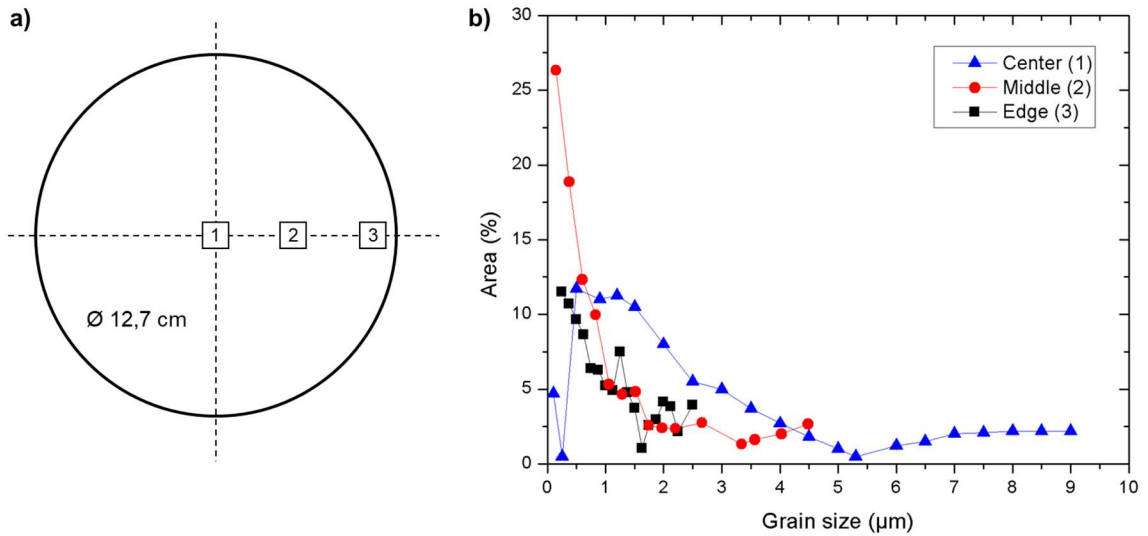


Figure 3.8: **a**-location of the EBSD maps for grain size distribution analysis **b**-grain size distribution for each EBSD map

3.2 Classical compression at ambient atmosphere

A set of three classical compression tests at room pressure and room temperature were conducted. The specimen reached the following stress values: 1.75 GPa, 2.48 GPa and 2.53 GPa, all tended toward a brittle failure. The stress-strain curve of the last sample is displayed in Fig. 3.9a. The stress-strain data reported before the elastic regime is a testing artifact, as the contact between the fixtures and the sample is stabilizing. The stress strain curves show an elastic regime highlighted with the red dashed curve, associated to a strain of 0.23% after correction from the non-perfect contact between sample and fixtures, exhibiting an exclusive linear elastic behavior upon brittle failure.

The sample failure reported is extremely brittle as the elastic energy release is instantaneous, leaving only dust and few chunks of the specimen in the testing area. Fracture surface observations confirm the brittle trend as the several crack paths in Fig.

3.9b is either progressing along the grain boundary or across the larger grains with almost no variation in the direction of propagation.

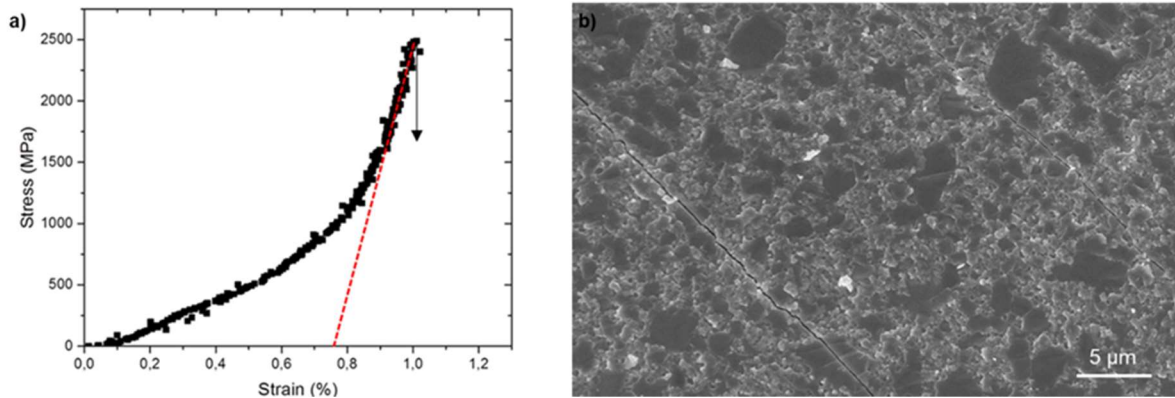


Figure 3.9: **a**-Stress-strain curve of compression test displaying brittle behavior. **b**-Fracture surface showing crack propagation in the microstructure

The result of these mechanical tests suggests the deformation under compression in regular conditions cannot trigger plasticity mechanisms. This means additional constraints to crack propagations are necessary, and the Paterson machine is one of the appropriate techniques.

3.3 Compression under confining pressure

The stress-strain curves reported in Fig. 3.10 are exclusively displaying linear elastic regime, as the failure of each specimen occurs without plastic activity. Increasing the hydrostatic pressure from 300 MPa to 350 MPa, or raising the temperature to 400°C leads to the same behavior with failure stress varying from 2.6 GPa to 3.8 GPa. The machine stiffness of the Paterson is sensitive to pressure and temperature conditions, thus the slope variation from one test to another cannot be accounted for the sample behavior.

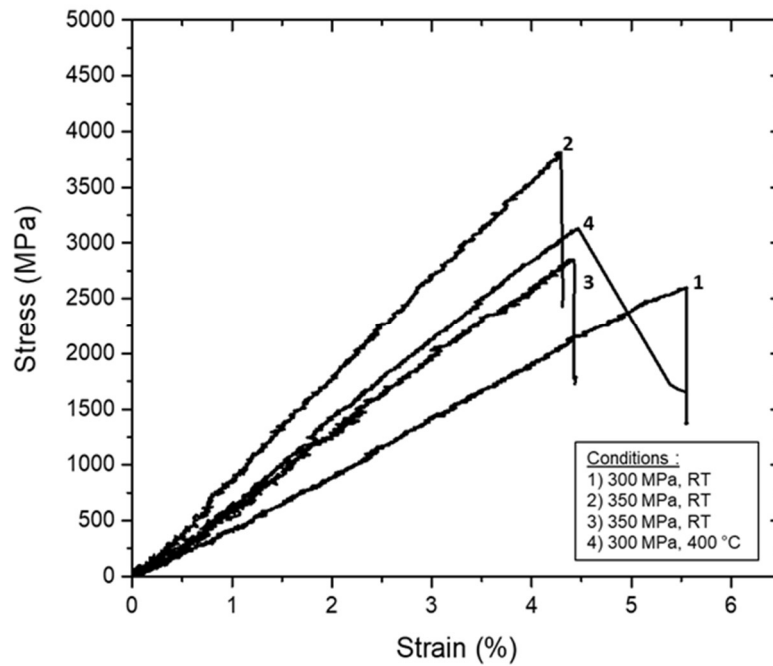


Figure 3.10: Stress strain curves for various temperature and pressure conditions

Nevertheless, these data clearly show a linear elastic regime without yield, and a brittle failure. Indeed, the remaining parts of compressed samples consists of a combination of dust-like material and few chunks, contained in the Al jacket after the test. The brittleness is confirmed by SEM observation on a piece of sample recovered from the test.

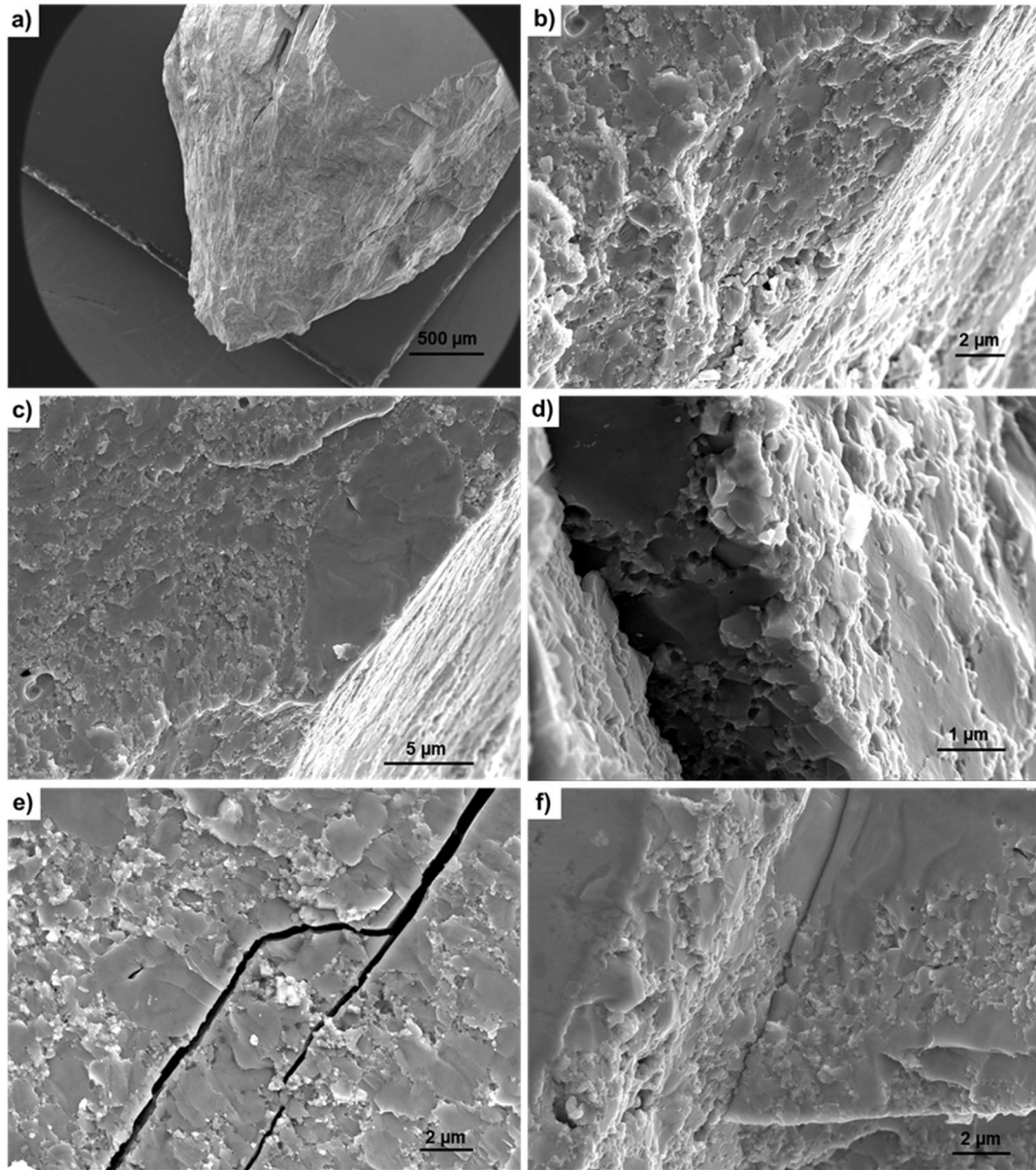


Figure 3.11: **a**-main debris recovered from a test **b**- fracture surface showing textured surface **c**- fracture surface showing a large grain where two fracture plane meet **d**- combination of large grain cleaved and nanostructured grains decohesioned **e**-crack branching within a grain **f**-crack propagation from a large grain to a grain boundary.

Indeed the fracture surfaces are displayed through many examples in Fig. 3.11. Locally, complex crack propagation occurs with an example of branching triggered within a micrometric grain (Fig. 3.11e). It is noticeable the cracks are propagating differently regarding the microstructural environment. In Fig. 3.11, the observations show that very

large distance can be covered by the crack, especially within the larger grains where the crack keeps a straight path (Fig. 3.11c,f). When it reaches the opposite grain boundary, the crack follows a zig-zagging path, between the smaller grains along the grain boundary.

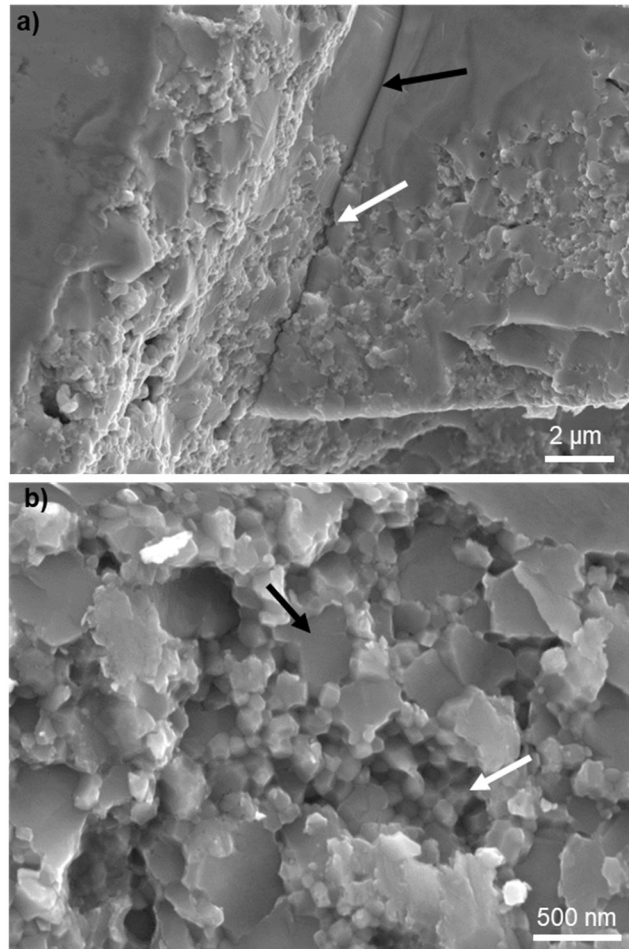


Figure 3.12: Fracture surface displaying nanostructured matrix decohesion and larger grain cleaved.

This phenomenon is illustrated in Fig 3.12, causes small grains decohesion (white arrows) while larger embedded grains are cleaved (black arrows), creating a complex surface topography. The crack propagation occurs as follows: if a propagating crack encounters a grain larger than its neighbors, it will preferentially cross this one until it reaches the opposite grain boundary through intra-granular cracking where at this stage,

the crack is likely to evolve again in the nanostructured matrix, where its progression will follow an inter-granular path along grain boundaries of the smaller grains.

The SEM observations on compression fracture surfaces show very large area of crack propagation, following a straight path, suggesting little to no control on this phenomenon is possible with this microstructure. In addition, since no plasticity is reported on the stress-strain curves of these tests, local observations are necessary to study the crack tip area for possible dislocation activity.

3.4 Mesoscale analysis of controlled crack insertion

After nanoindentation, the radial cracks that appeared around the indents are subject to three kinds of observation: 1) Surface observation of indented region (SEM and EBSD), 2) 3D-EBSD tomographic reconstruction of an extracted volume containing one of the cracks and 3) TEM observations on extracted foil at crack tip.

3.4.1 Surface observations

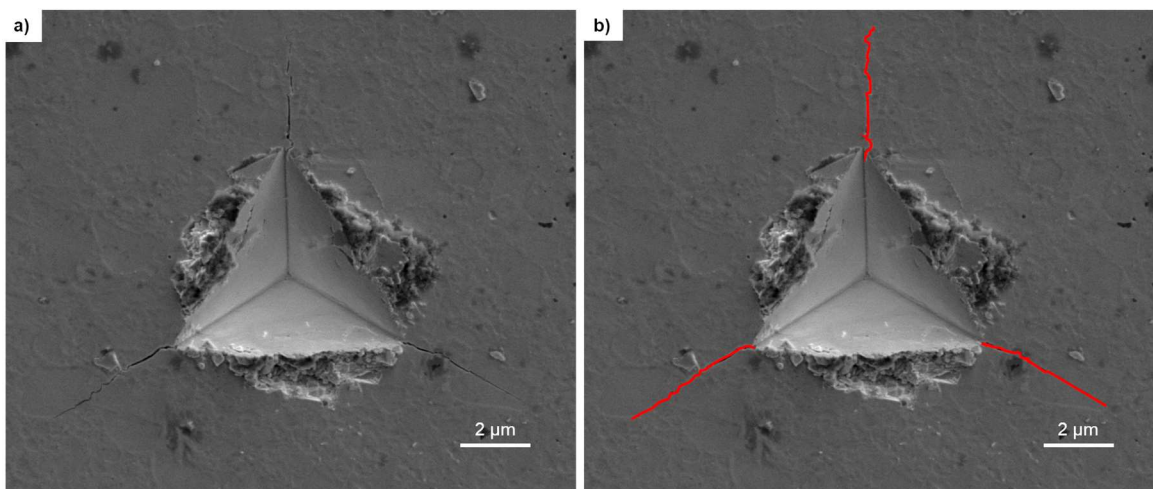


Figure 3.13 : 200 mN indent obtained with a cube corner tip displaying three radial cracks

A simple SEM observation in Fig. 3.13 of the radial cracks show their paths evolving as both inter- and intra-granular as highlighted with the red lines. The crack path depends on the microstructural environment encountered as it evolved in the medium, confirming the trend observed on compression fracture surfaces.

As mentioned in Chapter 2, section 2.2.4.2, indents with various loads were made on the surface. In the indentation grid displayed Fig. 2.14a, the lowest load applied is 5 gf, where cracks propagated from the indent tips. It is probable the threshold load for crack initiation is lower than this value. An estimation of the fracture toughness of this material was attempted on 5 gf load indents, where for an accurate estimation this should be done on an indent generated by the threshold load [102]. Within this limitation, the value of K_{IC} for this material is estimated as $1.48 \text{ MPa}\cdot\text{m}^{1/2} < K_{IC} < 2.6 \text{ MPa}\cdot\text{m}^{1/2}$, with an average value of $1.92 \text{ MPa}\cdot\text{m}^{1/2}$, according to the relation $K_{IC} = \alpha \left(\frac{E}{H}\right)^{1/2} \left(\frac{F}{L^{3/2}}\right)$, where E is the elastic modulus, H the hardness, F the peak indentation load, L the crack length from the center of the indent to the crack tip, and α an empirical constant depending on the geometry of the indenter, taken as 0.04 for a cube corner tip [102].

EBSD observation on an indentation (Fig. 3.14) confirms the crack propagation trend reported in previous section and highlights its complexity. By comparing and combining index quality (IQ) and inverse pole figure (IPF) map, the crack path between the grains of the nanostructured matrix and within a large grain can be observed, as highlighted by red lines. It seems the crack is deflected by sub-structures in the large grain (probably of the same type as the dislocation networks observed in Fig. 3.6), but still propagates along the same main direction. This observation suggests the crystalline

orientation may not affect the direction of the crack propagation. Instead, local crack deflection shows sensitivity to the grain boundary and grain sub-structures.

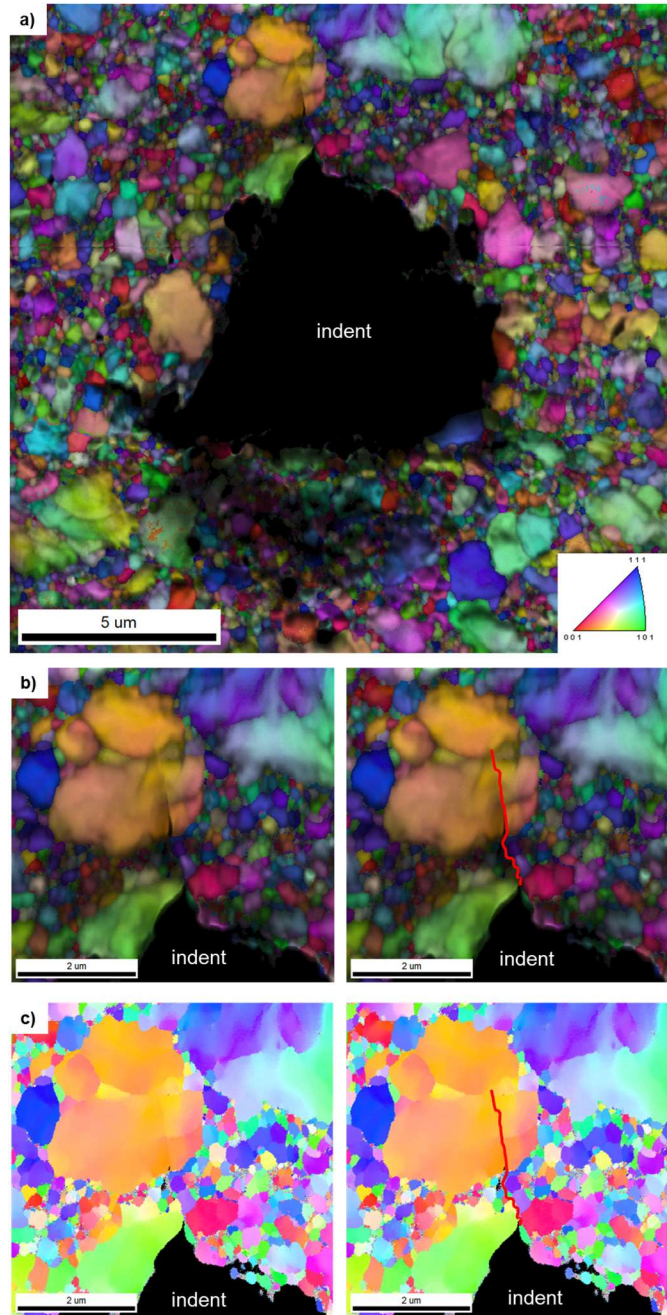


Figure 3.14: **a**-EBSD (IQ+IPF) map with 20nm pixel size on an indent **b**-magnified area displayed with superposition of IQ and IPF (left) map with crack highlighted in red (right) **c**-magnified area displayed with an IQ map (left) with highlighted crack in red (right)

3.4.2 Tomographic reconstruction

Another indent is subject to crack observation (Fig. 3.15), via the 3D-EBSD tomographic reconstruction. Displayed in Fig. 3.16, the selected volume is $5.76 \times 3.46 \times 4.41 \mu\text{m}^3$ and contains a radial crack portion, as well as the information on grains orientation (from EBSD). The EBSD resolution together with the degradation of EBSD signal by FIB milling does not allow to properly index the individual crystallographic orientations in the smallest grains of the nanostructured matrix: only the larger grains are properly observed in the rendered volume.

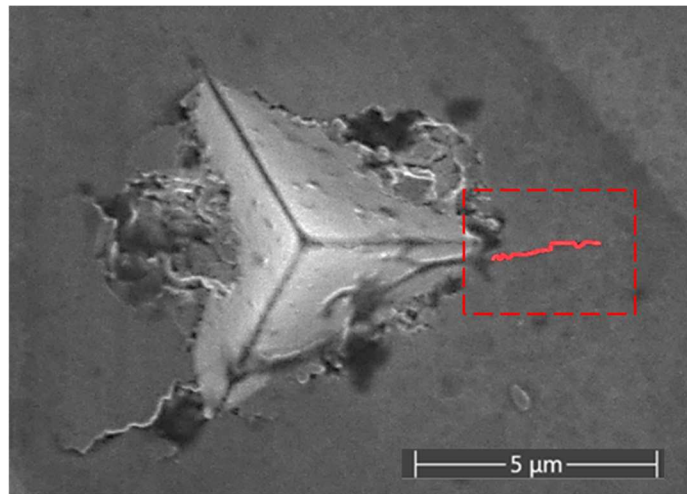


Figure 3.15: Indentation and the selected crack highlighted in red. An estimation of the initial volume extracted is represented by the red dashed line

The black voxels represent voids. From above (Fig. 3.16a), the indent edge is identifiable with its triangular shape composed of black voxels. In addition, the crack path can be as well identified, starting at the indent edge. From below (Fig. 3.16b), the black voxels show portion of the crack as it progresses from the indent to deeper regions, where it reappears at the bottom of the volume, through a large grain.

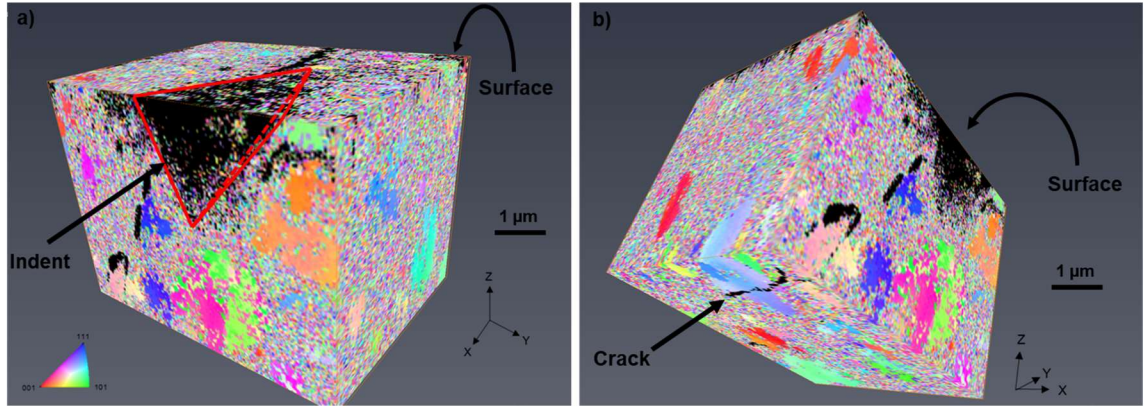


Figure 3.16: **a**-Top view of the reconstructed volume facing the indent **b**-View from beneath the volume where the crack reappears through a grain **c**-Highlighted crack around a large blue grain **d**-Highlighted crack fracturing two grains in blue and pink

The volume is observed in transparency mode in Fig. 3.17, showing the indent and crack highlighted with dark blue voxels. In addition, EBSD maps from the original stack can be displayed to study selected slices. Analysis of this volume confirms the inter-granular path as the crack is contouring the blue grain in Fig. 3.17a (arrow), as well as the intra granular cracking as the crack is crossing two grains in Fig. 3.17b (arrows).

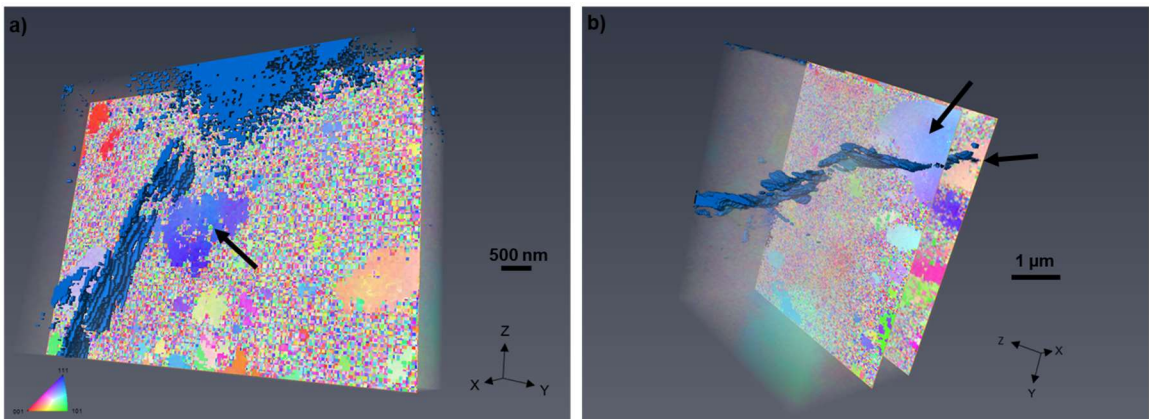


Figure 3.17: **a**-Highlighted crack around a large blue grain **b**-Highlighted crack fracturing two grains in blue and pink

The complete scanned volume is displayed in transparency with the highlighted voxels in Fig. 3.18.

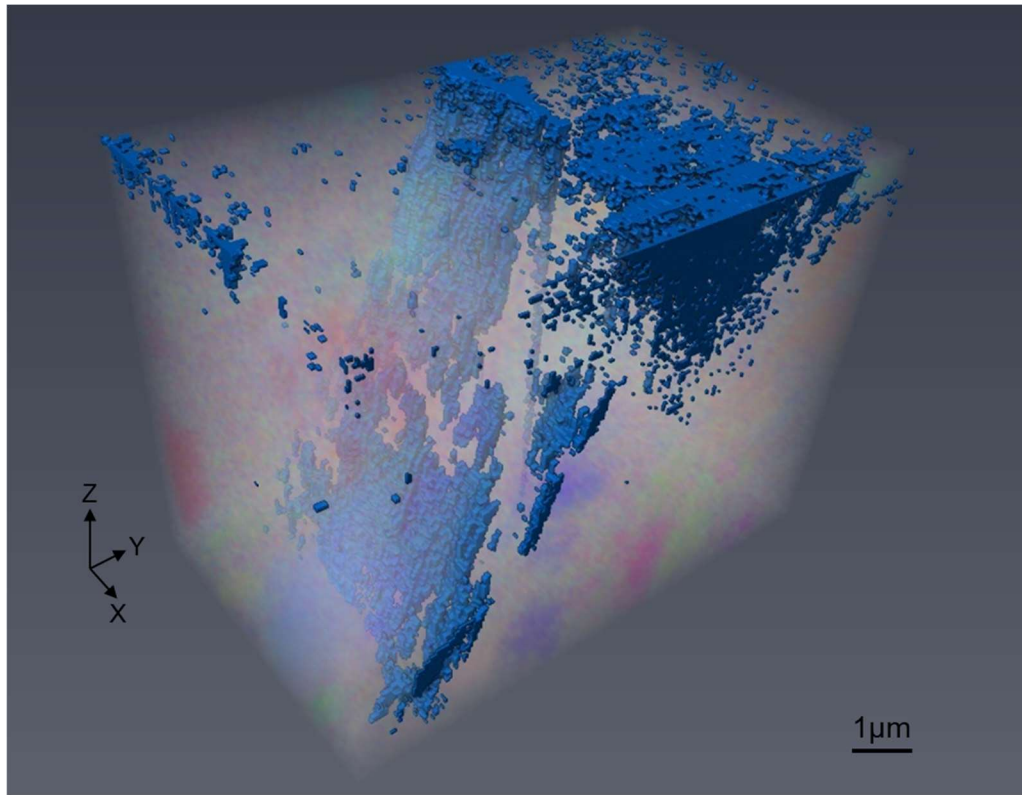


Figure 3.18: volume observed in transparency with the unindexed pixels highlighted in blue

3.4.3 TEM observation

TEM lamellae were extracted as close as possible to the tip of radial cracks, perpendicular to their path, shown in Fig. 3.19. A SEM observation on the surface with the crack highlighted in red (Fig. 3.20a and Fig. 3.20b) show the crack is either contouring or crossing grains. Preliminary STEM observation on the thin foil shows the crack highlighted in red (Fig. 3.20c), making the distinction with the FIB curtaining effect. (This phenomenon occurs when the ions channel where the crack was initially opened because of the local topography, causing an extra straight and plumb thinning).

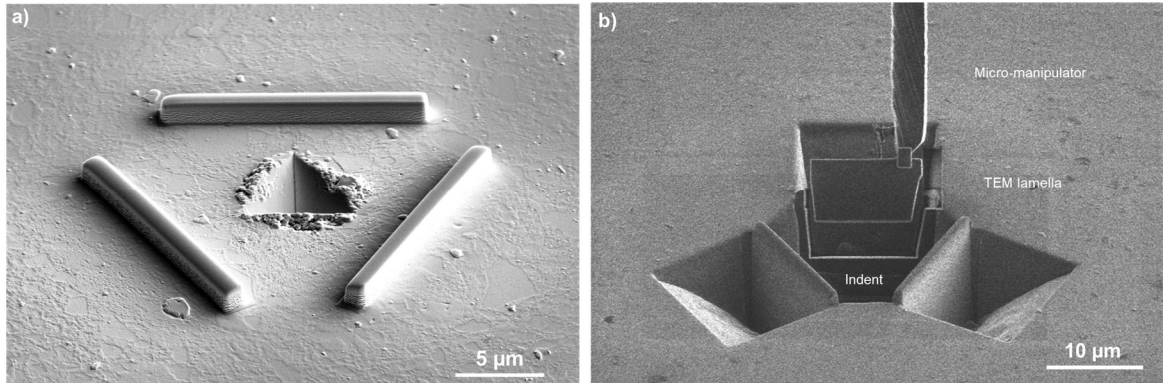


Figure 3.19: **a-** An indent with three Pt layer deposited at the crack tips prior to FIB milling **b-**TEM thin lamella extracted with the micro manipulator

Observations by TEM (Fig 3.21) show the crack path perpendicular to the surface follows exclusively inter-granular cracking, with examples of branching around few grains. The crack tip is located 2μm below the surface in a grain boundary. No dislocation activity can be observed in the crack path vicinity as well as in the grains in the crack tip area (Fig 3.21c). The exclusive inter-granular path in this case may be due to the absence of large grain on the crack path.

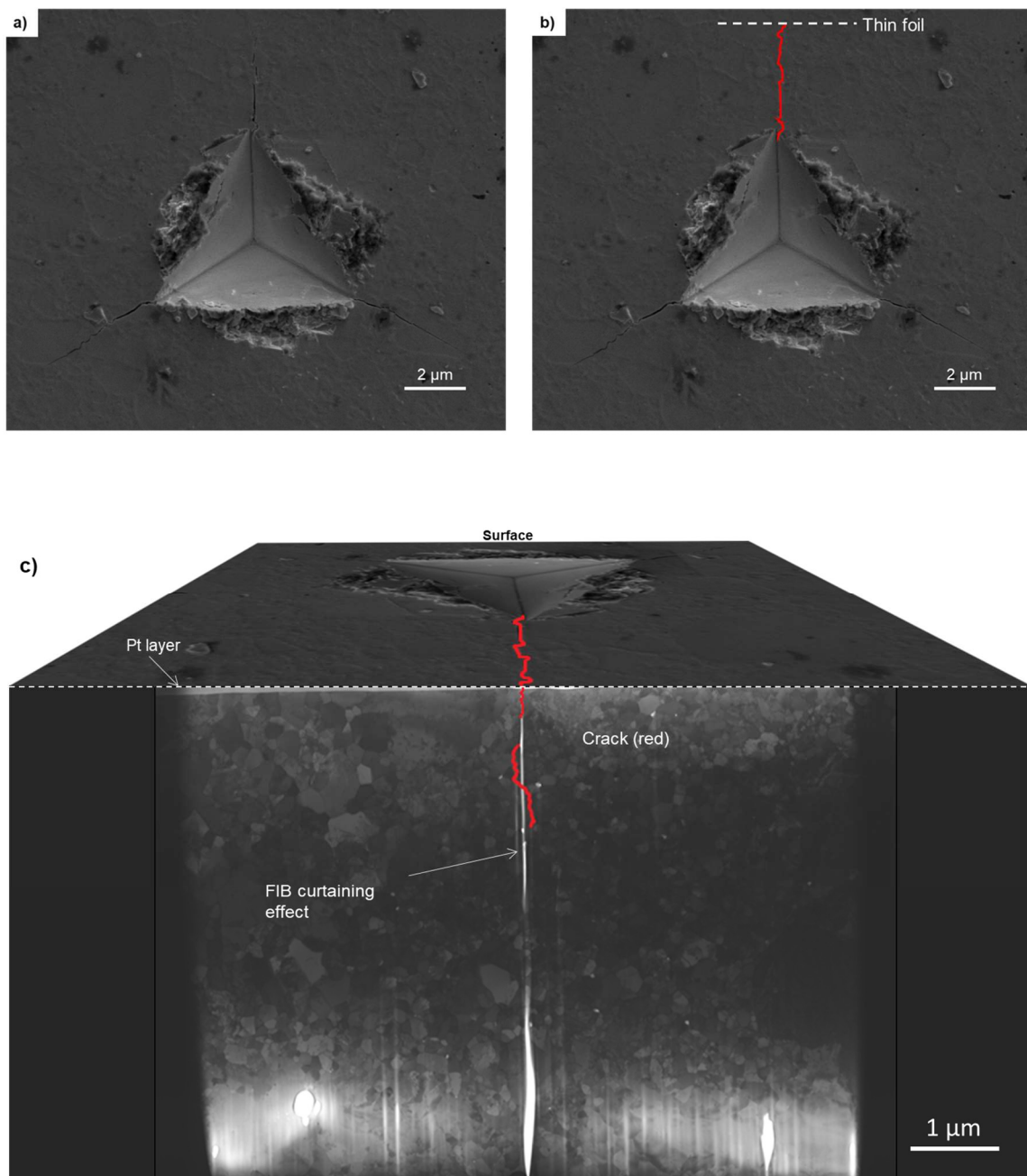


Figure 3.20: **a**-Indent with three radial cracks **b**-Red highlight of the crack and location of the TEM thin foil extraction area **c**-In-plane representation of the TEM foil extracted, as observed by STEM.

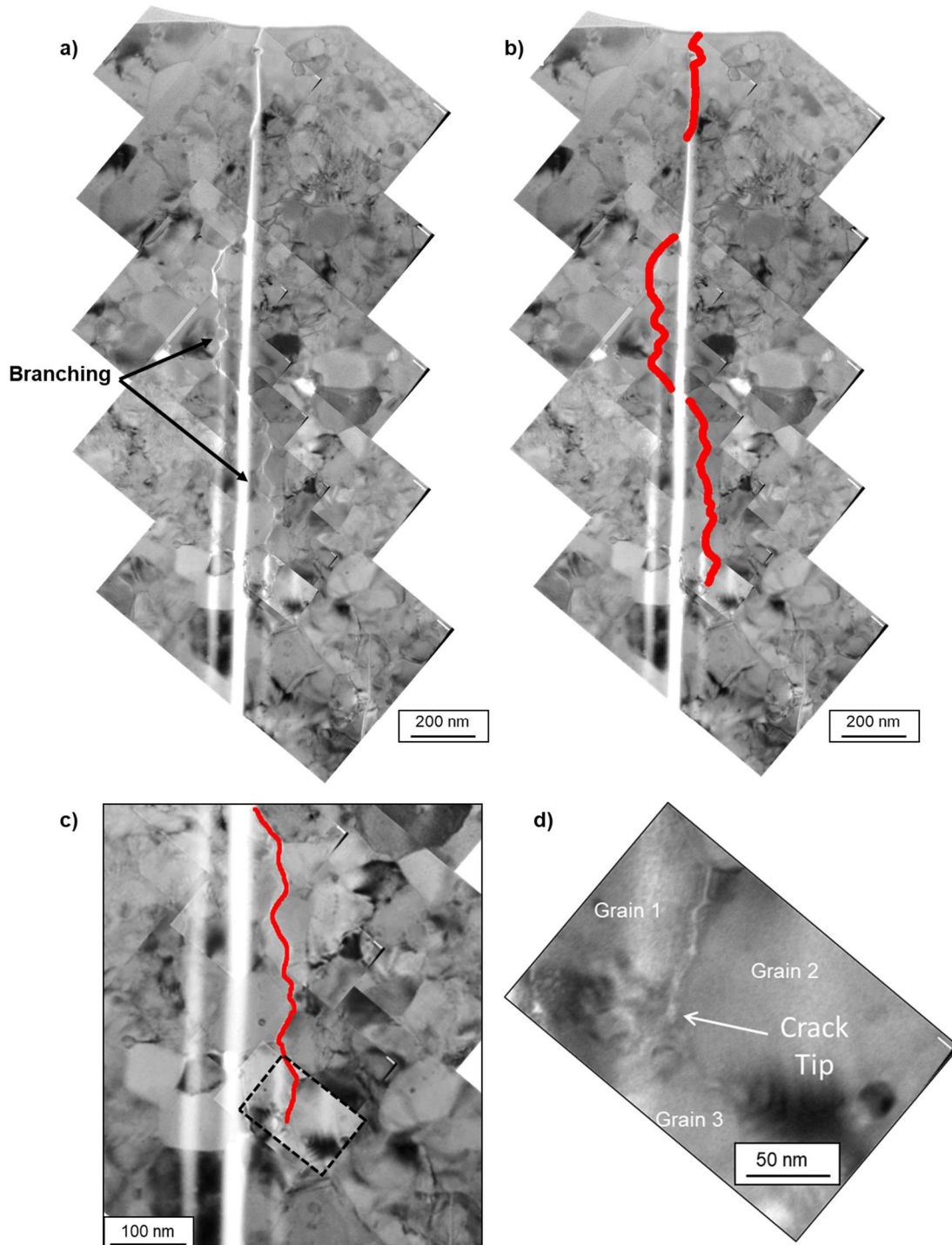


Figure 3.21: **a**-TEM observation on extracted thin foil showing in-depth crack propagation with example of branching **b**-Red highlight of the crack path **c**-Crack tip area magnification showing no dislocation activity **d**-crack tip located at a GB without dislocation activity in the three surrounding grains

3.5 Micropillar compression

3.5.1 Mechanical testing

A polycrystalline pillar before compression is displayed in Fig. 3.22, milled out by FIB with a square cross-section ($2 \times 2 \mu\text{m}^2$) and $6 \mu\text{m}$ height.

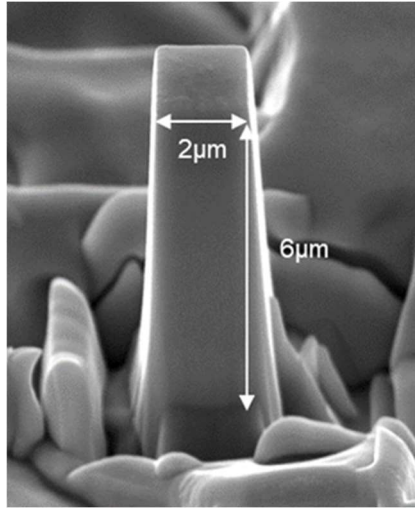


Figure 3.22: micropillar geometry

As mentioned in Chapter 2, the pillars were not damaged at first loading. Instead the procedure consists in incremental depth of penetration of the nanoindenter tip compressing the pillar, to have a chance to assess plasticity mechanisms before specimen failure. An example of this procedure is reported in Fig. 3.23 with stress-strain curves associated to depth of penetration ranging from 75nm to 200nm. The loading cycle causing the pillar failure displays a displacement of 196nm, and the slope remains identical to the previous loading cycles slopes, proof that the pillar did not sustain plastic damages during pre-compression. No sign of plasticity is shown by these stress-strain curves, including the last one leading to the brittle failure.

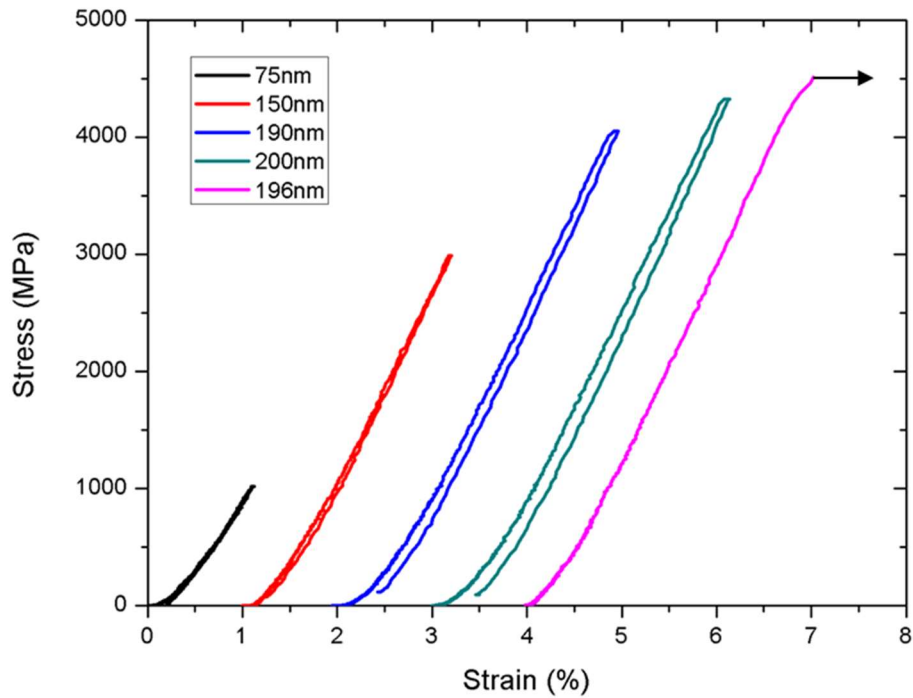


Figure 3.23: loading cycles on a micropillar with color-coded max depth, the strain is artificially shifted for display purpose

The final stress-strain curves for three pillars tested in compression are reported in Fig. 3.24, showing a deformation behavior following an elastic regime, until brittle failure. The pillars compression testing were conducted at speeds varying between $8.5 \text{ nm}\cdot\text{s}^{-1}$ and $25 \text{ nm}\cdot\text{s}^{-1}$, equivalent to strain rates of $1.4 \times 10^{-3} \text{ s}^{-1}$ and $4 \times 10^{-3} \text{ s}^{-1}$ for pillars with $6 \mu\text{m}$ height. These curves do not show sensitivity to the variation of the speed of compression. While some curvature of stress-strain curves can be observed right before sample failure, this phenomenon is due to the nanoindentation load control procedure instability while the specimen starts to fail and is not a sign of plasticity.

The stresses reached by each pillar are ranging from 3.1 GPa to 4.5 GPa which is consistent with the macroscopic tests under confining pressure. The data scattering on these stress-strain curves is comparable to the confining pressure dataset on bulk samples.

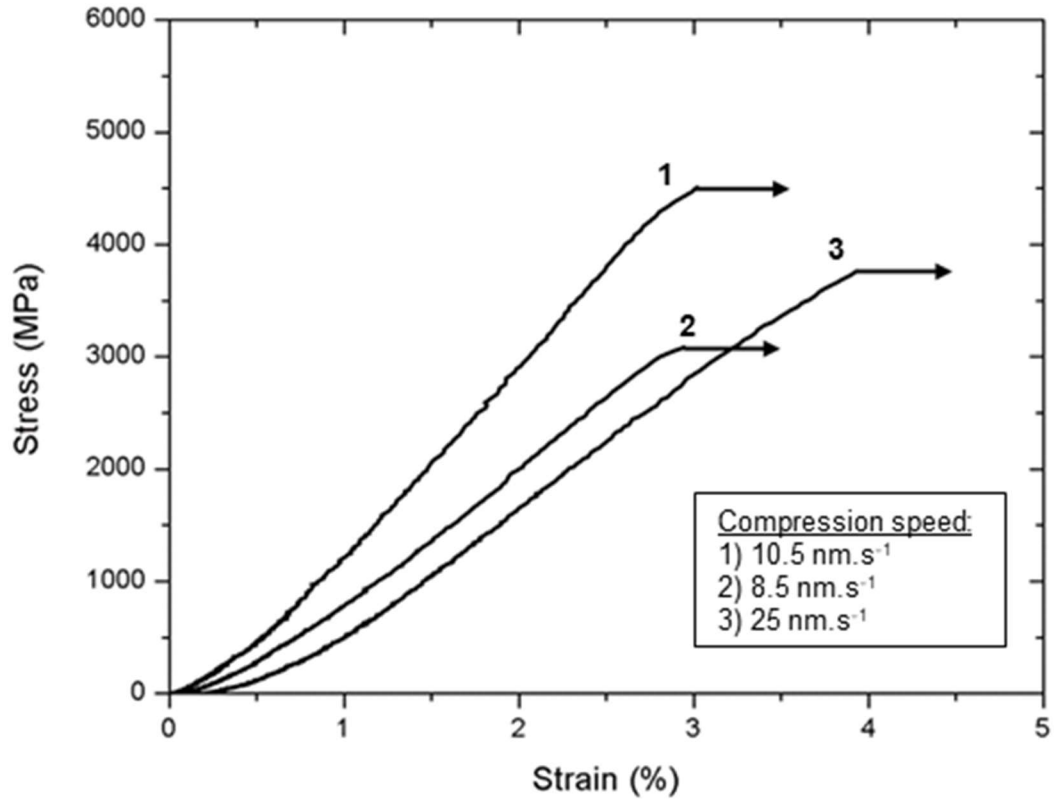


Figure 3.24: Stress-strain curve of micropillar compression

Such consistency may be due to a local grain size distribution that would favor early crack propagation, such as a large grain in a stress-concentration area. Indeed, the micropillars fracture surfaces presented in Fig. 3.25 show both inter- and intra-granular cracking. These observations can be easily compared to the confining pressure test fracture surfaces observations for their similarity (Fig. 3.11b-f).

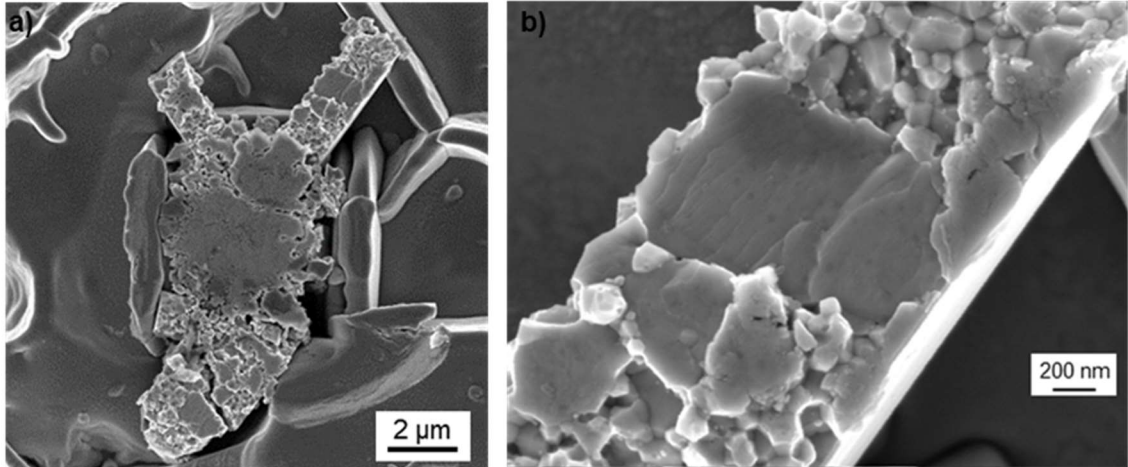


Figure 3.25: **a**-Pillar broken in several large segments **b**-Fracture surface showing both inter- and intragranular cracking

3.5.2 Corrections on micro-pillar data

As the micro-pillar compression was carried out with a flat punch tip, in displacement control mode, the observations gathered from nanoindentation data are considered for an additional correction on the micro-pillar data. The maximum displacement offset recorded is 20 nm, however the ratio of the depth measured and the real depth changes as the test progresses. As the micro-pillar compression loads are located around the 10 mN, the depth difference ratio at this load value was chosen to calculate the corrective coefficient, leading to an overestimation of a factor of 1.36. The corrected stress-strain curves are displays in Fig.8 and the new elastic modulus are presented in Table 8, for which the values are now for 281 GPa for pillar n°1, 196 GPa for pillar n°2 and 189 GPa for pillar n°3. The elastic modulus calculated for this material is 229 GPa.

Table 8: summary of the elastic moduli values

Pillar N°	E (GPa)	E_Sneddon (GPa)	E_final (GPa)
1	169 +/- 5	207 +/- 10	281 +/- 20
2	124 +/- 4	145 +/- 7	196 +/- 14
3	119 +/- 4	139 +/- 7	189 +/- 13

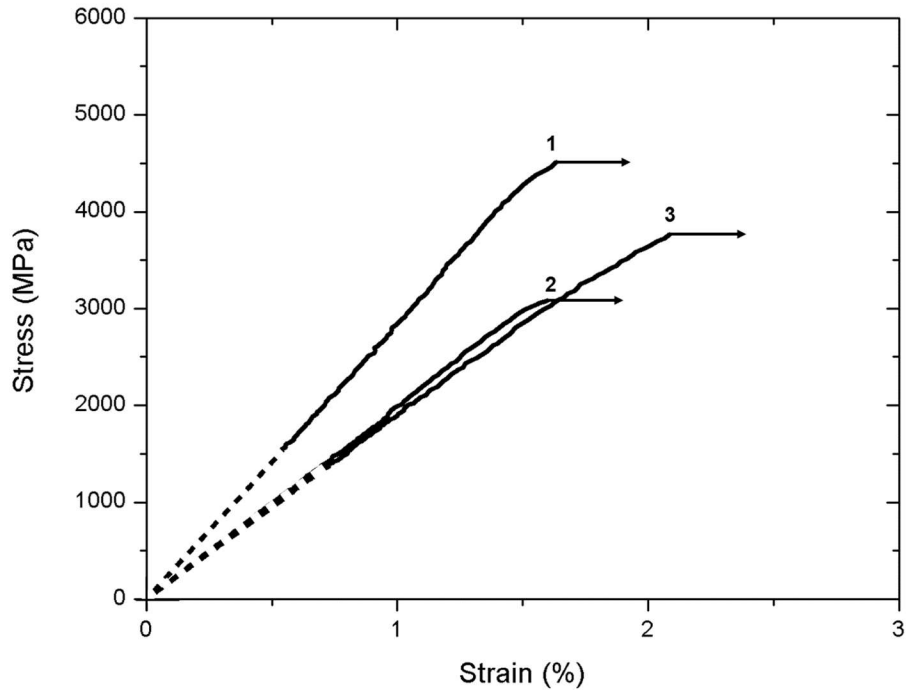


Figure 3.26: stress-strain data corrected for the linear curve foot, the Sneddon corrections and the nanoindenter displacement overestimation

3.5.3 Conclusions

There is an over estimation of the elastic modulus of pillar n°1, probably due to the correction for the nanoindenter data recording which considers the maximum displacement offset. Indeed, the true correction for one micro-pillar compression is anywhere between zero and the maximum correction pointed-out, which was applied in this case. For the case of pillar n°1, the Sneddon correction seems to be enough.

For the pillars n°2 and n°3, the elastic moduli values are still right under 200 GPa. There are several possibilities to account for. Prior study on the this half-Heusler material has demonstrated an anisotropy in the values of elastic modulus in function of the crystallographic orientation [36]. The values reported range between 208 GPa along the

<111> directions and 255 GPa along the <100> directions. This must be accounted for as there is a possibility for a large grain to fill the cross-sectional area of a micro-pillar, on a limited length. There is also the possibility of the presence of porosity inside the pillars, or in the pedestal volume, that would lead to lower fracture stresses as well as contribute to the scattering of both the stiffness and fracture stress values. Overall, the slope variation between pillars may be not real because of the non-predictable over-estimation of displacement. If the second data correction is not applied to pillar n°1, the elastic moduli for the three pillars are all within a reasonable range of 20 GPa, lower but closer to the material elastic modulus of 229 GPa than from the raw dataset.

3.5.4 Critical flaw size estimation

An approach to assess the damage mechanisms consists in evaluating the critical flaw size. Since the micro-pillar experiment is highly localized and concerning a closed volume, such estimation allows to check if the sizes of the defects that trigger failure of the specimen, are reasonable regarding the specimen size. Using the expression for fracture toughness $K_{IC} = \sigma \sqrt{\pi a}$, the critical flaw size (a) is estimated using the values of micro-pillar failure stresses for σ and the range of values of fracture toughness obtained via nanoindentation for K_{IC} . The values obtained range between 34 nm and 220 nm. These are realistic values, considering the size of the micro-pillars ($2 \times 2 \times 6 \mu\text{m}^3$) as well as the wide range of grain size, starting in the scale of only tens of nanometers and can be as large as the micron range. This analysis suggests that the fracture initiation scales with the microstructure or grain boundary porosity that could be present within the micro-pillars.

3.6 Summary

A multi-scale deformation analysis was conducted on the p-type Half-Heusler $\text{Hf}_{0.44}\text{Zr}_{0.44}\text{Ti}_{0.12}\text{CoSb}_{0.8}\text{Sn}_{0.2}$:

-The crystalline structure of the p-type half-Heusler is confirmed as well as the composition $\text{Hf}_{0.44}\text{Zr}_{0.44}\text{Ti}_{0.12}\text{CoSb}_{0.8}\text{Sn}_{0.2}$. The fabricated pellets present a large range of grain size from nanostructured grains with a mean size of 110 nm to larger micrometric grains from 1 μm to 10 μm . These grains are geometrically arranged as a system of isolated large grains embedded in a matrix of nanosized grains.

- Compression experiments at the macroscale including experiments with confining pressure and temperature environment led to failure stresses ranging from 1.75 GPa to 3.8 GPa. These experiments determined the exclusively brittle behavior of the alloy with a mixed intra- and inter-granular propagation observed by SEM on fracture surfaces. At the mesoscale, nanoindentation toughness method was used to generate a controlled crack propagation. Estimation of the fracture toughness K_{IC} of this material provides the range of values $1.48 \text{ MPa}\cdot\text{m}^{1/2} < K_{\text{IC}} < 2.6 \text{ MPa}\cdot\text{m}^{1/2}$, with an average value of $1.92 \text{ MPa}\cdot\text{m}^{1/2}$. The inserted cracks were subject to observation via 3D-EBSD for analyzing the crack path according to the crystallographic environment, and via TEM to study its path perpendicular to the surface as well as the crack tip. These observations corroborate fracture surface analysis on bulk specimen and confirm the absence of dislocation activity at the crack tip and in the crack path vicinity.

-At the microscale, micro-pillar compression was carried out with a nanoindenter, confirming the stress level reached from 3.1 GPa to 4.5 GPa, as well as the crack propagation modes obtained by upper scale experiments.

Chapter 4: General discussion, general conclusion and perspectives

4.1 General discussion

The purpose of this work was to study the deformation mechanisms of the nanostructured thermoelectric material p-type half-Heusler $\text{Hf}_{0.44}\text{Zr}_{0.44}\text{Ti}_{0.12}\text{CoSb}_{0.8}\text{Sn}_{0.2}$.

4.1.1 Native Microstructure

The metallurgical study of this alloy provides analysis upon novel data not mentioned in the literature. Indeed, the published data only represents this material with a 200 nm mean grain size, in an article focusing on the ability to process nanostructured alloys [85]. Instead, our grain size analysis shows there is a more complex, broad range of grain sizes in this alloy, where grain diameter was measured from 70 nm to 10 μm . The EBSD maps exhibit a pattern in the grain distribution where large grains are embedded in a matrix of nanosized grains. Therefore, the analysis focused on determining the average grain size of the nanostructured matrix which is 110 nm, although the presence of large micrometric grains may drive the macroscopic behavior, acting as the weak link in the microstructure regarding crack propagation. In addition, small precipitates were observed, 10 nm to 20 nm diameter, located either at the grain boundaries or supposedly along former grain boundaries. The precipitates must be playing a role in the phonon scattering process, as they are nanosized crystalline features of this microstructure as suggested by literature on this alloy where they are referenced as “nanodots” [84]. Usually this feature is identified as nanoprecipitates [32], which are formed during solid state reactions and proven to enhance the TE properties in half-Heusler alloys [108]. Finally, the grain size distribution

was assessed from the center to the edge of the sample. This analysis demonstrates the grain size distribution narrows down from the center the edge of the sample, with the largest grain size measured from 9 μm to 2.5 μm respectively. However, the general trend for the grain size distribution on the three mapped area is similar. There could be several factors to this, such as inhomogeneous pressure or temperature gradient during the sintering process, or perhaps a heating or cooling procedure not adapted.

As mentioned previously, a recurring pattern of grain distribution in the microstructure was identified. Observations suggest large grains embedded in a matrix of smaller grains. Regarding the phonon scattering process, these larger grains grain could be considered at first as an issue, especially for those with a micrometric diameter. However, the presence of dislocations networks within grains as observed by TEM imagery and suggested by EBSD maps, could mean the larger grains contribute to lowering the thermal conductivity more than accounted for.

4.1.2 Ductile versus brittle behavior

The proposed mechanical testing experiments, tailored to trigger plasticity and study the associated mechanisms, exclusively led to brittle failure. The failure mechanisms observed are a mixed behavior of inter- and intra-granular cracking, where the crack propagation shows little to no change in the general direction of propagation and is not accompanied by dislocation activity either around the crack tip or in the grains along the crack path. Such outcome can be analyzed by comparing the stress level reached in our experiments to theoretical work results on the (Ti, Hf and Zr)NiSn half-Heusler compounds [88]. This study identifies the weakest slip system in this structure to be $\langle\bar{1}10\rangle\{111\}$,

which is activated by a minimum shear stress of 10.52 GPa. The uniaxial compression stress necessary to activate this slip system can be estimated according to the Schmid's law, $\tau = m\sigma$, where τ is the shear stress, m the Schmid factor and σ the uniaxial compression stress. Considering a polycrystalline non-textured material, the average Schmid factor value usually stands between $m=0.33$ and $m=0.5$ for a $\{111\}$ slip plane (or its inverse - Taylor factor - stands between 2 and 3), which translates into a uniaxial compression stress between 20 GPa and 30 GPa to activate this slip system with a shear stress of 10.52 GPa. In comparison, the maximum stress reached in our study is 3.8 GPa in the Paterson machine experiment and 4.5 GPa in the case of micro-pillars, at which point the samples instantaneously fractured. Clearly, none of our experimental techniques have provided sufficient stress levels required for slip system activation. Instead, brittle failure occurs by fracture mechanisms. Even with the test temperature of 400 °C and our well controlled efforts for confinement, fracture persisted.

With such outcome, we can ask ourselves the following question: if this experimental plan thought to trigger plasticity mechanisms via dislocation activity did not succeed, does it suggest plastic deformation is definitively impossible for TE materials? A first part of the answer lies in the nature of the material studied. The p-type half-Heusler $\text{Hf}_{0.44}\text{Zr}_{0.44}\text{Ti}_{0.12}\text{CoSb}_{0.8}\text{Sn}_{0.2}$ shows relatively high elastic modulus (~231 GPa) and hardness values (~14 GPa) which do not act in favor of ductility as compared to other materials such as the Bi_2Te_3 alloys for instance, with an elastic modulus around 43 GPa and hardness as low as 1.4 GPa (Table 4, [37]). The second part of the answer may lie into the nature of the experiments conducted. The Skutterudite, usually brittle material, displays similar compression stress-strain behavior on bulk samples, with an exclusive elastic

behavior leading to brittle fracture [33]. Nevertheless, the severe plastic deformation technique High Pressure Torsion was successfully applied to it as a processing route to enforce several hundreds of percent of deformation to refine the grain size [44]–[47], at which stage dislocations must play a part in the process to relieve the stress imposed to the material, as suggested by an increase of dislocation density in early study [44]. But this single information does not allow to differentiate the isolated effect of the dislocations from the effect of the refined microstructure, and do not assess dislocation properties, or deformation mechanisms. If the plasticity cannot be triggered, then the energy is released by crack initiation, such as with our experiments, where cracks propagated to relieve the stress, hence the brittle failure, where the crack propagation is characterized as a mixed mode of inter- and intra-granular cracking. Finally, since the EDS scan in Fig. 3.2b shows elongated pocket of Hf, there is a probability this pocket is located at a GB due to its shape. If this would be to happen regularly within the microstructure, such pockets of soft material would provide the crack tip with weaker spots to engage into while propagating.

4.1.3 Crack propagation and damage mechanisms

As highlighted by the various analyses provided in this study, this material contains a wide range of grain sizes, where large grains, sometimes micrometric, are located in a matrix of nanosized grains. The fracture surfaces, as well as EBSD observations (planar and 3D) of generated cracks suggest that, at all scales, neighbor grains can affect the fracture mechanisms. As a crack initiates, its propagation will be affected by the encountered microstructure. As it encounters a large grain, too much energy is required to propagate along its GB, then rupture by cleavage is easier to reach the opposite side of the grain. At this stage, the crack tip evolves into the surrounding matrix of smaller grains,

where the grain boundaries offer more options for propagation, as well as smaller angles than when the GB of a large grain is encountered. Then the crack propagates along these GB, causing a decohesion of the matrix surrounding the larger grains, with local examples of branching as seen by TEM. Finally, the EBSD observations on inserted cracks suggest a higher level of complexity may occur within the large grains. Indeed, in Fig. 3.14 the crack propagation highlighted in the map is affected by substructures within the grain, supposedly a dislocation network. The sub-texture created by these defects impacts the crack direction locally but do not deflect it from its general direction of propagation.

Fracture toughness was estimated, within the limitation that the load used to generate the indent may be higher than the threshold load for fracture initiation. Values for K_{IC} are estimated as $1.48 \text{ MPa}\cdot\text{m}^{1/2} < K_{IC} < 2.6 \text{ MPa}\cdot\text{m}^{1/2}$, with an average value of $1.92 \text{ MPa}\cdot\text{m}^{1/2}$. Although collected from small scale and low load nanoindentation experiments, these values are consistent, although more spread, with fracture toughness estimated with the SENB configuration on bulk samples, where $1.7 \text{ MPa}\cdot\text{m}^{1/2} < K_{IC} < 2.2 \text{ MPa}\cdot\text{m}^{1/2}$ [40], [87]. Other studies on half-Heusler materials report values for $1.8 \text{ MPa}\cdot\text{m}^{1/2} < K_{IC} < 2.3 \text{ MPa}\cdot\text{m}^{1/2}$ using Vickers indentations [35]. The similarity of fracture toughness values obtained from nanoindentation, Vickers indentation and bulk setup, demonstrates the intrinsic brittleness nature of this alloy, and perhaps with extension to other half-Heusler materials, is consistent at all scales, supporting the observations on fracture surfaces, and the stress level reached throughout all the conducted experiments in this study.

4.1.4 Guidelines for material development

The grain size analysis and the identification of the fracture mechanisms suggest a narrower grain size distribution would be recommended to allow the material to support

higher loads. Indeed, a homogeneous grain size would provide less options for a crack to propagate, which would have to either evolve as intra- or inter-granular instead of a mix of the two modes. To obtain such microstructure, the effects of the sintering parameters on this alloy would need to be reviewed. The pressure and temperature sintering parameters may be optimized to an optimized ZT value, but however may not be the right option to contain crack propagation in this alloy.

4.2 General conclusion

The present study provides new data on the p-type half-Heusler $\text{Hf}_{0.44}\text{Zr}_{0.44}\text{Ti}_{0.12}\text{CoSb}_{0.8}\text{Sn}_{0.2}$. The microstructural analysis, necessary to assess the failure mechanisms, goes deeper than previous publications, showing a recurring pattern of large, sometimes micrometric grains embedded in a matrix of nanosized grains. The mechanical tests conducted at the macro-, meso-, and microscales, represent a first in the TE field. The stress-strain data are comparable at both the macro- and microscales, displaying an exclusive elastic behavior until brittle failure at similar stress levels ranging from 2 GPa to 4.5 GPa. In addition, the crack propagation is identical, combining intra- and intergranular crack propagation, as confirmed by the mesoscale experiments and analysis. The absence of dislocation activity in the crack path vicinity and at the crack tip area supports the brittle nature of this alloy. The microstructural analysis, and the fracture surface observation show a wide range of grain size. This trend is observed in bulk samples as well as in the micropillar fracture surfaces, where the larger grains tend to drive crack propagation on long distances as opposed to intergranular cracking along GB.

4.3 Perspectives

Generating data and providing a comprehensive analysis on the deformation mechanisms for the first time on a TE material contributes to the conception of future TEG. In accordance to the sandwich setup of the TEG, it would be valuable to broaden the mechanical study for basic engineering data such as flexure strength or fracture toughness measurements. Independently, the deformation analysis is necessary to fully characterize the deformation mechanisms, particularly with the current interest in dislocations in TE materials. In the case of failure by fracture, the methodology presented in this study can be used as a roadmap as it has successfully identified the observed failure mechanisms. In addition to the experiments carried out, it would be interesting to add an investigation of fracture surfaces by EDS scan for any cluster of pure element that could drive the crack propagation along GB for instance. If plasticity via dislocation activity were to be identified, an additional experiment could be worth considering.

In the p-type half-Heusler $\text{Hf}_{0.44}\text{Zr}_{0.44}\text{Ti}_{0.12}\text{CoSb}_{0.8}\text{Sn}_{0.2}$, it would be possible to conduct compression experiments on micropillars milled by FIB from grains large enough to contain either a monocrystalline pillar, or a pillar containing only few grain boundaries. An EBSD map helps to select a grain meeting these size requirements, in addition to providing its crystallographic orientation. Then a procedure similar to that described in Chapter 2 would be applied to mill a pillar by FIB. For a compression on a monocrystalline pillar, if slip planes are activated during the mechanical test, a first SEM approach would provide an analysis with data on the slip planes according to the orientation recorded by EBSD. Then it would be possible to extract a thin foil from the pillar and observe the dislocations by TEM. In the case of a micropillar compression testing, containing a few

GB could provide data on the stress level required to trigger fracture between two grains, accounting for the GB geometry. This would allow characterization of the conditions for the crack propagation to switch from intra- to inter-granular cracking mode and vice-versa.

Within the same line of work, the fracture toughness at the grain scale could be assessed, via the milling of micro-cantilever beam, to be tested in bending by nanoindentation procedure. Depending on the beam location and geometry, fracture toughness data could be extracted from single crystals, and grain boundaries interface mechanics could be studied this way, thereby completing the micro-pillars experiments.

The mixed-mode of crack propagation identified in this study highlights the importance of the impact of the microstructure on the deformation mechanisms. It shows that what may be beneficial while processing a TE material may act to the detriment of its mechanical properties. While this alloy demonstrated sustained loading to several GPa, its brittle behavior imposes stochastic limitations on the failure conditions. Therefore, after the work on composition optimization regarding its TE properties while conserving a refined grain size, it would be relevant to add the mechanical properties for consideration. The parameters to achieve the required microstructure for high TE properties would need to be reviewed. The temperature, temperature ramp, pressure, time, cooling rate parameters have to be characterized in relationship with the outcoming microstructure.

For these reasons, the deformation mechanisms remain of critical interest to design of TE materials, particularly those expected to sustain deformation such as the TE metallic alloys currently in early stage of development. Indeed, they could be shaped, welded or deformed to fit where the current solid state TE material cannot, due to their brittleness. With metallic alloy deformation, the study of dislocations is paramount. It would be

extremely valuable to identify the deformation mechanisms associated with these alloys and understand how they impact the TE properties to maximize their potential.

Bibliography

- [1] G. S. Nolas, J. Sharp, and J. Goldsmid, *Thermoelectrics : Basic principles and new materials developments*, vol. 4. Springer-Verlag Berlin Heidelberg, 2001.
- [2] D. M. Rowe, *Thermoelectrics Handbook: Macro to Nano*. Baton Rouge, UNITED STATES: CRC Press, 2005.
- [3] T. J. Seebeck, “Ueber die magnetische Polarisation der Metalle und Erze durch Temperatur-Differenz,” *Ann. Phys.*, vol. 82, no. 2, pp. 133–160, 1826.
- [4] J. C. A. Peltier, “Nouvelles expériences sur la calorificité des courants électriques,” *Ann. Chim.*, vol. 56, pp. 371–186, 1834.
- [5] W. Thomson, “On a mechanical theory of thermoelectric currents,” *Proc. R. Soc. Edinb.*, vol. 3, pp. 91–98, 1851.
- [6] W. Thomson, *Proc. R. Soc. Edinb.*, vol. 2, pp. 123–123, 1854.
- [7] L. Onsager, “Reciprocal Relations in Irreversible Processes. I.,” *Phys. Rev.*, vol. 37, no. 4, pp. 405–426, Feb. 1931.
- [8] L. Onsager, “Reciprocal Relations in Irreversible Processes. II.,” *Phys. Rev.*, vol. 38, no. 12, pp. 2265–2279, Dec. 1931.
- [9] H. B. Callen, “The Application of Onsager’s Reciprocal Relations to Thermoelectric, Thermomagnetic, and Galvanomagnetic Effects,” *Phys. Rev.*, vol. 73, no. 11, pp. 1349–1358, Jun. 1948.

- [10] L. R. S. R.S, “LVI. On the influence of obstacles arranged in rectangular order upon the properties of a medium,” *Lond. Edinb. Dublin Philos. Mag. J. Sci.*, vol. 34, no. 211, pp. 481–502, Dec. 1892.
- [11] E. Altenkirch, “Über den nutzeffekt der thermosäule,” *Phys. Z.*, vol. 10, p. 560, 1909.
- [12] M. Telkes, “The Efficiency of ThermoelectrGenerators. I.,” *J. Appl. Phys.*, vol. 18, no. 12, pp. 1116–1127, 1947.
- [13] H. J. Goldsmid and R. W. Douglas, “The use of semiconductors in thermoelectric refrigeration,” *Br. J. Appl. Phys.*, vol. 5, no. 11, pp. 386–386, 1954.
- [14] A. F. Ioffe, *Semiconductor Thermoelements, and Thermoelectric Cooling*. Infosearch, 1957.
- [15] M. Cutler, J. F. Leavy, and R. L. Fitzpatrick, “Phys. Rev. 133, A1143 (1964) - Electronic Transport in Semimetallic Cerium Sulfide,” *Phys. Rev.*, vol. 133, no. A1143, 1964.
- [16] C. Kittel, *Introduction to solid state physics 8th edition*, 2005th ed. Wiley.
- [17] H.-S. Kim, Z. M. Gibbs, Y. Tang, H. Wang, and G. J. Snyder, “Characterization of Lorenz number with Seebeck coefficient measurement,” *APL Mater.*, vol. 3, no. 4, p. 041506, Feb. 2015.
- [18] H. J. Goldsmid, *Introduction to Thermoelectricity*, vol. 121. Springer, 2010.
- [19] L. D. Hicks and M. S. Dresselhaus, “Effect of quantum-well structures on the thermoelectric figure of merit,” *Phys Rev B*, vol. 47, pp. 12727–12731, mai 1993.

- [20] L. D. Hicks and M. S. Dresselhaus, “Thermoelectric figure of merit of a one-dimensional conductor,” *Phys Rev B*, vol. 47, pp. 16631–16634, juin 1993.
- [21] J. P. Heremans, M. S. Dresselhaus, L. E. Bell, and D. T. Morelli, “When thermoelectrics reached the nanoscale.,” *Nat. Nanotechnol.*, vol. 8, no. 7, pp. 471–473, 2013.
- [22] K. F. Hsu, S. Loo, F. Guo, W. Chen, J. S. Dyck, C. Uher, T. Hogan, E. K. Polychroniadis and M. G. Kanatzidis, “Cubic $\text{AgPb}(m)\text{SbTe}(2+m)$: bulk thermoelectric materials with high figure of merit.,” *Science*, vol. 303, no. 5659, pp. 818–821, 2004
- [23] B. Poudel, Q. Hao, Y. Ma, Y. Lan, A. Minnich, B. Yu, X. Yan, D. Wang, A. Muto, D. Vashaee, X. Chen, J. Liu, M. S. Dresselhaus, G. Chen and Z. F. Ren, “High-Thermoelectric Performance of Nanostructured Bismuth Antimony Telluride Bulk Alloys,” *Science*, vol. 320, no. 5876, pp. 634–638, may 2008.
- [24] K. Biswas, J. He, I. D. Blum, C. I. Wu, T. P. Hogan, D. N. Seidman, V. P. Dravid, M. G. Kanatzidis, “High-performance bulk thermoelectrics with all-scale hierarchical architectures,” *Nature*, vol. 489, no. 7416, p. 414, Sep. 2012.
- [25] G. Slack, “In Solid State Physics, Vol. 34, H. Ehrenreich, F. Seitz and D. Turnbull, Eds,” 1979.
- [26] J. P. Heremans, V. Jovovic, E. S. Toberer, A. Saramat, K. Kurosaki, A. Charoenphakdee, S. Yamanaka and G. J. Snyder, “Enhancement of Thermoelectric Efficiency in PbTe by Distortion of the Electronic Density of States,” *Science*, vol. 321, no. 5888, pp. 554–557, 2008.

- [27] Y. Pei, X. Shi, A. LaLonde, H. Wang, L. Chen, and G. J. Snyder, “Convergence of electronic bands for high performance bulk thermoelectrics,” *Nature*, vol. 473, no. 7345, pp. 66–69, May 2011.
- [28] “U.S. Energy Flow Charts Lawrence Livermore National Laboratory,” 2016.
- [29] MINISTÈRE DE L’ENVIRONNEMENT, DE L’ÉNERGIE ET DE LA MER, and EN CHARGE DES RELATIONS INTERNATIONALES SUR LE CLIMAT, “Bilan énergétique de la France métropolitaine en 2016 - Données provisoires.” May-2017.
- [30] F. J. DiSalvo, “Thermoelectric Cooling and Power Generation,” *Science*, vol. 285, no. 5428, pp. 703–706, 1999.
- [31] G. J. Snyder and E. S. Toberer, “Complex thermoelectric materials.,” *Nat. Mater.*, vol. 7, no. 2, pp. 105–114, 2008.
- [32] S. Chen and Z. F. Ren, “Recent progress of half-Heusler for moderate temperature thermoelectric applications,” *Mater. Today*, vol. 16, no. 10, pp. 387–395, 2013.
- [33] L. Zhang, G. Rogl, A. Grytsiv, S. Puchegger, J. Koppensteiner, F. Spieckermann, H. Kabelka, M. Reinecker, P. Rogl, W. Schranz, M. Zehetbauer and M. A. Carpenter, “Mechanical properties of filled antimonide skutterudites,” *Mater. Sci. Eng. B*, vol. 170, no. 1–3, pp. 26–31, 2010.
- [34] J. E. Ni, E. D. Case, K. N. Khabir, R. C. Stewart, C. I. Wu, T. P., Hogan, E. J. Tomm, S. N. Girard and G. Mercouri, “Room temperature Young’s modulus, shear modulus, Poisson’s ratio and hardness of PbTe–PbS thermoelectric materials,” *Mater. Sci. Eng. B*, vol. 170, no. 1–3, pp. 58–66, 2010.

- [35] G. Rogl, A. Grytsiv, M. Gürth, A. Tavassoli, C. Ebner, A. Wünschek, S. Puchegger, V. Sprunyk, W. Schranz, E. Bauer, H. Müller, M. Zehetbauer and P. Rogl, “Mechanical properties of half-Heusler alloys,” *Acta Mater.*, vol. 107, pp. 178–195, 2016.
- [36] S. Gahlawat, R. He, S. Chen, L. Wheeler, Z. F. Ren, and K. W. White, “Elastic constants determined by nanoindentation for p-type thermoelectric half-Heusler,” *J. Appl. Phys.*, vol. 116, no. 8, p. 083516, 2014.
- [37] R. He, S. Gahlawat, C. Guo, S. Chen, T. Dahal, H. Zhang, W. Liu, Q. Zhang, E. Chere, K. White and Z. F. Ren, “Studies on mechanical properties of thermoelectric materials by nanoindentation,” *Phys. Status Solidi A*, vol. 212, no. 10, pp. 2191–2195, 2015.
- [38] S. LeBlanc, “Thermoelectric generators: Linking material properties and systems engineering for waste heat recovery applications,” *Sustain. Mater. Technol.*, vol. 1–2, pp. 26–35, Dec. 2014.
- [39] G. Rogl and P. Rogl, “Mechanical Properties of Skutterudites,” *Sci. Adv. Mater.*, vol. 3, no. 4, pp. 517–538, Aug. 2011.
- [40] Z. F. Ren, Y. Lan, and Q. Zhang, *Advanced Thermoelectrics: Materials, Contacts, Devices, and Systems*. CRC Press, 2017.
- [41] J. Jiang, L. Chen, S. Bai, Q. Yao, and Q. Wang, “Thermoelectric properties of textured p-type (Bi,Sb)₂Te₃ fabricated by spark plasma sintering,” *Scr. Mater.*, vol. 52, no. 5, pp. 347–351, Mar. 2005.

- [42] J. Jiang, L. Chen, S. Bai, Q. Yao, and Q. Wang, "Fabrication and thermoelectric performance of textured n-type $\text{Bi}_2(\text{Te,Se})_3$ by spark plasma sintering," *Mater. Sci. Eng. B*, vol. 117, no. 3, pp. 334–338, Mar. 2005.
- [43] V. Ravi, S. Firdosy, T. Caillat, B. Lerch, A. Calamino, R. Pawlik, M. Nathal, A. Sechrist, J. Buchhalter and S. Nutt, "Mechanical Properties of Thermoelectric Skutterudites," *AIP Conf. Proc.*, vol. 969, no. 1, pp. 656–662, Jan. 2008.
- [44] L. Zhang, A. Grytsiv, B. Bonarski, M. Kerber, D. Setman, E. Schafler, P. Rogl, E. Bauer, G. Hilscher and M. Zehetbauer, "Impact of high pressure torsion on the microstructure and physical properties of $\text{Pr}_{0.67}\text{Fe}_3\text{CoSb}_{12}$, $\text{Pr}_{0.71}\text{Fe}_{3.5}\text{Ni}_{0.5}\text{Sb}_{12}$, and $\text{Ba}_{0.06}\text{Co}_4\text{Sb}_{12}$," *J. Alloys Compd.*, vol. 494, no. 1–2, pp. 78–83, Apr. 2010.
- [45] G. Rogl, Z. Aabdin, E. Schafler, J. Horky, D. Setman, M. Zehetbauer, M. Kriegisch, O. Eibl, A. Grytsiv, E. Bauer, M. Reinecker, W. Schranz and P. Rogl, "Effect of HPT processing on the structure, thermoelectric and mechanical properties of $\text{Sr}_{0.07}\text{Ba}_{0.07}\text{Yb}_{0.07}\text{Co}_4\text{Sb}_{12}$," *J. Alloys Compd.*, vol. 537, no. 0, pp. 183–189, Oct. 2012.
- [46] G. Rogl, D. Setman, E. Schafler, J. Horky, M. Kerber, M. Zehetbauer, M. Falmbigl, P. Rogl, E. Royanian, and E. Bauer, "High-pressure torsion, a new processing route for thermoelectrics of high ZTs by means of severe plastic deformation," *Acta Mater.*, vol. 60, no. 5, pp. 2146–2157, Mar. 2012.
- [47] G. Rogl, A. Grytsiv, P. Rogl, E. Royanian, E. Bauer, J. Horky, D. Setman, E. Schafler and M. Zehetbauer, "Dependence of thermoelectric behaviour on severe

- plastic deformation parameters: A case study on p-type skutterudite $\text{DD}_{0.60}\text{Fe}_3\text{CoSb}_{12}$,” *Acta Mater.*, vol. 61, no. 18, pp. 6778–6789, Oct. 2013.
- [48] G. Chen, Y. Mu, P. Zhai, G. Li, and Q. Zhang, “An Investigation on the Coupled Thermal-Mechanical-Electrical Response of Automobile Thermoelectric Materials and Devices,” *J. Electron. Mater.*, vol. 42, no. 7, pp. 1762–1770, 2013.
- [49] R. A. Brown, “Scattering theory for crystal dislocations,” *J. Phys. F Met. Phys.*, vol. 7, no. 7, pp. 1269–1269, 1977.
- [50] N. S. Bennett, D. Byrne, and A. Cowley, “Enhanced Seebeck coefficient in silicon nanowires containing dislocations,” *Appl. Phys. Lett.*, vol. 107, no. 1, 2015.
- [51] N. S. Bennett, D. Byrne, A. Cowley, and N. Neophytou, “Dislocation loops as a mechanism for thermoelectric power factor enhancement in silicon nano-layers,” *Appl. Phys. Lett.*, vol. 109, no. 17, p. 173905, Oct. 2016.
- [52] S. I. Kim, K. H. Lee, H. A. Mun, H. S. Kim, S. W. Hwang, J. W. Roh, D. J. Yang, W. H. Shin, X. S. Li, Y. H. Lee, G. J. Snyder and S. W. Kim, “Dense dislocation arrays embedded in grain boundaries for high-performance bulk thermoelectrics,” *Science*, vol. 348, no. 6230, pp. 109–114, 2015.
- [53] P. G. Klemens, “The Thermal Conductivity of Dielectric Solids at Low Temperatures (Theoretical),” *Proc. R. Soc. Lond. Math. Phys. Eng. Sci.*, vol. 208, no. 1092, pp. 108–133, 1951.
- [54] P. G. Klemens, “The Scattering of Low-Frequency Lattice Waves by Static Imperfections,” *Proc. Phys. Soc. Sect. A*, vol. 68, no. 12, pp. 1113–1113, 1955.

- [55] P. G. Klemens, “Thermal Conductivity and Lattice Vibrational Modes,” in *Solid State Physics*, vol. 7, F. Seitz and D. Turnbull, 1958, pp. 1–98.
- [56] A. Granato and K. Lucke, “Theory of Mechanical Damping Due to Dislocations,” *J. Appl. Phys.*, vol. 27, no. 6, pp. 583–593, 1956.
- [57] J. Callaway and H. C. von Baeyer, “Effect of Point Imperfections on Lattice Thermal Conductivity,” *Phys Rev*, vol. 120, pp. 1149–1154, Nov. 1960.
- [58] P. Carruthers, “Electrical and Thermal Resistivity of dislocations,” *Phys Rev Lett*, vol. 2, no. 8, pp. 336–337, Apr. 1959.
- [59] P. Carruthers, “Theory of Thermal Conductivity of Solids at Low Temperatures,” *Rev Mod Phys*, vol. 33, no. 1, pp. 92–138, Jan. 1961.
- [60] H.-S. Kim, S. D. Kang, Y. Tang, R. Hanus, and G. Jeffrey Snyder, “Dislocation strain as the mechanism of phonon scattering at grain boundaries,” *Mater Horiz*, vol. 3, pp. 234–240, 2016.
- [61] R. L. Sproull, M. Moss, and H. Weinstock, “Effect of Dislocations on the Thermal Conductivity of Lithium Fluoride,” *J. Appl. Phys.*, vol. 30, no. 3, pp. 334–337, 1959.
- [62] T. Suzuki and H. Suzuki, “Effect of Dislocations on the Thermal Conductivity of LiF,” *J. Phys. Soc. Jpn.*, vol. 32, no. 1, pp. 164–171, 1972.
- [63] J. Zou, D. Kotchetkov, A. A. Balandin, D. I. Florescu, and F. H. Pollak, “Thermal conductivity of GaN films: Effects of impurities and dislocations,” *J. Appl. Phys.*, vol. 92, no. 5, pp. 2534–2539, 2002.

- [64] C. Mion, J. F. Muth, E. A. Preble, and D. Hanser, “Accurate dependence of gallium nitride thermal conductivity on dislocation density,” *Appl. Phys. Lett.*, vol. 89, no. 9, 2006.
- [65] D. Eyidi, D. Maier, O. Eibl, and M. Westphal, “Chemical Composition and Crystal Lattice Defects of Bi₂Te₃ Peltier Device Structures,” *Phys. Status Solidi A*, vol. 187, no. 2, pp. 585–600, 2001.
- [66] N. Peranio and O. Eibl, “Gliding dislocations in Bi₂Te₃ materials,” *Phys. Status Solidi A*, vol. 206, no. 1, pp. 42–49, 2009.
- [67] F. R. N. Nabarro, “The Interaction of Screw Dislocations and Sound Waves,” *Proc. R. Soc. Lond. Ser. Math. Phys. Sci.*, vol. 209, no. 1097, pp. 278–290, 1951.
- [68] V. Esayan, A. Sarkisyan, and A. Durgaryan, “Absorption of Ultrasound in Bi₂Te₃ Crystals and Their Electrical-Properties,” *Sov. Phys. Semicond.-Ussr*, vol. 15, no. 12, pp. 1341–1343, 1981.
- [69] K. Biswas, J. He, Q. Zhang, G. Wang, C. Uher, V. P. Dravid and M. G. Kanatzidis, “Strained endotaxial nanostructures with high thermoelectric figure of merit,” *Nat. Chem.*, vol. 3, no. 2, pp. 160–166, Feb. 2011.
- [70] J. Mao, “Defect Engineering in Thermoelectric Materials,” Ph.D. Thesis, University of Houston, 2018.
- [71] Z. Chen, Z. Jian, W. Li, Y. Chang, B. Ge, R. Hanus, J. Yang, Y. Chen, M. Huang, G. J. Snyder and Y. Pei, “Lattice Dislocations Enhancing Thermoelectric PbTe in Addition to Band Convergence,” *Adv. Mater.*, vol. 29, no. 23, Jun. 2017.

- [72] Z. Chen, B. Ge, W. Li, S. Lin, J. Shen, Y. Chang, R. Hanus, G. J. Snyder and Y. Pei, “Vacancy-induced dislocations within grains for high-performance PbSe thermoelectrics,” *Nat. Commun.*, vol. 8, p. 13828, Jan. 2017.
- [73] S. R. Boona, S. J. Watzman, and J. P. Heremans, “Research Update: Utilizing magnetization dynamics in solid-state thermal energy conversion,” *APL Mater.*, vol. 4, no. 10, p. 104502, Jul. 2016.
- [74] S. R. Boona, R. C. Myers, and J. P. Heremans, “Spin caloritronics,” *Energy Environ. Sci.*, vol. 7, no. 3, pp. 885–910, Feb. 2014.
- [75] H. Jin, O. D. Restrepo, N. Antolin, S. R. Boona, W. Windl, R. C. Myers and J. P. Heremans, “Phonon-induced diamagnetic force and its effect on the lattice thermal conductivity,” *Nat. Mater.*, vol. 14, no. 6, pp. 601–606, Jun. 2015.
- [76] S. R. Boona, K. Vandaele, I. N. Boona, D. W. McComb, and J. P. Heremans, “Observation of spin Seebeck contribution to the transverse thermopower in Ni-Pt and MnBi-Au bulk nanocomposites,” *Nat. Commun.*, vol. 7, p. 13714, Dec. 2016.
- [77] S. J. Watzman, R. A. Duine, Y. Tserkovnyak, S. R. Boona, H. Jin, A. Prakash, Y. Zheng and J. P. Heremans, “Magnon-drag thermopower and Nernst coefficient in Fe, Co, and Ni,” *Phys. Rev. B*, vol. 94, no. 14, p. 144407, Oct. 2016.
- [78] M. Adams, Y. Zheng, and J. P. Heremans, “APS -APS March Meeting 2018 - Event - Portable Combustion Generator with Integrated Thermoelectric/Heat Exchanger,” in *Bulletin of the American Physical Society*.
- [79] W. Jeitschko, “Transition metal stannides with MgAgAs and MnCu₂Al type structure,” *Metall. Trans.*, vol. 1, no. 11, pp. 3159–3162, Nov. 1970.

- [80] L. Huang, Q. Zhang, B. Yuan, X. Lai, X. Yan, and Z. F. Ren, “Recent progress in half-Heusler thermoelectric materials,” *Mater. Res. Bull.*, vol. 76, pp. 107–112, 2016.
- [81] X. Yan, G. Joshi, W. Liu, Y. Lan, H. Wang, S. Lee, J. W. Somonson, S. J. Poon, T. M. Tritt, G. Chen and Z. F. Ren, “Enhanced Thermoelectric Figure of Merit of p-Type Half-Heuslers,” *Nano Lett.*, vol. 11, no. 2, pp. 556–560, 2011.
- [82] G. Joshi, X. Yan, H. Wang, W. Liu, G. Chen, and Z. F. Ren, “Enhancement in Thermoelectric Figure-Of-Merit of an N-Type Half-Heusler Compound by the Nanocomposite Approach,” *Adv. Energy Mater.*, vol. 1, no. 4, pp. 643–647, 2011.
- [83] Y. Kimura, H. Ueno, and Y. Mishima, “Thermoelectric Properties of Directionally Solidified Half-Heusler (M,M)NiSn (Ma, Mb = Hf, Zr, Ti) Alloys,” *J. Electron. Mater.*, vol. 38, no. 7, pp. 934–939, Jul. 2009.
- [84] X. Yan, W. Liu, H. Wang, S. Chen, J. Shiomi, K. Esfarjani, H. Wang, D. Wang, G. Chen and Z. F. Ren, “Stronger phonon scattering by larger differences in atomic mass and size in p-type half-Heuslers $\text{Hf}_{1-x}\text{Ti}_x\text{CoSb}_{0.8}\text{Sn}_{0.2}$,” *Energy Env. Sci.*, vol. 5, pp. 7543–7548, 2012.
- [85] X. Yan, W. Liu, S. Chen, H. Wang, Q. Zhang, G. Chen and Z. F. Ren, “Thermoelectric Property Study of Nanostructured p-Type Half-Heuslers (Hf, Zr, Ti)CoSb_{0.8}Sn_{0.2},” *Adv. Energy Mater.*, vol. 3, no. 9, pp. 1195–1200, 2013.
- [86] R. He, “PhD thesis, Study on Half-Heusler Compounds for Thermoelectric Power Generation,” University of Houston, 2016.
- [87] S. Gahlawat, R. He, S. Chen, Z. F. Ren, and K. White, “Unpublished work.”

- [88] G. Li, Q. An, U. Aydemir, W. A. Goddard III, M. Wood, P. Zhai, Q. Zhang and G. J. Snyder, “Enhanced ideal strength of thermoelectric half-Heusler TiNiSn by substructure engineering,” *J. Mater. Chem. A*, vol. 4, no. 38, pp. 14625–14636, Sep. 2016.
- [89] A. Winkelmann, C. Trager-Cowan, F. Sweeney, A. P. Day, and P. Parbrook, “Many-beam dynamical simulation of electron backscatter diffraction patterns,” *Ultramicroscopy*, vol. 107, no. 4–5, pp. 414–421, Apr. 2007.
- [90] S. I. Wright and M. M. Nowell, “EBSD Image Quality Mapping,” *Microsc. Microanal.*, vol. 12, no. 1, pp. 72–84, Feb. 2006.
- [91] L. Holzer and M. Cantoni, *Review of FIB-tomography*. 2012.
- [92] M. A. Groeber, B. K. Haley, M. D. Uchic, D. M. Dimiduk, and S. Ghosh, “3D reconstruction and characterization of polycrystalline microstructures using a FIB–SEM system,” *Mater. Charact.*, vol. 57, no. 4, pp. 259–273, Dec. 2006.
- [93] M. Groeber, “Development of an automated characterization-representation framework for the modeling of polycrystalline materials in 3D,” The Ohio State University, 2007.
- [94] J. S. Tiley, A. R. Shiveley, A. L. Pilchak, P. Z. Shade, and M. Z. Groeber, “3D reconstruction of prior β grains in friction stir–processed Ti–6Al–4V,” *J. Microsc.*, vol. 255, no. 2, pp. 71–77, Aug. 2014.
- [95] H. Abrams, “Grain size measurement by the intercept method,” *Metallography*, vol. 4, no. 1, pp. 59–78, Feb. 1971.

- [96] M. S. Paterson, “A high-pressure, high-temperature apparatus for rock deformation,” *Int. J. Rock Mech. Min. Sci. Geomech. Abstr.*, vol. 7, no. 5, pp. 517–526, Sep. 1970.
- [97] A. Guitton, “Mécanismes de déformation des phases MAX : une approche expérimentale multi-échelle,” Ph.D. Thesis, Université de Poitiers, 2013.
- [98] B. Kedjar, “Ph.D. Thesis, Etude des mécanismes de plasticité des semiconducteurs sous pression hydrostatique : cas de l’antimoniure d’indium InSb,” Université de Poitiers, 2007.
- [99] B. Kedjar, L. Thilly, J.-L. Demenet, and J. Rabier, “Plasticity of indium antimonide between -176°C and 400°C under hydrostatic pressure. Part I: macroscopic aspects of the deformation,” *Acta Mater.*, vol. 58, pp. 1418–1418, 2010.
- [100] A. Guitton, A. Joulain, L. Thilly, and C. Tromas, “Dislocation analysis of Ti₂AlN deformed at room temperature under confining pressure,” *Philos. Mag.*, vol. 92, no. 36, pp. 4536–4546, 2012.
- [101] J. L. Hay and G. M. Pharr, “Instrumented Indentation Testing,” in *ASM Handbook, Volume 8: Mechanical Testing and Evaluation*, A S M International, 2000, pp. 232–243.
- [102] G. M. Pharr, “Measurement of mechanical properties by ultra-low load indentation,” *Mater. Sci. Eng. A*, vol. 253, no. 1–2, pp. 151–159, 1998.
- [103] M. D. Uchic, D. M. Dimiduk, J. N. Florando, and W. D. Nix, “Sample Dimensions Influence Strength and Crystal Plasticity,” *Science*, vol. 305, no. 5686, pp. 986–989, 2004.

- [104] J. R. Greer, W. C. Oliver, and W. D. Nix, “Size dependence of mechanical properties of gold at the micron scale in the absence of strain gradients,” *Acta Mater.*, vol. 53, no. 6, pp. 1821–1830, Apr. 2005.
- [105] I. N. Sneddon, “The relation between load and penetration in the axisymmetric boussinesq problem for a punch of arbitrary profile,” *Int. J. Eng. Sci.*, vol. 3, no. 1, pp. 47–57, May 1965.
- [106] W. C. Oliver and G. M. Pharr, “An improved technique for determining hardness and elastic modulus using load and displacement sensing indentation experiments,” *J. Mater. Res.*, vol. 7, no. 6, pp. 1564–1583, Jun. 1992.
- [107] G. Guillonneau, G. Kermouche, S. Bec, and J.-L. Loubet, “Determination of mechanical properties by nanoindentation independently of indentation depth measurement,” *J. Mater. Res.*, vol. 27, no. 19, pp. 2551–2560, Oct. 2012.
- [108] J. P. A. Makongo, D. K. Misra, X. Zhou, A. Pant, M. R. Shabetai, X. Su, C. Huer, K. L. Stokes and P. F. Poudeu, “Simultaneous Large Enhancements in Thermopower and Electrical Conductivity of Bulk Nanostructured Half-Heusler Alloys,” *J. Am. Chem. Soc.*, vol. 133, no. 46, pp. 18843–18852, Nov. 2011.